2026

Journal of JART

—English edition—

2026

The Japan Association of Radiological Technologists

Journal of JART —English edition—
2026
The Japan Association of Radiological Technologists

CONTENTS

Note: The contents of this magazine are those that have been published in JART magazine.

Overview of the Japan Association of Radiological Technologists

The Japan Association of Radiological Technologists, a public interest incorporated association under the jurisdiction of the Ministry of Health, Labour and Welfare, was established in 1947 with the purpose of contributing to the health of citizens through raising the professional ethics of members, improving and furthering the study of medical radiology and medical radiological technology, and enhancing public health.

In light of the startling progress being made in the fields of image diagnostics and radiation therapy where radiological technologists work, it is necessary to stay constantly aware of the latest know-how and technology. JART collaborates with other certification agencies to enhance the capacity of all radiological technologists in general through providing lifelong learning seminars, short courses, academic conferences and numerous other learning opportunities. We believe that such activities constitute our obligation as medical professionals to the general public.

As the only medical profession that has “radiological” in its name, we strive to limit medical exposure, to raise the standing of our profession, and to realize a profession of specialist technologists that can be advertised. And we are committed to promoting services with you all for the provision of safe and secure medical care.

general principles

We will render our services to those in need of health care.

We will act as members of a health care team.

We will perform our duties in our field of specialty.

We will continue to study for the benefit of humanity.

We will respect and practice the principle of informed consent.

Regarding Publication of the English Edition

UEDA Katsuhiko (President)

The journal of the JART English version issues every year. It has a favorable reception for we members of the world and general people. As well as this issue, 11 articles to be useful for radiological technologists are issued.

We will feature clinical, educational, and research-based achievements by radiological technologists in the monthly issues of the JART journal, and continually work to improve the magazine. I truly hope that this English edition will benefit radiological technicians worldwide.

To give our radiological technologists from across the globe an insight into our business, I will briefly explain the history of the JART. In March 1896, we succeeded in taking the first X-ray image in Japan. In 1897, Shimadzu Corporation released an X-ray generator for educational use. In 1925, there were approximately 1,500 X-ray technicians. In 1927, the first Shimadzu X-ray Technician Training Institute was established, and evidence-based education was put in place. The JART was founded in 1947 to make “radiological technologist” a national qualification. Since its establishment, we have worked towards broad acceptance of this national qualification, in collaboration with the government, the Diet, the Japanese Medical Association, and occupational military authorities.

As a result in June 1951, we were finally able to see the promulgation of the Radiology X-ray Technicians Act, Act No.226 of 1951. Since then, we have responded to the changing needs of the society, revising the original act to get the Radiology X-ray Technicians Act of 1968 passed, and partially revising that to get the Radiology Technicians Act and Radiology X-ray Technicians Act of 1983 passed, and finally getting the Radiology Technicians Act, which is in place currently, passed. Back then, the scope of work was limited to general X-ray testing, television X-ray testing, angiography, X-ray computed tomography scanning, RI scanning, and radiation therapy. In 1993, the Radiology Technicians Act was further revised, and MRI scanning, ultrasonic testing, and non-mydriatic fundus camera examination were added to the list. In 2010, image interpretation assistance, radiation examination explanation, and consultation work were added. In April 2015, intravenous contrast agent injection using automated contrast injectors, needle removal and hemostasis, lower digestive tract examination (anal catheter insertion and administration of contrast medium), anal catheter insertion, and oxygen inhalation during radiation therapy were added as operations that could be performed by radiological technologists.

In October 2021, the needle insertion for examinations of contrasting of the examination for CT, MRI, Ultrasound and Radioisotope are added as the new operation that can be performed by radiological technologists.

The JART will continue to respond to the needs of the medical industry, and we hope to broaden the operational scope of radiological technologists based on our foundation in scientific evidence.

History of The Japan Association of Radiological Technologists (JART)

1947
- Establishment of JART (July 13)

1951
- Promulgation of the Act on Medical Radiographers (June 11)
- Authorization for Establishment of the Japan Association of Radiographers (June 13)

1954
- First national examination for Medical Radiographers (May 30)

1956
- Event to commemorate the 10th anniversary of founding, attended by Her Imperial Highness Princess Chichibunomiya

1962
- Event to commemorate the 15th anniversary of founding and 10th anniversary of enactment of the Act on Medical Radiographers, attended by Her Imperial Highness Princess Chichibunomiya

1968
- Promulgation of the Act to Partially Revise the Act on Medical Radiographers (establishment of two professions) (May 23)
- First national examination for radiological technologists

1969
- Renaming as the JART
- Staging of the 4th International Society of Radiographers & Radiological Technologist (ISRRT) World Congress at Tokyo Palace Hotel, attended by Her Imperial Highness Princess Chichibunomiya

1975
- Event to commemorate the 80th anniversary of the discovery of X-rays, attended by Her Imperial Highness Princess Chichibunomiya

1979
- Completion of the Education Center for JART

1983
- Partial revision of the Act on Medical Radiographers and the Act on Radiological Technologists (unification of the professions)

1985
- Event to commemorate the 90th anniversary of the discovery of X-rays, attended by Her Imperial Highness Princess Chichibunomiya
- Staging of the 1st Japan Conference of Radiological Technologists

1987
- General assembly resolution for establishment of the New Education Center and a four-year university

1989
- Completion of the New Education Center (Suzuka City)

1991
- Opening of Suzuka University of Medical Science

1993
- The Act to Partially Revise the Act on Radiological Technologists, and Ministerial Ordinance to Partially Revise the Enforcement Orders (April 28)

1994
- Appointment of the President of JART as the 11th President of ISRRT

1995
- Event to commemorate the 100th anniversary of the discovery of X-ray, attended by Her Imperial Highness Prince Akishinomiya

1996
- Start of the Medical Imaging and Radiologic Systems Manager certification system

1998
- Staging of the 11th ISRRT World Congress at Makuhari

1999
- Start of the Radiation Safety Manager certification system

2000

- "Presentation of the Medical Exposure Guidelines (Reduction Targets)" for patients

2001

- Start of the Radiological Technologists Liability Insurance System

2003

- Enactment of X-Ray Week

2004

- Relocation of offices to the World Trade Center Building in Tokyo

2005

- Start of the Medical Imaging Information Administrator certification system

2006

- Staging of a joint academic conference between Japan, South Korea, and Taiwan
- Revision of the Medical Exposure Guidelines

2008

- Establishment of the committee on Autopsy imaging (Ai)

2009

- Revision to the national examination for radiological technologists
- Launch of the Team Medicine Promotion Conference, with the President of JART as its representative
- Appointment of the President of JART as chairperson of the Central Social Insurance Medical Council specialist committee

2010

- Health Policy Bureau Director's notification concerning promotion of team medicine

2011

- Support activities following the Great East Japan Earthquake
- Staging of an extraordinary general meeting concerning transition to a public interest incorporated association

2012

- Registration of transition to a public interest incorporated association (April 1)
- Event to mark the 65th anniversary of founding and transition to a public interest incorporated association (June 2)
- Renaming as public interest incorporated association JART
- Launch of the Radiological Technologists Liability Insurance System with participation by all members

2013

- Signing of the Comprehensive Mutual Cooperation Agreement on Prevention of Radiation Exposure (September 21)

2014

- Consignment of work to measure personal exposure of residents
- Revision of the Act on Radiological Technologists, Government Ordinance to Partially Revise the Enforcement Orders, and Revision of the Enforcement Regulations (June 25)
- Launch of the radiation exposure advisor certification system

2015

- Event to commemorate the 120th anniversary of the discovery of X-rays

2017

- Event to mark the 70th anniversary of founding (June 2)

2018

- Notice from the Regional Medical Care Planning Division Director, Health Policy Bureau, Ministry of Health, Labour and Welfare, and Director of the Economic Affairs Division regarding Operational Considerations for Securing a System for Safety Management pertaining to Medical Equipment

2019

- Notice from the Health Policy Bureau on a Safety Management System for Medicinal Use of Radiation

2020

- Partial revision of the Ordinance on Prevention of Ionizing Radiation Hazards

2021

- Relocation of offices to the Mita Kokusai Building in Tokyo
- Revision of the Radiological Technologists Act expanded the scope of practice.
- Holding the 23th AACRT with 37th JCRT in Tokyo

2022

- Event to mark the 75th anniversary of founding (July 16)

Received October 31, 2024; accepted January 17, 2025

Evaluation of Image Quality during Upper Abdomen Imaging with Golden-Angle Radial Sparse Parallel-Volumetric Interpolated Breath-hold Examination in Combination with Electromagnetic Wave Suppression Sheet: A Study Using Phantoms

ITO Kazuyuki*, SHIRATO Takashi, YOKOYAMA Hikaru, HAMASAKI Nozomi

Department of Radiology, Juntendo University Nerima Hospital

* E-mail: kito@juntendo.ac.jp

Note: This paper is secondary publication, the first paper was published in the JART, vol. 72 no. 878: 19-27, 2025.

Key words: Golden Angle Radial Sparse Parallel (GRASP), electromagnetic wave suppression, streak artifact, image uniformity

【Abstract】
Purpose: In the context of upper abdominal imaging using Golden-Angle Radial Sparse Parallel-Volumetric Interpolated Breath-hold Examination (GRASP-VIBE), streaking artifacts caused by drooping arms lead to a degradation in image quality. This study examined the effect of employing an electromagnetic wave suppression (EWS) sheet to cover the arm, aiming to reduce streaking artifacts and assess its impact on image quality using a phantom model.
Methods: The phantom was arranged to simulate conditions of both raised and lowered arms, and imaging was performed using both GRASP-VIBE and conventional VIBE techniques. The phantom was covered with an EWS sheet, and the streaking artifacts were quantified. Image uniformity was assessed through a gray scale uniformity map.
Results: The use of the EWS sheet resulted in a significant reduction of streaking artifacts; however, a notable decrease in uniformity was observed in GRASP-VIBE imaging.
Conclusion: The application of the EWS sheet in GRASP-VIBE imaging, when covering the drooping arm, may alleviate streaking artifacts in upper abdominal imaging. Nevertheless, due to radial sampling, signal intensity may fluctuate within the field of view as a consequence of the static magnetic field inhomogeneity induced by the EWS sheet.

Introduction

The standard protocol for magnetic resonance imaging (MRI) of the upper abdomen requires patients to suspend respiration during the examination. However, respiratory capacity varies among individuals, and prolonged imaging may result in respiratory artifacts due to inadequate breath-holding. Furthermore, typical respiratory durations (10-15 seconds) impose limitations on spatial resolution and imaging range. Golden-Angle Radial Sparse Parallel-Volumetric Interpolated Breath-hold Examination (GRASP-VIBE) [1], a recently developed technique by Siemens, employs a radial k-space trajectory with golden angles and compressed sensing. GRASP-VIBE demonstrates the capability to acquire images with high temporal and spatial resolution under free-breathing conditions, which can be utilized in dynamic contrast-enhanced (DCE) MRI. The clinical efficacy of this technique has been substantiated in numerous cases [2, 3]. In our hospital, GRASP-VIBE stands out as the most commonly employed radial imaging methodology for upper abdominal MRI examinations, representing a sophisticated approach in this field. One drawback of GRASP-VIBE is the presence of streaking artifacts inherent to radial imaging [4]. While many streaking artifacts in radial images can be attributed to undersampling, the Nyquist condition is violated in the outer regions of k-space. It has also been reported that imaging

objects with a large field of view (FOV) causes streaking artifacts due to nonlinearities in the magnetic field gradient at the edge of the magnet [5]. Strong streaking artifacts degrade image quality and, in some cases, obscure pathology. In abdominal imaging, a common source of streaks is drooping arms [6]. For patients with limited arm mobility due to intravenous cannulation or restricted joint range of motion, imaging is typically performed with the arms positioned inferiorly. The resultant streaking artifacts on the image, caused by the lowered arm position, may potentially compromise the visualization of abdominal organs. Although increasing the number of spokes filling k-space can mitigate streaking artifacts, it also extends the duration of the imaging process.

Currently, there exist medical devices designed to mitigate the effects of electromagnetic waves emitted during MRI examinations. These electromagnetic wave suppression (EWS) sheets are believed to improve image quality by reducing signals that contribute to aliasing and motion artifacts [7]. However, no studies have yet assessed the image quality of radial sampling in conjunction with EWS sheets. Our hypothesis posited the possibility of diminishing streaking artifacts through the application of the EWS sheet on the arms during GRASP-VIBE imaging.

The objective of this research was to examine the influence of the EWS sheet on the arms of the images obtained during an upper abdominal examination using GRASP-VIBE by employing phantoms for imaging purposes.

Materials and Methods

All examinations were performed using a 3T MAGNETOM Vida MR scanner (Siemens Healthcare, Erlangen, Germany) with a BM Spine 32 ch coil and a BM Body 18 ch coil. A spherical phantom (MARCOL-Oil + 0.011 g MACROLEX blue, ϕ 240 mm, T_1 value 180 ms, T_2 value 83 ms) and cylindrical phantoms ($NiCl_2$*H_2O, H_2O, ϕ 80 mm × 350 mm, T_1 value 57 ms, T_2 value 30 ms) that had been used for maintenance of our MRI systems were used as subjects. For the EWS sheet (tranduction sheet® J・Trust, Tokyo, Japan), 50 cm × 60 cm in size, was used. The EWS sheet comprises copper, acting as an electromagnetic wave reflector, and carbon, serving as an absorber. This sheet is a multilayer structure consisting of copper and carbon, with the exterior of the sheet being copper. Objects covered with this sheet are immune to electromagnetic waves. The sheet is thin and lightweight, making it suitable for wrapping around limbs. The study employed seven distinct phantom configurations, as illustrated in Fig. 1. The phantom diameter was determined by referencing the distribution of abdominal circumference within the Japanese population [8], as published by the Ministry of Health, Labor and Welfare. A spherical phantom with a diameter of 240 mm acted as the torso substitute, while a cylindrical phantom with a diameter of 80 mm served as the arms' representative. The setup featuring

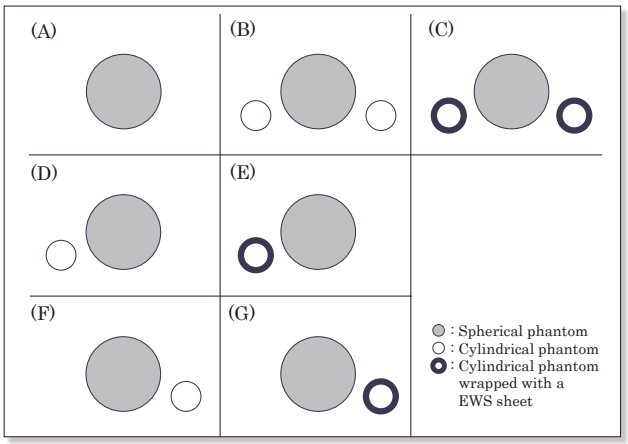

Fig. 1 Schematic representation of the seven phantom configurations.

(A) Central spherical phantom. (B) Cylindrical phantoms placed on both sides of the spherical phantom. (C) Configuration B with sheets wrapped around the cylindrical phantoms. (D) Cylindrical phantom placed only on the right side of the spherical phantom. (E) Configuration D with a sheet wrapped around the cylindrical phantom. (F) Cylindrical phantom placed only on the left side of the spherical phantom. (G) Configuration F with a sheet wrapped around the cylindrical phantom.

two cylindrical phantoms assumed both arms were hanging down, whereas the setup with only one cylindrical phantom assumed one arm was raised. The phantoms were placed at the radiofrequency (RF) coils' center. After allowing the fluid in the phantom to settle for roughly 10 minutes, scanning was performed. In each phantom configuration, imaging was done in the axial section, with the center of the scanning range positioned at the center of the spherical phantom. A single imaging was conducted for each phantom configuration. From the acquired images, the image of the largest cross section of the spherical phantom was chosen for evaluation.

In this research, we employed both GRASP-VIBE and conventional VIBE methodologies. In GRASP-VIBE, the number of radial spokes filling the k-space is contingent upon factors such as duration time, temporal resolution, repetition time (TR), and the utilization of liver gating technique [9]. To perform GRASP-VIBE, it is necessary to establish the conditions of 2-4 phases. For each phase, a specific duration time is designated, and data is collected continuously for the entire duration period. Images are then reconstructed using the corresponding number of spokes based on the temporal resolution from the data gathered during the designated duration time. A longer duration time results in more data being collected, leading to a longer scan time. Conversely, increasing the temporal resolution setting increases the number of radial spokes filling the k-space, but diminishes the temporal resolution. The temporal resolution is also influenced by the TR. When employing the self-navigation method of "liver gate," which is a respiratory synchronization technique, only 50% of the data collected on the expiratory side is utilized for image reconstruction. This equates to half the number of radial spokes in the k-space compared to the set temporal resolution. A reduction in the number of radial spokes in the k-space results in an increased influence of streaking artifacts. Respiratory synchronization utilizing the liver gate is essential for imaging the upper abdomen, and it is crucial to control the streaking artifact. Consequently, the experiments conducted in this study were performed under the liver DCE-MRI examination conditions with a combined liver gate employed at our institution. GRASP-VIBE sequence was acquired with the following parameters: FOV 370 × 370 mm, base resolution 288, slice thickness 3.0 mm, slice resolution 68%, slices per slab 72, slice oversampling 11.1%, phase oversampling 0%, TR 3.5 ms, echo time (TE) 1.39 ms, flip angle (FA) 8°, fast fat saturation, slice partial fourier 5 / 8, bandwidth 1160 Hz / Px, Normalize Prescan, phases 4, first duration 15 s, second duration 35 s, third duration 60 s, fourth duration 120 s, temporal resolution 14.6 s, liver gate, delay after bolus 25 s, total acquisition time 4 min 14 s. All analyses were performed using 1st phase images. Conventional VIBE is performed using Cartesian k-space trajectories. Therefore, it was acquired to evaluate the effect of image uniformity resulting from different k-space trajectories. Parameters of conventional VIBE sequence were as follows: FOV 370 × 370 mm, matrix 288 × 288, slice thickness 4.0 mm, slice resolution 61%, slices per slab 60, slice oversampling 20.0%, phase oversampling 10%, TR 3.3 ms, TE 1.15 ms, FA 10°, fast fat saturation, acceleration mode CAIPIRINHA, acceleration factor PE 1, acceleration factor 3D 3, slice partial fourier 7 / 8, bandwidth 620 Hz / Px, Normalize Prescan, total acquisition time 19 s.

Evaluation of streaking artifacts

We employed a technique to quantify background signal values to evaluate streaking artifacts [4]. In areas where signal values are expected to be nearly zero, streaks substantially elevate the average signal. The signal value increases progressively with the intensity of the streaks and approaches zero in

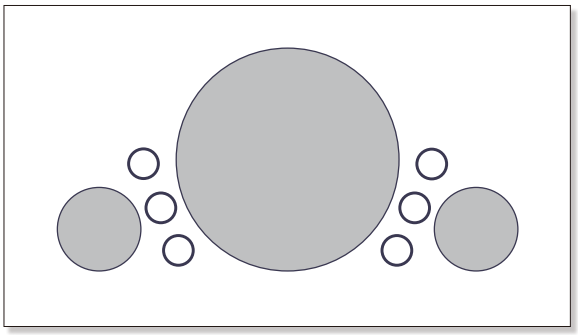

Fig. 2 ROI setting method for the measurement of signal intensity in air.

their absence. The phantom was imaged using GRASP-VIBE in the configurations illustrated in Fig. 1a - 1c. Three slices from the central region of the imaging range were utilized for evaluation. For the acquired images, we designated regions of interest (ROIs) at three locations on each side of the spherical phantom, and we measured the signal values in air (Fig. 2). These measurements were subsequently compared, and statistical analysis was conducted utilizing the Kruskal-Wallis and Steel-Dwass multiple comparison tests ($p < 0.05$) (EZR v. 1.67 Jichi Medical University Saitama Medical Center, Saitama, Japan).

Image uniformity

The phantom was imaged utilizing GRASP-VIBE and conventional VIBE in the seven configurations illustrated in Fig. 1a - 1g, and gray scale uniformity maps [10] were generated using the image of a single slice at the imaging center. Gray scale uniformity maps were created in accordance with the National Electrical Manufacturers Association (NEMA) method. A ROI at the center of the image was selected to encompass 75% of the signal-producing volume. The signal from each pixel in the entire image was examined, and a five-step gray level was assigned to each pixel according to the magnitude by which the signal deviated from the mean value at the center ROI. A five-step gray-level representation of image nonuniformity was employed with the following ranges relative to the mean value:

A. lowest signal value to -20%
B. -20% through -10%
C. -10% through +10%
D. +10% through +20%
E. +20% through to highest signal value

This map serves as a visual evaluation method for assessing the location and structure of nonuniformities but does not provide a quantitative value. Consequently, we obtained the percent image uniformity (PIU) from the gray scale uniformity map, referencing previous reports [11] to compare the differences in phantom configuration and imaging sequence. The groups A - E aforementioned, designated for the creation of the gray scale uniformity map, were consolidated to form three distinct groups, 0 - 2:

Group 0: Total number of pixels from group C
Group 1: Total number of pixels from groups B and D
Group 2: Total number of pixels from groups A and E

The number of pixels in each of these groups was then used to compute a PIU as follows:

$$PIU = 100\,(1 - (0.5 \cdot group1 + group2) / (group0 + group1 + group2)) \cdots\cdots\cdots (1)$$

Results

Streaking artifacts

Images obtained from the three distinct phantom configurations utilized for evaluation, along with graphs generated from the measured data, are presented in Figs 3 and 4. The median values for configurations A, B, and C were 45.52, 104.52, and 60.63, respectively. A Kruskal-Wallis test revealed a significant difference among the three configurations ($p < 0.05$). Post-hoc multiple comparisons using the Steel-Dwass test indicated significant differences between configuration A and B

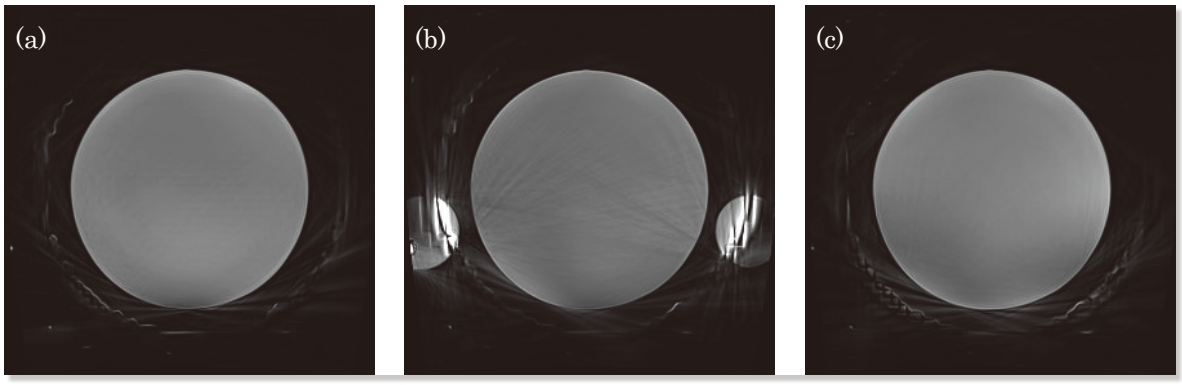

Fig. 3 Phantom image by GRASP-VIBE.
(a) Phantom configuration A
(b) Phantom configuration B
(c) Phantom configuration C

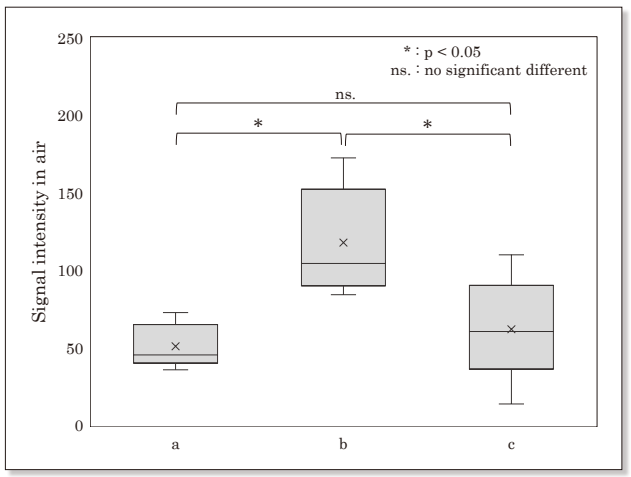

Fig. 4 Measured signal value in air to evaluate streaking artifacts.
(a) Phantom configuration A
(b) Phantom configuration B
(c) Phantom configuration C

($p < 0.05$), as well as between configuration B and C ($p < 0.05$). However, no significant difference was found between configuration A and C ($p = 0.63$).

Image uniformity

Gray scale uniformity maps obtained through GRASP-VIBE and conventional VIBE imaging techniques are presented in Figs 5 and 6. In conventional VIBE imaging, phantom configurations C, E, and G displayed heightened signals near the sheet within the spherical phantom. However, in GRASP-VIBE, phantom configuration C showed lower signal values within the spherical phantom between EWS sheets, while phantom configurations E and G exhibited reduced signal values in the anterior region of the spherical phantom. PIUs for seven distinct phantom arrangements obtained via GRASP-VIBE and conventional VIBE are enumerated in Table 1. Comparing identical phantom placements with and without the EWS sheet encircling the cylindrical phantom revealed that GRASP-VIBE showed a reduction of 11.26% to 14.09% in PIUs when the EWS sheet was applied, compared to when it was not used. On the other hand, conventional VIBE showed a decrease of 1.66% to 2.22%.

Discussion

In this investigation, we evaluated the influence of wrapping the EWS sheet around the arm on images acquired during upper abdominal imaging with GRASP-VIBE, using a phantom. The EWS sheet demonstrated efficacy in mitigating streaking artifacts caused by the arm. Nonetheless, its placement was observed to potentially result in a reduction of signal intensity in the abdominal region, thereby affecting the overall uniformity of the image.

GRASP-VIBE incorporates fat suppression techniques; however, when the arm is drooped, adequate fat suppression is often not achieved, particularly in off-center regions

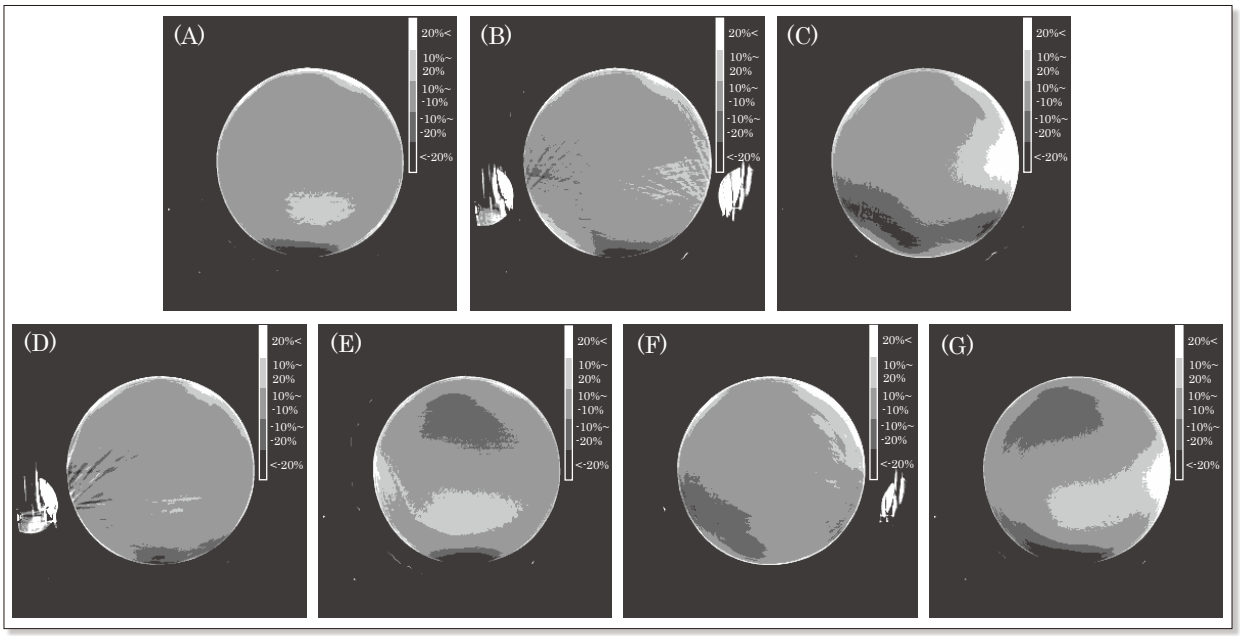

Fig. 5 Gray scale uniformity map of GRASP-VIBE in 7 different phantom configurations.

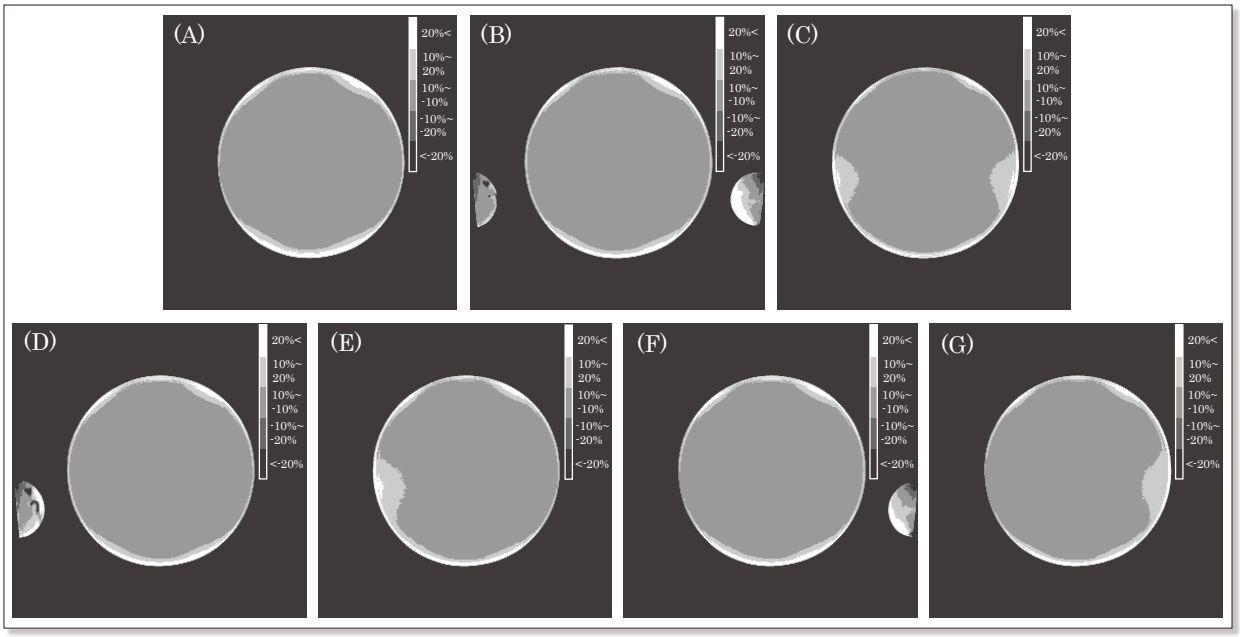

Fig. 6 Gray scale uniformity map of conventional VIBE in 7 different phantom configurations.

Table 1 The percent image uniformities for GRASP-VIBE and conventional VIBE at each phantom configuration.

	Percent image uniformity						
Phantom configuration	A	B	C	D	E	F	G
GRASP-VIBE	88.14	87.41	73.32	89.67	78.41	84.08	70.85
Conventional VIBE	90.55	91.52	89.30	91.22	89.38	91.38	89.72

where the arm is positioned, due to the nonlinearity of the magnetic field gradient. As a result, streaking artifacts arising from the arm that maintain high signal values are generated, thereby deteriorating the image quality of the abdomen. Our experimental findings indicated that the presence of cylindrical phantoms exacerbated streaking artifacts, as evidenced by differences in signal values in air with and without these phantoms. We hypothesized that wrapping EWS sheets around cylindrical phantoms, the primary source of streaking artifacts, suppressed signal values, thus mitigating the artifacts. Validation results demonstrated that the utilization of EWS sheets significantly mitigated streaking artifacts. Nevertheless, the utilization of EWS sheets resulted in signal irregularities within the spherical phantom, with numerous artifacts emerging from high-signal regions on the phantom's bedside surface. The artifact induced a slight increase in the background signal value; however, there was no statistically significant difference compared to the scenario without the cylindrical phantom. Given that the streaking artifacts originating from the edges of the spherical phantom had minimal impact on its interior, it is anticipated that imaging with the EWS sheet encircling the patient's arm will effectively mitigate the artifacts.

To ensure image uniformity, seven distinct phantom configurations were employed, and an evaluation was conducted using a gray scale uniformity map in accordance with the NEMA method. This approach enabled the identification of areas exhibiting signal irregularities. To facilitate numerical comparisons, PIU values were calculated based on the grayscale uniformity map and referenced prior studies. The noticeable decrease in PIU was more pronounced with GRASP-VIBE compared to conventional VIBE, a phenomenon that can be attributed to the radial acquisition scheme used in GRASP-VIBE. Radial acquisitions allow for continuous sampling of the k-space center and provide robustness against motion artifacts. However, the presence of phase errors in k-space data can negatively impact image quality [12, 13]. These errors can be caused by echo shift resulting from inhomogeneities in the static magnetic field and imbalances in the imaging gradients, which are mainly caused by eddy currents. The EWS sheet utilized in this study comprises copper and carbon, both of which are conductive materials. Upon exposure to electromagnetic waves, conductors generate electric currents due to the force acting on free electrons. These currents manifest as eddy currents, creating a magnetic field around the conductor [14]. This magnetic field, in turn, induces static magnetic field inhomogeneity, leading to echo shift and subsequent phase errors, resulting in trajectory errors in k-space and variations in signal intensity in images. For the above reasons, the reduction in uniformity observed when utilizing the EWS sheet during GRASP-VIBE imaging is hypothesized to be attributable to eddy currents generated in the EWS sheet upon exposure to electromagnetic waves. In Cartesian acquisitions, such as conventional VIBE, rectilinear k-space undergoes uniform shifts and uniform phase errors across all lines [14]. Consequently, Cartesian acquisitions are less likely to degrade image quality due to phase errors. Changes in signal intensity in Cartesian acquisitions are likely attributed to the influence of the non-uniform RF magnetic field caused by RF waves reflected by the sheet and are confined to the vicinity of the sheet. Furthermore, in radial acquisitions, the disturbance of the static magnetic field by eddy currents varies based on the sheet's position, exerting different effects on the image. The use of EWS sheets on only one side of the cylindrical phantom exacerbates PIU reduction and image quality degradation. Therefore, when utilizing GRASP-VIBE with EWS sheets, it is recommended to

wrap EWS sheets around both arms to prevent a decline in image quality.

This study employed a phantom commonly used for MRI system maintenance. Although the experiments were conducted with a setup designed to simulate the human body, the shape and signal characteristics differ from those of actual biological tissue. Furthermore, in clinical settings, variations in subject body size and intra-abdominal tissue composition may result in differences in signal disturbances and their spatial manifestations. Subsequent validation utilizing volunteer studies and clinical data is imperative in future research. Additionally, this study was conducted under imaging conditions relevant to clinical settings, and images were evaluated following sensitivity correction processing. In 3T MRI systems, multi-channel coils are utilized, and sensitivity correction holds significant importance in clinical practice. However, the impact on images is expected to vary depending on the coils used and the distance from the specimen.

Conclusion

The application of an EWS sheet to cover the dependent arms during GRASP-VIBE imaging may potentially mitigate streaking artifacts in upper abdominal imaging. This approach could potentially enhance image quality at the lateral margins of abdominal organs in proximity to the arms. However, due to radial sampling, static magnetic field inhomogeneity induced by the EWS sheet may result in signal intensity variations within the FOV. Notably, the utilization of the sheet on a single arm may adversely affect image uniformity, thus rendering the application of sheets to both arms preferable. Furthermore, signal attenuation between the two sheets may potentially lead to image quality degradation. Consequently, prudence is warranted when employing this technique for examinations focusing on abdominal organs in the posterior region.

Disclosure Statement

The authors declare that they have no conflicts of interest.

References

1) Feng L, et al.: Golden-angle radial sparse parallel MRI: combination of compressed sensing, parallel imaging, and golden-angle radial sampling for fast and flexible dynamic volumetric MRI. Magn Reson Med, 72(3), 707-717, 2014.
2) Pan J, et al.: Image quality optimization: dynamic contrast-enhanced MRI of the abdomen at 3T using a continuously acquired radial golden-angle compressed sensing acquisition. Abdom Radiol (NY), 49, 399-405, 2024.
3) Lu Y, et al.: The value of GRASP on DCE-MRI for assessing response to neoadjuvant chemotherapy in patients with esophageal cancer. BMC Cancer, 19(1), 999, 2019.
4) Xue Y, et al.: Automatic coil selection for streak artifact reduction in radial MRI. Magn Reson Med, 67(2), 470-476, 2012.
5) Du J, et al.: Artifact reduction in undersampled projection reconstruction MRI of the peripheral vessels using selective excitation. Magn Reson Med, 51(5), 1071-1076, 2004.
6) Mandava S, et al.: Radial streak artifact reduction using phased array beamforming. Magn Reson Med, 81(6), 3915-3923, 2019.
7) Ono A, et al.: Effect of electromagnetic wave suppression sheet in magnetic resonance imaging system on radio-frequency-induced heating of metallic implant. JJMRM, 39(2), 55-59, 2019.
8) Ministry of Health, Labor and Welfare: Report of National Health and Nutrition Survey in Japan, 2019. Ministry of Health, Labor and Welfare, 122-123, 2020.
9) Ito K, et al.: Non-contrast MR angiography of the renal artery with golden angle radial sparse parallel-volumetric interpolated breath-hold examination: Optimal imaging conditions. JJMRM, 43(4), 174-181, 2023.
10) National Electrical Manufacturers Association: Determination of image uniformity in diagnostic magnetic resonance images. NEMA Standards Publication MS 3-2008.
11) Goerner FL, et al.: A comparison of five standard methods for evaluating image intensity uniformity in partially parallel imaging MRI. Med Phys, 40(8), 082302, 2013.
12) Moussavi A, et al.: Imperfect magnetic field gradients in radial k-space encoding-Quantification, correction, and parameter dependency. Magn Reson Med, 81(2), 962-975, 2019.
13) Moussavi A, et al.: Correction of gradient-induced phase errors in radial MRI. Magn Reson Med, 71(1), 308-312, 2014.
14) Hidaka K.: Introduction to Materials Designing for Electromagnetic Wave Shielding or Absorption. Seikei-Kakou, 34(1), 5-8, 2022.

Received April 1, 2025; accepted August 18, 2025

The Utility of SSIM for Determination of Target EI for Chest X-ray Imaging — Comparison and Examination of Visual Evaluation —

KITA Kento[1)]*, IDEGUCHI Tadamitsu[2)], TANAKA Nobukazu[2)], KATO Toyoyuki[3)], OHFUJI Takafumi[4)], TANAKA Ryouji[4)], IMOTO Nami[5)], TABATA Nariaki[6)], HAMADA Michi[7)], KUROYANAGI Hiroyuki[8)], KIJIMA Satoru[8)]

1) Department of Health Sciences, Graduate School of Medical Sciences, Kyushu University (Currently Division of Clinical Radiology Service, Kyoto University Hospital)
2) Department of Health Sciences, Faculty of Medical Sciences, Kyushu University
3) Division of Radiology, Department of Medical Technology, Kyushu University Hospital
4) Department of Radiological Technology, Department of Medical Technology, Kyushu Central Hospital
5) Division of Radiology, Saiseikai Fukuoka General Hospital
6) Department of Health Sciences, Graduate School of Medical Sciences, Kyushu University / Department of Radiology, Fukuoka University Chikushi Hospital
7) Department of Radiology, Fukuoka University Hospital
8) Sales Division MS Business Department, FUJIFILM Medical Co., Ltd.

* E-mail: ken.kita.523@gmail.com

Note: This paper is secondary publication, the first paper was published in the JART, vol. 72 no. 879: 21-30, 2025.

Key words: structural similarity (SSIM), target exposure index (EIt), deviation index (DI), noise suppression processing, paired comparison

【Abstract】

The purpose of this study was to evaluate the utility of structural similarity (SSIM) in setting target dose indices (EIt) for chest X-ray imaging. Specifically, we investigated the relationship between radiation dose, image quality changes due to noise reduction processing (Flexible Noise Control: FNC), and the correlation between visual assessment and SSIM.

The EIt, determined from clinical imaging data histograms, was used as the reference dose. Chest phantoms were imaged three times each at seven different dose levels: DI -3.0, -2.0, -1.0, 0.0, +1.0, +2.0, and +3.0. Noise reduction processing (FNC) was applied at seven levels (0.0, 0.2, 0.4, 0.5, 0.6, 0.8, and 1.0) to each image, resulting in a total of 147 images. SSIM was calculated for all combinations, and correlations between radiation dose, FNC, and SSIM were analyzed. Additionally, SSIM was computed for 24 image pairs (randomly combined from images with DI 0.0 and DI -3.0) with FNC applied at three levels (0.0, 0.5, 1.0). A visual assessment experiment was conducted by two radiologists with over 10 years of experience and four radiologic technologists using the Scheffe's paired comparison method, and the results were compared with the SSIM values.

SSIM reflected the radiation dose and the degree of FNC application. Similarly, visual assessment showed that higher SSIM values were associated with smaller interval scale values, indicating a correlation. Furthermore, the analysis suggested that the appropriate use of FNC could contribute to further reduction in radiation exposure.

In chest radiographs, SSIM was demonstrated to be a novel evaluation method that can easily determine the target exposure index EIt.

Introduction

Digitalization of X-ray imaging systems has provided various benefits, including rapid image acquisition and image processing aimed at facilitating accurate diagnosis. On the other hand, regarding radiation dose, ICRP Publication 93 warns that "radiological technologists are aware that overexposed images can be corrected by computer processing, whereas underexposure necessitates repeat examination; consequently, there is a tendency to deliver a higher dose than necessary." [1)] In Japan as well, several reports have indicated that patient radiation dose has increased compared with the period before the transition to digital systems. [2, 3)] One possible contributing factor is that, with the widespread adoption of modality worklist management (MWM), preset exposure parameters are automatically applied, thereby

reducing the need for detailed adjustment of imaging conditions according to the subject. [4] To optimize patient radiation exposure, it is necessary to standardize dose indicators among manufacturers and to unify quality control of clinical images. Accordingly, in 2008, the International Electrotechnical Commission (IEC) proposed the exposure index (EI) as a dose indicator. [5] For clinical implementation, it is necessary to establish a target exposure index (EIt) for each anatomical region that yields optimal image quality. [6] Two principal methods have been used to determine EIt. One is to operate the system for a certain period at each clinical facility and determine EIt from the histogram of EI values actually obtained for each anatomical region (hereafter, actual values), using the median, mode, or mean. [7] The other is to determine EIt by visual assessment using clinical images or anthropomorphic phantoms. [8, 9] Although both methods are constrained by time and labor, the use of actual values is easier to implement because of its simplicity. However, EIt derived from the median or mode of actual values does not necessarily represent the appropriate dose in terms of both patient exposure and image quality. Therefore, although visual assessment is ultimately the preferred method for determining EIt, it is difficult to implement in practice because it is complex and requires substantial time, manpower, and effort.

Against this background, we focused on structural similarity (SSIM). SSIM is an objective image quality assessment metric proposed by Wang et al. that indicates how similar two images are, and because it reflects human visual perception, it has been expected to serve as a new index that could substitute for visual assessment. [10] For this reason, it has been used in a variety of research fields, including MRI and CT. [11-16] However, because SSIM was originally defined for natural images, its usefulness in medical imaging must be demonstrated by investigating in detail the correlation between image quality and SSIM and, ultimately, by validating it against conventional visual assessment methods. Because SSIM is a metric for quantitatively evaluating similarity between two images, comparison with the paired comparison method [17-19] is most appropriate among visual assessment approaches. If a correlation is observed between these methods and SSIM, SSIM could be proposed as one of the new simple methods for determining EIt.

Therefore, in this study, we focused on methods for determining EIt in chest radiography and investigated the usefulness of SSIM.

1. Method

1-1 Objective Image Quality Metric: SSIM

SSIM is an image quality metric calculated using the pixel values of two images to be compared: a reference image and a comparison image. It is a quantitative value that indicates the degree to which the image structure of the comparison image resembles that of the reference image. SSIM is calculated from three components, namely luminance, contrast, and structure (noise), and takes a value closer to 1.0 as the similarity increases and closer to 0.0 as the similarity decreases. The SSIM representing the similarity between two images, x and y, is calculated using Eq. (1).

$$SSIM(x,y) = \left[l(x,y)^{\alpha} \times c(x,y)^{\beta} \times s(x,y)^{\gamma}\right] \quad \cdots\cdots\cdots (1)$$

Here, l, c, and s denote "luminance", "contrast", and "structure (noise)", respectively, and each factor is independent and calculated using Eqs. (2)-(4).

$$l(x,y) = \frac{2\mu_x\mu_y + C_1}{\mu_x^2 + \mu_y^2 + C_1}, \quad C_1 = (K_1 L)^2 \quad \cdots\cdots\cdots (2)$$

$$c(x,y) = \frac{2\sigma_x\sigma_y + C_2}{\sigma_x^2 + \sigma_y^2 + C_1}, \quad C_2 = (K_2 L)^2 \quad \cdots\cdots\cdots (3)$$

$$s(x,y) = \frac{\sigma_{xy} + C_3}{\sigma_x\sigma_y + C_3}, \quad C_3 = \frac{C_2}{2} \quad \cdots\cdots\cdots (4)$$

Here, μ_x and μ_y are the mean pixel values, σ_x and σ_y are the standard deviations, σ_{xy} is the covariance, and C_1 and C_2 are constants introduced to prevent the denominator from approaching zero. For SSIM calculation, we used the standard parameter settings based on the paper by Wang et al. [10]: $\alpha = \beta = \gamma = 1$, $K_1 = 0.01$, $K_2 = 0.03$, and $L = 255$. These settings have also been adopted in previous studies reporting the usefulness of SSIM for CT and X-ray images, [20, 21] and the same values were therefore used in the present study.

1-2 Imaging of the Chest Phantom

For SSIM calculation, corresponding 8 × 8-pixel regions of interest (ROIs) were placed at the same positions in the two images being compared, and SSIM was calculated while moving the ROI across the entire image without overlap; the mean value was then used (Fig. 1). The ROI size of 8 × 8 pixels was adopted on the basis of the method of Wang et al., considering a balance that would appropriately reflect fine differences in visual structure. Because evaluation of two images using SSIM requires the subject to be positioned in exactly the same location in both images, assessment using clinical images is difficult. Therefore, in this study, a chest phantom was used.

First, to determine the EIt to serve as the reference dose for chest phantom imaging, 3,831 clinical chest postero-anterior (PA) radiographs acquired at the three collaborating institutions were used (Table 1). Although EIt is usually established for each anatomical region at each institution, if a common EIt could be set across multiple institutions using the same detector, equivalent image quality might be ensured at the same radiation dose. Taking this into consideration, a provisional EIt was determined using data from multiple institutions. All EI data had been calibrated using a sensitivity index defined by the manufacturer with a calibrated dosimeter. In addition, use of these data was approved by the ethics committees of each institution (Kyudai-Ikyo-Sei No. 1425, Rinken No. 327, Approval No. 2021-2-5). Fig. 2 shows histograms created from the EI values of

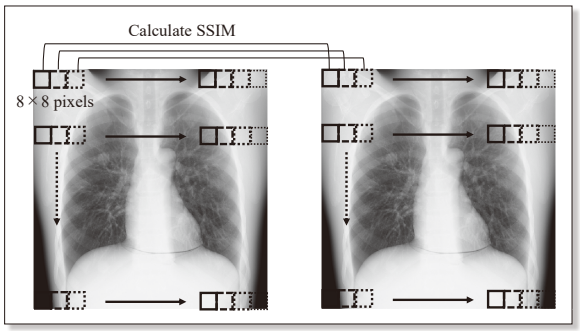

Fig. 1 Calculation method of SSIM in this study.

SSIM of 8×8 pixels ROIs at corresponding positions between the two images was calculated. This process was repeated by shifting the entire image to ensure the ROIs did not overlap, and SSIM values were then averaged.

Table 1 Detail of clinical data at each facility.

Facility Name	Number of Cases Male / Female	Age Average (Min-Max)
Hospital A	620 / 730	57.7 (0-90)
Hospital B	1,172 / 957	62.1 (0-100)
Hospital C	216 / 136	46.8 (20-90)

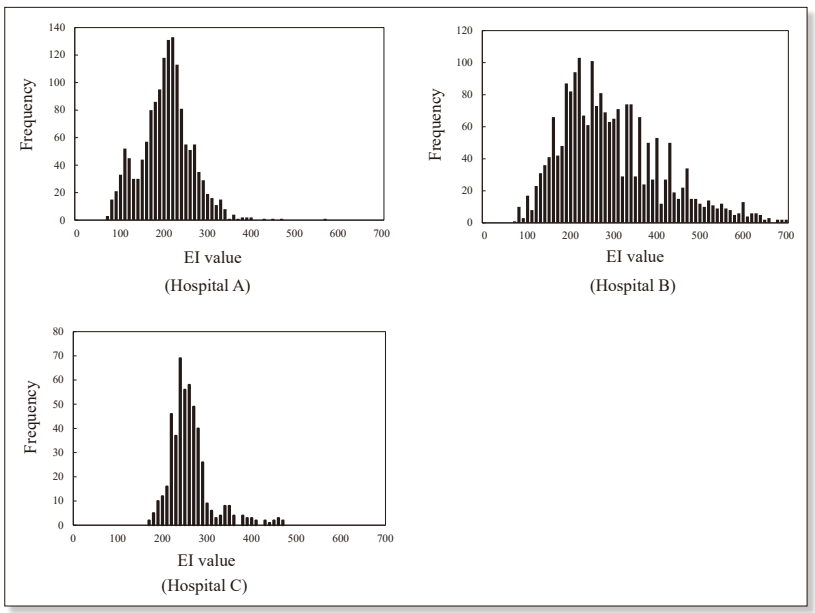

Fig. 2 Histograms of EI at each facility.

chest PA images from each institution. The modal EI values at the three institutions were 220, 250, and 210, and the mean of these values, 227, was adopted as the provisional EIt (hereafter, EIt). Using the imaging conditions corresponding to the determined EIt as the reference dose, chest phantom images were acquired under various conditions, and SSIM was calculated and analyzed. The chest phantom used for imaging was the N-1 LUNGMAN (Kyoto Kagaku Co., Ltd., Kyoto, Japan), and the X-ray detector was an indirect-conversion flat-panel detector (FPD), CALNEO SMART C47 (pixel size, 150 μm; FUJIFILM Medical Co., Ltd., Tokyo, Japan), which was the same FPD used at the three collaborating institutions. The anti-scatter grid used had a grid ratio of 12:1, a grid density of 60 lines/cm, and a focal distance of 200 cm (JPI Japan, Tokyo, Japan). Imaging was performed using an X-ray generator, CIRCLEX 0.6/1.2 P38DE-85 (Shimadzu Corporation, Kyoto, Japan). The tube voltage was fixed at 120 kV, tube current at 200 mA, and source-to-image distance (SID) at 200 cm, while the exposure time (ms) was adjusted so that the deviation index (DI) became −3.0, −2.0, −1.0, 0.0 (EIt), +1.0, +2.0, and +3.0. Chest phantom images were acquired three times at each of these seven dose levels. Here, DI was calculated as a deviation index from the difference relative to EIt and was used to evaluate whether the exposure dose was excessive or insufficient. Regarding the appropriate range of this value, Task Group 116 of the American Association of Physicists in Medicine (AAPM) defines ±0.5 as the appropriate range for imaging conditions; when DI exceeds +1.0, the dose is considered excessive, and when it is below −1.0, the dose is considered insufficient, and instructions from a radiologist should be sought regarding the need for repeat imaging; when it is −3.0 or less, repeat imaging is recommended.[22] Although the reference imaging dose was set to correspond to EIt 227 derived from the three institutions, owing to equipment characteristics, the imaging conditions shown in Table 2 were selected so that the EI values were as close as possible to those corresponding to each DI.

Table 2 Radiographic conditions for chest phantom.

DI	Calculated EI	EI acquired at exposure	tube current–time product (mAs)
-3.0	114	121	1.42
-2.0	143	150	1.8
-1.0	180	186	2.2
0.0	227 (EIt)	231	2.8
1.0	286	298	3.6
2.0	360	369	4.4
3.0	453	458	5.6

1-3 Correlation Between Exposure Dose and SSIM

Using the 21 chest phantom images acquired at the dose levels corresponding to each DI in Section 1-2, the correlation between exposure dose and SSIM was investigated. Of the two images used for SSIM calculation, the reference image was set to DI 0.0 (EIt), and the comparison image was set to DI −3.0, −2.0, −1.0, 0.0, +1.0, +2.0, or +3.0. For each dose condition (DI), three images were acquired, and SSIM was calculated for all combinations with the three images obtained under the reference condition (DI 0.0) (3 × 3 = 9 combinations), and the average value was used. The three components, "luminance", "contrast", and "structure (noise)", were calculated using Eqs. (2)-(4), and SSIM was finally obtained using Eq. (1). However, for DI 0.0, combinations of completely identical images (self-comparisons) were excluded because SSIM = 1.0; instead, SSIM was calculated and averaged for the three possible combinations among the three images acquired under the same condition. This enabled analysis that included image quality variation caused by factors such as quantum noise even under the same DI.

1-4 Correlation Between Noise Reduction Processing and SSIM: Comparison at Each Exposure Dose

Flexible noise control (FNC), a noise reduction process, has been reported to improve

graininess without reducing the response of the signal component [23, 24] and is routinely used in clinical chest radiography. Here, FNC was applied to the 21 phantom images acquired in Section 1-2 at seven enhancement levels: 0.0 (no processing), 0.2, 0.4, 0.5, 0.6, 0.8, and 1.0, yielding a total of 147 images for SSIM calculation. Of the two images used for SSIM calculation, the reference image was set to DI 0.0 (EIt), and the comparison image was set to DI −3.0, −2.0, and −1.0 in the underexposure range, as well as DI +1.0, +2.0, and +3.0 in the overexposure range. For all combinations of the three images at each dose level, SSIM of the chest phantom images was calculated and averaged. However, the same intensity of FNC processing was applied to both images when calculating SSIM. FNC 0.5 was the default setting for chest radiography and is currently used clinically at the three collaborating institutions, whereas the maximum FNC value was 1.0.

1-5 Visual Assessment and SSIM

Among the images acquired in Section 1-2, chest phantom images obtained at DI 0.0 (EIt 227) and DI −3.0 (EI 114), which AAPM Task Group 116 recommends should be repeated, were each processed with FNC at three levels—0.0 (no processing), 0.5 (clinical setting), and 1.0 (maximum setting)—to produce a total of six images for observation. Because SSIM is an index for quantifying image similarity between two images, it has already been noted that validation against visual assessment is best performed using the paired comparison method. Furthermore, among paired comparison methods, Scheffé's paired comparison method modified by Ura was used, considering the possibility that the order in which the observed images are presented may affect the observers' evaluation. [25] The observers consisted of two radiologists and four radiological technologists, all with more than 10 years of experience. Six images with varying exposure doses and FNC enhancement levels were randomly paired to prepare ${}_6P_2 = 30$ image pairs for observation. Among these, the final set consisted of 24 pairs in which EIt (DI 0.0) served as the reference image.

Before the experiment, the study procedures and protection of personal data were explained in writing, and informed consent was obtained from the observers. The observed images were displayed at actual size on a 3-megapixel monochrome LCD monitor, RadiForce GS320 (EIZO Co., Ltd., Ishikawa, Japan). The fluorescent lighting was adjusted so that the illuminance at the front of the monitor was 30 lx, and the grayscale characteristic was calibrated to the grayscale standard display function in accordance with the illuminance. First, the observers were asked to comprehensively evaluate the two presented chest radiographs. They were then asked to assess which image was superior in two regions, namely the "mediastinum/subdiaphragmatic region" and the "lung field," using a 7-point category scale ranging from 0 to ±3. As evaluation criteria, for the "mediastinum/subdiaphragmatic region," uniformity, graininess, and contrast with the lung field were emphasized, whereas for the "lung field," the indicators were contrast of the pulmonary vessels, uniformity of density, and the visibility of the boundaries of the ribs and diaphragm. The final evaluation was left to each observer's judgment based on experience and learning, [18] and the results were integrated as the overall observational outcome for the chest radiographs. Observation time and viewing distance were left unrestricted. The observer ratings were analyzed by analysis of variance, and mean preference scores were calculated and subjected to significance testing. [26] When there was no difference in image quality between two images, the obtained stimulus distance (interval scale value) approached 0, whereas a larger value indicated a greater difference in image quality. Correlation with visual assessment was investigated by comparing these values with SSIM. To calculate SSIM in local regions such as the "mediastinum/sub-

diaphragmatic region" and the "lung field," it is necessary to precisely extract the target region from the image and ensure complete positional correspondence of the ROI. Although the phantom placement was constant, slight fluctuations in pixel values due to noise and minor variations in pixel arrangement could affect the structural term (the *s* component). Therefore, there were some concerns regarding the reliability of SSIM in local regions, and in this study, comparative analysis was performed using SSIM for the entire chest radiograph.

2. Results

2-1 Correlation Between Exposure Dose and SSIM

Fig. 3a shows the results of SSIM calculation using DI 0.0 (EIt) as the reference image and images with DIs ranging from −3.0 to +3.0 as the comparison images. FNC was set to 0.0 for all images. As the exposure dose increased, that is, as the DI increased, the SSIM value also increased, showing a strong positive correlation (R = 0.987). The calculated results for luminance, contrast, and structure are shown in Fig. 3 b–d. Luminance and contrast showed values close to 1.0 at all DI levels. The calculated results for structure increased as the exposure dose increased and showed a strong positive correlation (R = 0.994). These findings indicate that the SSIM value was strongly influenced by the calculated results for structure (noise), and that the exposure dose was reflected in the SSIM results.

2-2 Correlation Between Noise Reduction Processing and SSIM

Fig. 4a shows the SSIM values according to the FNC enhancement level in the underexposure range, where DI 0.0 was used as the reference image and images with DIs of −3.0, −2.0, and −1.0 were used as the comparison images. Fig. 4b shows the SSIM calculation results according to the FNC enhancement level in the overexposure range, where the comparison images had DIs of +1.0, +2.0, and +3.0. When FNC was 0.0, the SSIM values between the reference-dose image and the underexposed images were 0.91 or lower; however, as the FNC enhancement level increased, the SSIM value increased, and all underexposed images reached 0.961–0.964 at FNC 1.0 (Fig. 4a). Next, in the overexposure range, the SSIM values were 0.925–0.935 at FNC 0.0 and increased gradually as the FNC enhancement level increased, reaching 0.970–0.971 for all overexposed images (Fig. 4b). Thus, the greater the FNC enhancement level, the greater the SSIM value.

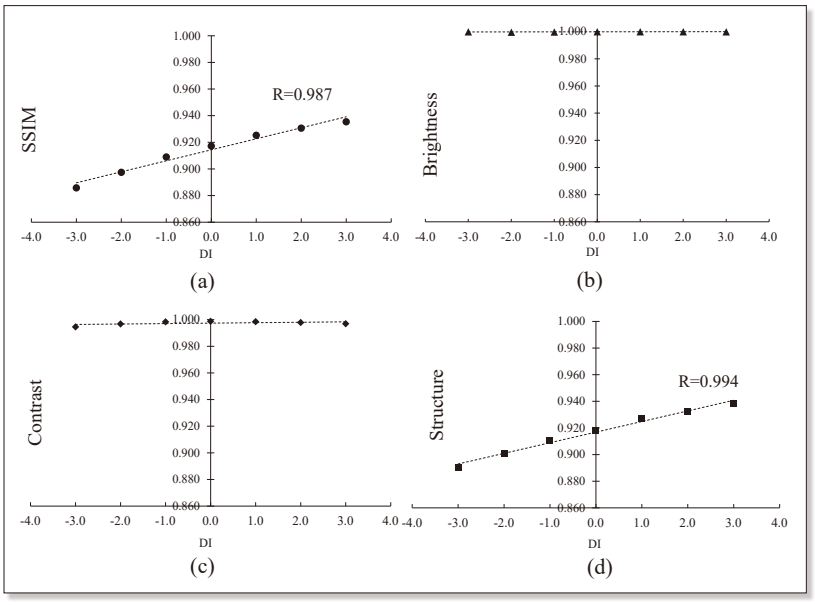

Fig. 3 SSIM in DI variations (FNC 0.0).
(a) SSIM (b) Brightness (c) Contrast and (d) Structure
Note: The point at DI = 0.0 corresponds to a comparison between separately acquired images obtained under identical imaging parameters.

2-3 Visual Assessment Results and SSIM

Fig. 5 shows the scores for the main effects derived from the results of the visual assessment using the paired comparison method on a yardstick. The image acquired at an underexposed dose with-

out FNC, which showed marked noise (DI −3.0, FNC 0.0), was located at the most negative end of the yardstick, whereas the image acquired at the reference dose and processed with the maximum level of noise reduction (DI 0.0, FNC 1.0) was located at the most positive end. The other images were also arranged along the scale according to image quality reflecting both exposure dose and the FNC enhancement level, indicating a correlation between the image quality of chest phantom radiographs and visual assessment by the paired comparison method. At this time, the 1% significance level on the yardstick was $Y_{0.01} = 1.1989$, and the 5% significance level was $Y_{0.05} = 1.0093$. Image pairs connected by solid lines showed significant differences at the 1% level (**), whereas those connected by dashed lines showed significant differences at the 5% level (*).

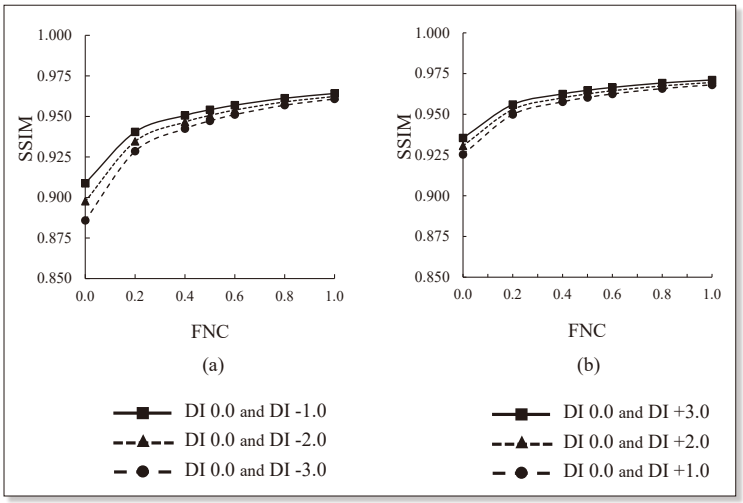

Fig. 4 Changes in SSIM for reference dose (DI 0.0) and low dose (DI −1.0, −2.0, −3.0) images, and reference dose and high dose (DI +1.0, +2.0, +3.0) images, with variations in the degree of FNC enhancement.
(a) Low dose range, (b) High dose range.

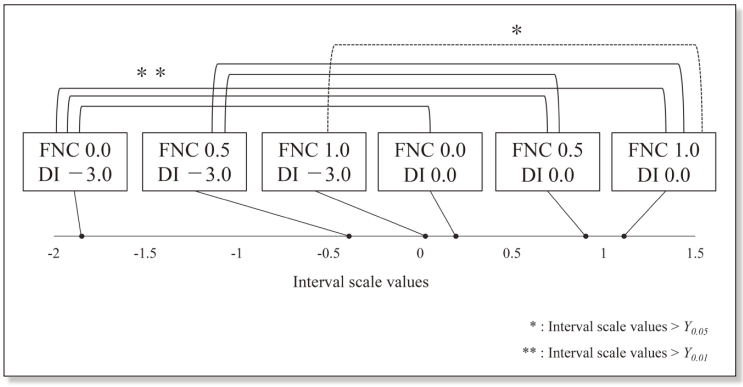

Fig. 5 Interval scale values using Scheffe's method are presented on a yardstick line.

Table 3 shows the SSIM values of the chest phantom images used in the paired comparison observer study, as well as the interval scale values between the two images and the results of significance testing. First, when the reference image (Image A) was the image obtained at DI 0.0 with FNC 0.0 (I), the SSIM values between this image and the comparison images (Image B) obtained at DI 0.0 with FNC 0.5 and 1.0 were 0.990 and 0.983, respectively, and no significant differences were observed in either comparison. Next, when the comparison image (Image B) was the image obtained at DI −3.0 with FNC 0.0, 0.5, or 1.0, the SSIM values were 0.887, 0.923, and 0.929, respectively, and a significant difference between the two images was observed only for the image pair with an SSIM of 0.887 ($P < 0.01$).

Next, when the reference image (Image A) was the image obtained at DI 0.0 with FNC 0.5 (II), the SSIM value relative to the comparison image (Image B) obtained at DI 0.0 with FNC 1.0 was as high as 0.997, and no significant difference was observed between the two images. Furthermore, when the comparison image (Image B) was the image obtained at DI −3.0 with FNC 0.0, 0.5, or 1.0, the SSIM values were 0.901, 0.940, and 0.948, respectively, and no significant difference was observed only for the image pair with FNC 1.0.

When the reference image (Image A) was the image obtained at DI 0.0 with FNC 1.0 (III), the SSIM values relative to the comparison images (Image B) obtained at DI −3.0 with FNC 0.0, 0.5, and 1.0

Table 3 Comparison of SSIM and interval scale values for each combination.

	Image A	Image B	SSIM	Interval scale values
	DI, FNC	DI, FNC		
Ⅰ	0.0, 0.0	0.0, 0.5	0.990	0.708
	0.0, 0.0	0.0, 1.0	0.983	0.917
	0.0, 0.0	−3.0, 0.0	0.887	2.042**
	0.0, 0.0	−3.0, 0.5	0.923	0.583
	0.0, 0.0	−3.0, 1.0	0.929	0.167
Ⅱ	0.0, 0.5	0.0, 1.0	0.997	0.208
	0.0, 0.5	−3.0, 0.0	0.901	2.750**
	0.0, 0.5	−3.0, 0.5	0.940	1.292**
	0.0, 0.5	−3.0, 1.0	0.948	0.875
Ⅲ	0.0, 1.0	−3.0, 0.0	0.904	2.958**
	0.0, 1.0	−3.0, 0.5	0.944	1.500**
	0.0, 1.0	−3.0, 1.0	0.952	1.083*

* : Interval scale values > $Y_{0.05}$ (Yardstick value by 5 % significance level) = 1.0093
** : Interval scale values > $Y_{0.01}$ (Yardstick value by 1 % significance level) = 1.1989

were 0.904, 0.944, and 0.952, respectively, and significant differences were observed for all image pairs (FNC 0.0 and 0.5: $P < 0.01$; FNC 1.0: $P < 0.05$).

3. Discussion

In the relationship between exposure dose and SSIM in chest phantom imaging, the calculated values for luminance and contrast were nearly 1.0 at all dose levels (Fig. 3b, c). One possible explanation is the effect of density stabilization processing based on the image histogram, namely exposure data recognizer (EDR2) [27], whereby luminance and contrast may have been maintained at constant levels regardless of exposure dose. Therefore, the SSIM values at each exposure dose can be considered to have strongly reflected noise between the two images, that is, the calculated result for structural difference (Fig. 3a, d). The exposure dose used for phantom imaging and SSIM showed an extremely strong positive correlation, demonstrating a correlation between exposure dose and SSIM values in medical X-ray images. A more detailed analysis of the graph in Fig. 3a showed that, in the overexposure range (DI>0), the SSIM values increased more gradually and exhibited less change than in the underexposure range. This may be because a sufficient number of photons for image formation had already reached the detector.

Next, regarding the correlation between FNC and SSIM, the SSIM value increased at all dose levels as the FNC enhancement level increased, and the differences became minimal at FNC 1.0. At 50% of the reference dose (DI −3.0), the SSIM value increased from 0.886 at FNC 0.0 to 0.964 at FNC 1.0, indicating a high degree of image similarity to the reference-dose image (Fig. 4a). Furthermore, for combinations of the reference image at DI 0.0 (EIt) and comparison images in the overexposure range, the SSIM values at FNC 0.0 were 0.925, 0.931, and 0.935 for each DI, whereas at FNC 1.0, they were 0.968, 0.970, and 0.971, respectively. As in the underexposure range, the SSIM value increased as the FNC enhancement level increased, although the degree of increase was more gradual (Fig. 4b). As in Fig. 3, this may be attributable to the number of photons incident on the detector; when the dose reaching the detector is sufficient, image noise is also reduced. Conversely, in the underexposure range, fewer photons reach the detector, and the FNC noise reduction process may therefore function more appropriately and effectively than in the overexposure range, resulting in a greater increase in SSIM. Thus, the greater the enhancement level of noise reduction processing, the higher the SSIM value, indicating a correlation between them.

The FPD used in this study is equipped with a new graininess-improvement process (FNC2), developed by FUJIFILM Medical and combined with dynamic processing. This technique has been reported to possess the capability to apply filters according to the recognized structural pattern and to reduce noise components superimposed on subject structures. [28] The SSIM re-

sults suggested that, by appropriately adjusting this FNC processing, even underexposed images that would otherwise warrant consideration of repeat imaging may be brought closer to the image quality obtained at the reference dose.

Next, the results of the visual assessment experiment using the paired comparison method were compared with the SSIM values calculated from the chest phantom images (Table 3). The results showed that SSIM is a useful metric that reflects the overall image quality of chest radiographs. A detailed analysis of the SSIM values between two images and the stimulus distances (interval scale values) obtained by the paired comparison method showed that smaller SSIM values tended to be associated with larger interval scale values, whereas larger SSIM values tended to be associated with smaller interval scale values. Regression analysis of these two parameters yielded an estimated SSIM of 0.975 when the interval scale value was zero, that is, when no difference between the two images was estimated. The P value was 0.0139, indicating a statistically significant relationship. Next, the relationship between SSIM and the interval scale value was quantitatively analyzed, and the SSIM satisfying the condition of no statistically significant difference was determined by logistic regression analysis. As a result, SSIM ≥ 0.941 was identified as the threshold at which the image quality of two chest radiographs is judged to be equivalent. However, for a more stringent determination, it would be preferable to use either a value greater than 0.952, which was the maximum SSIM among image pairs that showed a significant difference, or 0.975, at which the interval scale value becomes zero, as the threshold. It should be noted that the SSIM between two images acquired at DI 0.0 (same dose, no filter processing) was approximately 0.917 despite the absence of any visually perceptible difference. This is because quantum noise and variation in exposure dose affect the structural term (covariance) of SSIM. In contrast, the threshold of SSIM ≥ 0.941 for "visually equivalent" images should be interpreted as an index applicable to "systematic changes in conditions", such as dose variation and FNC filtering, and is conceptually different from variation within the same condition (e.g., the DI 0.0 case in Fig. 3).

In the present visual assessment, when the reference image was DI 0.0 with FNC 0.5, an image acquired at DI −3.0, corresponding to 50% of the reference dose, showed an SSIM of 0.948 when FNC was set to 1.0 and was judged to show "no significant difference" in the visual assessment. This result satisfies the condition of SSIM ≥ 0.941 derived from logistic regression analysis, indicating that increasing FNC from 0.5 to 1.0 may enable dose reduction of up to 50%. However, it is considered appropriate for each institution to select and establish the threshold cautiously according to its own judgment. The guideline of the Japan Image and Information Management Association (JIIMA) Standardization Committee, although intended for validation of natural image compression, states that an SSIM of 0.98 or higher indicates that "the images are indistinguishable," an SSIM of 0.9 to 0.98 indicates "a level at which degradation can be recognized upon magnification," and an SSIM below 0.9 indicates "a level at which degradation is clearly recognizable." [29] In the present study, the SSIM of 0.975 corresponding to an interval scale value of zero was very close to the JIIMA guideline value of 0.98, at which images are considered indistinguishable. The other SSIM values also showed close agreement with the results of visual assessment.

Several points should be noted when using SSIM to determine EIt. As described above, the "luminance", "contrast", and "structure" included in the SSIM formula are represented by Eqs. (2)-(4). Among these, the L value representing dynamic range was set to 255, even for 14-bit images, in accordance with the proposal of Maruyama, [21] in order to subjectively capture subtle fluctuations due to quantum noise in

medical images. In addition, although the standard parameter settings proposed by Wang et al. and adopted in previous studies were used in the present study, detailed investigation of the optimal parameters for medical X-ray images remains a subject for future study.

Next, attention should be focused on the structure (noise) term in Eq.(4). When two images are acquired under the same X-ray exposure conditions and observed by humans, they are generally judged to have almost the same image quality. Because SSIM reflects human visual perception, it should theoretically yield a value close to 1.0. However, the SSIM between

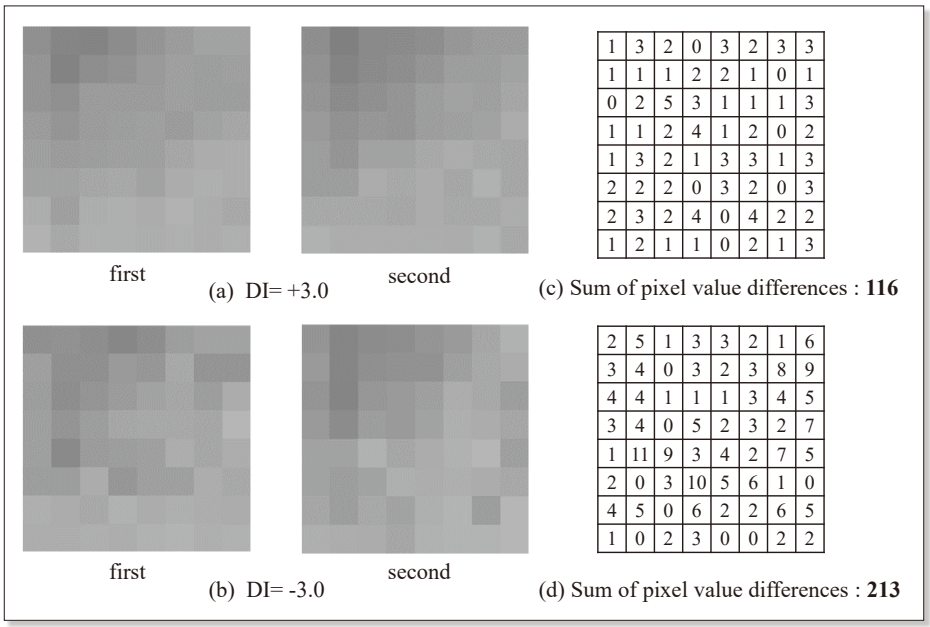

1	3	2	0	3	2	3	3
1	1	1	2	2	1	0	1
0	2	5	3	1	1	1	3
1	1	2	4	1	2	0	2
1	3	2	1	3	3	1	3
2	2	2	0	3	2	0	3
2	3	2	4	0	4	2	2
1	2	1	1	0	2	1	3

2	5	1	3	3	2	1	6
3	4	0	3	2	3	8	9
4	4	1	1	1	3	4	5
3	4	0	5	2	3	2	7
1	11	9	3	4	2	7	5
2	0	3	10	5	6	1	0
4	5	0	6	2	2	6	5
1	0	2	3	0	0	2	2

Fig. 6 Comparison of close-up radiographs acquired at the same dose level (8×8 pixels).
(a) Images were acquired at a deviation index (DI) of +3.0 in two separate exposures.
(b) Images were acquired at a deviation index (DI) of –3.0 in two separate exposures.
(c), (d) The digital values of each pixel obtained by subtracting two images.

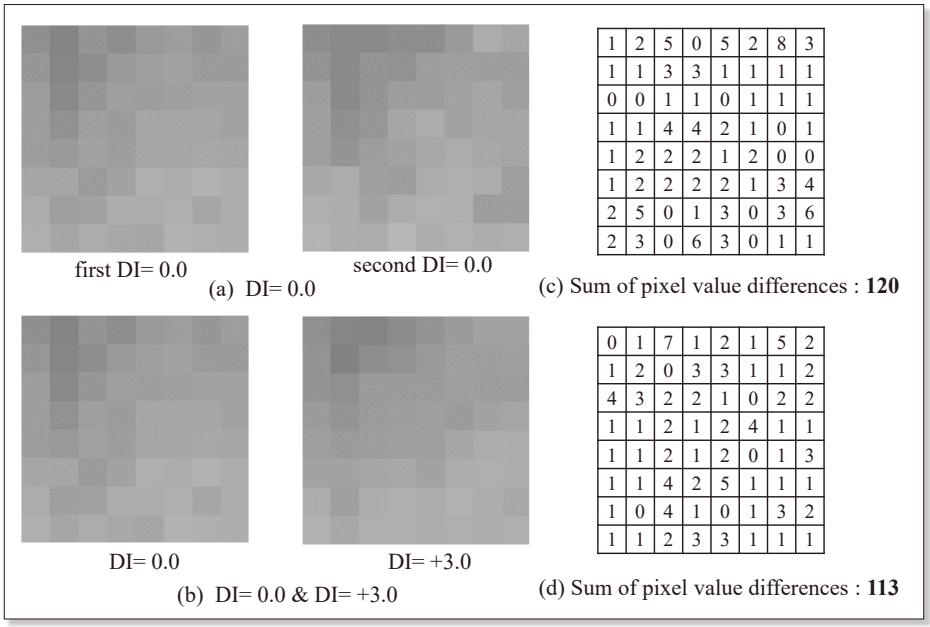

1	2	5	0	5	2	8	3
1	1	3	3	1	1	1	1
0	0	1	1	0	1	1	1
1	1	4	4	2	1	0	1
1	2	2	2	1	2	0	0
1	2	2	2	2	1	3	4
2	5	0	1	3	0	3	6
2	3	0	6	3	0	1	1

0	1	7	1	2	1	5	2
1	2	0	3	3	1	1	2
4	3	2	2	1	0	2	2
1	1	2	1	2	4	1	1
1	1	2	1	2	0	1	3
1	1	4	2	5	1	1	1
1	0	4	1	0	1	3	2
1	1	2	3	3	1	1	1

Fig. 7 Comparison of close-up radiographs acquired at the same or different dose levels (8×8 pixels).
(a) Images were acquired at a deviation index (DI) of 0.0 in two separate exposures.
(b) Images were acquired at a deviation index (DI) of 0.0 & +3.0 in separate exposures.
(c), (d) The digital values of each pixel obtained by subtracting two images.

two images acquired at the same dose of DI 0.0 was 0.912 (Fig. 3a). Furthermore, the SSIM between DI 0.0 and higher-dose images acquired at DI +1.0, DI +2.0, and DI +3.0 increased to 0.925, 0.930, and 0.935, respectively, showing a positive correlation. As noted above, the luminance and contrast parameters used in SSIM calculation were close to 1.0 regardless of exposure dose, indicating that the SSIM value was strongly influenced by the structural equation, Eq.(4). The structural difference term, $s(x, y)$, in SSIM quantifies differences in "noise distribution" by calculating the covariance of pixel values at corresponding positions between the two images. [10] The value of this structural term, $s(x, y)$, became markedly lower as the reference image became lower in dose. Fig. 6 shows enlarged 8 × 8-pixel images of the subdiaphragmatic region from phantom images acquired twice under the same conditions. Fig. 6a shows images acquired at DI +3.0, and Fig. 6b shows images acquired at DI −3.0; no FNC processing was applied in either case. Fig. 6c and Fig. 6d show the differences in pixel values at corresponding positions between the two images. As the dose decreased, the differences in pixel values at corresponding positions became greater (Fig. 6c, d), substantially affecting the covariance calculation. Because human observers visually average such pixel-level noise distributions, when the reference image is obtained at an extremely low dose, a discrepancy is more likely to arise between the SSIM value and the visual assessment result. Fig. 7a shows enlarged 8 × 8-pixel images of the subdiaphragmatic region from phantom images acquired twice at the same dose of DI 0.0, whereas Fig. 7b shows similar enlarged images acquired at DI 0.0 and DI +3.0. Fig. 7c and Fig. 7d show the differences in pixel values at corresponding positions. The sum of the pixel-value differences between DI 0.0 and DI +3.0 was smaller than that between the two DI 0.0 images, which helps explain the result obtained for the structure calculation.

Taken together, these findings suggest that SSIM may be applicable as an objective metric capable of substituting for visual assessment in the establishment of EIt. Future investigations will include evaluation of SSIM variability, visualization of image quality changes through the introduction of local SSIM maps in the local regions used for visual assessment (e.g., the lung field and subdiaphragmatic region), and more detailed assessment using multiscale ROIs, with the aim of establishing a more sophisticated methodology for determining EIt.

4. Conclusion

In this study, we investigated a method for applying SSIM to the determination of EIt on the basis of its correlation with visual assessment. SSIM was shown to enable objective and simple quantitative evaluation of image quality, and the established threshold (SSIM ≥ 0.941) indicated that image quality can be judged at a level equivalent to that of visual assessment. These findings suggest that this approach may contribute to a new method for determining EIt that reduces the burden of visual assessment while enabling both dose optimization and image quality assurance.

Conflicts of interest

This study was conducted with technical support from FUJIFILM Medical Co., Ltd. In addition, this study was supported by grants from FUJIFILM Medical Co., Ltd. (Nos. 31-4134 and 2022-861). Two of the co-authors are employees of FUJIFILM Medical Co., Ltd. The other authors have no conflicts of interest to disclose.

Acknowledgments

The authors would like to express their sincere gratitude to the faculty members of the Department of Health Sciences, Kyushu University Graduate School, and to the staff of the

Division of Radiology, Kyushu University Hospital, for their cooperation in the visual assessment experiment conducted in this study. The authors also wish to express their heartfelt appreciation to Professor Emeritus Junji Morishita of Kyushu University for his continued guidance and support.

Presentation at a Scientific Meeting

A summary of this study was presented at the 80th Annual Scientific Meeting of the Japan Society of Radiological Technology (Yokohama, 2024).

References

1) ICRP Publication 93. Managing patient dose in digital radiology, 2004.
2) Suzuki S, et al.: The Interim Report of Investigative Research on Patient Exposure Doses in Diagnostic X-ray Examinations. Japanese Journal of Radiological Technology, 65, 681-685, 2009.
3) Suzuki S, et al.: The Interim Report No. 2 of Investigative Research on Patient Exposure Doses in Diagnostic X-ray Examinations. Japanese Journal of Radiological Technology, 65, 1582-1589, 2009.
4) Kishimoto K, et al.: Study of Appropriate Dosing in Consideration of Image Quality and Patient Dose on the Digital Radiography. Japanese Journal of Radiological Technology, 67, 1381-1397, 2011.
5) IEC62494-1: Medical electrical equipment –Exposure index of digital X-ray imaging systems, Part 1, Definitions and requirements for general radiography, Ed. 1, 2008.
6) Zhang M, et al.: A method to derive appropriate exposure parameters from target exposure index and patient thickness in pediatric digital radiography. Pediatric radiology, 43, 568-574, 2013.
7) Dave JK, et al.: Current state of practice regarding digital radiography exposure indicators and deviation indices: Report of AAPM Imaging Physics Committee Task Group 232. Med Phys, 45, 1146-1160, 2018.
8) Nakamae M: Study of the Reliability of Visual Evaluation by the Ranking Method: Analysis of Ordinal Scale and Psychological Scaling Using the Normalized-rank Approach. Japanese Journal of Radiological Technology, 56, 725-730, 2000.
9) Fukao M, et al.: Optimization of dual-energy subtraction chest radiography by use of a direct-conversion flat-panel detector system. Radiological Physics and Technology, 8, 46-52, 2015.
10) Wang Z, et al.: Image Quality Assessment: From Error Visibility to Structural Similarity. IEEE TRANSACTIONS ON IMAGE PROCESSING, 13, 600-612, 2004.
11) Zimmermann L, et al.: An MRI sequence independent convolutional neural network for synthetic head CT generation in proton therapy. Zeitschrift fur medizinische Physik, 32, 218-227, 2022.
12) Zhu Z, et al.: Compressed Sensing-Based MRI Reconstruction Using Complex Double-Density Dual-Tree DWT. Int J Biomed Imaging, 907501, 2013.
13) Zhu Y, et al.: Removal of high density Gaussian noise in compressed sensing MRI reconstruction through modified total variation image denoising method. Heliyon, 6, e03680, 2020.
14) Zhu Y, et al.: Sinogram domain metal artifact correction of CT via deep learning. Computers in biology and medicine, 155, 106710, 2023.
15) Zhu M, et al.: Structure-preserved meta-learning uniting network for improving low-dose CT quality. Phys Med Biol, 67, 2022.
16) Zhu H, et al.: Temporally downsampled cerebral CT perfusion image restoration using deep residual learning. International journal of computer assisted radiology and surgery, 15, 193-201, 2020.
17) Scheffé H: An analysis of variance for paired comparisons. J Am Stat Assoc, 47, 381-400, 1952.
18) Nakamae M, et al.: Method of Subjective Evaluation by Scheffe's Method of Paired Comparisons. Japanese Journal of Radiological Technology, 52, 1561-1565, 1996.
19) Nakamae M: Theory of Statistical Sensory Evaluation and Its Application to Radiological Technology Science: Focusing on Scheffé's Method of Paired Comparisons. Japanese Journal of Radiological Technology, 66, 1502-1507, 2010.
20) Yamada S, et al.: Perceptual Image Dissimilarity: A Novel Metric for Objective Assessment of Image Quality in Computed Tomography with Iterative Reconstruction. Japanese Journal of Medical Physics, 34, 35-46, 2014.
21) Maruyama S: Properties of the SSIM metric in medical image assessment: Correspondence between measurements and the spatial frequency spectrum. Physical and Engineering Sciences in Medicine, 46, 1131-1141, 2023.
22) AAPM (American Association of Physicists in Medicine): An Exposure Indicator for Digital Radiography, AAPM report No.116, July 2009.
23) Iwasaki N: Flexible Noise Control (FNC). Fujifilm Medical Review, 12, 25-32, 2004.
24) MacCutcheon DW: Management of pediatric radiation dose using Fuji computed radiography. Pediatr Radiol, 34, S201-206, 2004.
25) Ura S: Analysis of Paired Comparison Experiments. Hinshitsu Kanri (Statistical Quality Control), 10(2), 78-80, 1959.
26) Takagi H: Practical Statistical Tests and Machine Learning III: Significance Tests for Human Subjective Tests. Systems, Control and Information, 58(12), 514-520, 2014.
27) Furukawa K, ed.: Chapter 9. Digital Images and Image Processing. In: Radiographic Photography: From Analog to Digital. 2nd ed. Tokyo: FUJIFILM Medical Co., Ltd., 199-204, 2018.
28) Takahashi T, et al.: Improving X-ray Image Quality based on Human-Body Thickness and Structure Recognition. Fujifilm Research & Development, (62), 28-34, 2017.
29) Kobako M: Toward Standardization: Report of the Standardization Committee (3), Guidelines for Image Compression of Electronic Documents. Journal of Image and Information Management, 50(5), 21-24, 2011.

Received July 8, 2024; accepted October 22, 2024

Survey on Imaging Techniques for Autopsy Imaging CTs in Japan

TASHIRO Masami, Ph.D.[1)*], KOBAYASHI Tomoya, Ph.D.[2)], MEIJO Atsushi[3)], MATSUI Daiki[4)], KANEZAWA Chie[5)], ENDO Hirotaka[6)], FUKAYA Masato[6)], MIYATA Takeshi[6)], IDONUMA Shunei[7)], KUDO Yasuyuki[8)], KURITA Junichiro[8)], SAITO Tsukasa[9)], WATANABE Satoshi[3)]

1) Department of Radiological Sciences, School of Health Science, Fukushima Medical University
2) Department of Clinical Imaging, Graduate School of Medicine, Tohoku University
3) Department of Central Radiology, Iwaki City Medical Center
4) Department of Imaging Center, Kita Fukushima Medical Center
5) Department of Radiology, Fukushima Medical University Hospital
6) Department of Radiology, Ohta Nishinouchi Hospital, Ohta General Hospital
7) Department of Radiology, Hoshi General Hospital
8) Department of Radiology, Takeda General Hospital
9) Department of Radiology, Aidu Chuo Hospital

* E-mail: masamit@fmu.ac.jp

Note: This paper is secondary publication, the first paper was published in the JART, vol. 72 no. 868: 26-33, 2025.

Key words: Autopsy Imaging, CT, Postmortem CT, Ai-CT

【Abstract】
The purpose of this study was to investigate the current practices of imaging protocols for postmortem CT examinations (Autopsy imaging CT: Ai-CT). A questionnaire survey was conducted, and data regarding facility information, CT equipment information, and imaging protocols were collected from 132 facilities nationwide in Japan. As a result, 39 combinations of imaging protocols were identified. CT automatic exposure control (CT-AEC) was used in many facilities. The results suggest that imaging protocols for Ai-CT examinations vary from facility to facility and are not standardized. The findings of this study are expected to contribute to the establishment of standardized Ai-CT imaging protocols in the future and to benefit both the forensic and clinical fields.

Introduction

Postmortem CT (Autopsy imaging CT: Ai-CT) is a non-invasive method used to examine the internal structures of a deceased person's body. Ai-CT is performed to determine the cause of death due to trauma or disease, providing detailed internal information. When used in conjunction with conventional autopsy, Ai-CT enables more accurate determination of the cause of death [1)]. In the field of forensic medicine, it is used to elucidate the cause and circumstances of death, serving as a means to uncover evidence of crimes and the background of incidents [2)]. Furthermore, Ai-CT is useful in investigating medical accidents and malpractice, as well as in pathological research, allowing comparisons between clinical diagnoses and pathological findings [3)]. Compared with conventional autopsies, Ai-CT can be performed more rapidly and hygienically, with the added benefit of reducing the psychological burden on the bereaved family [4)]. Thus, Ai-CT plays an important role in determining the cause of death and investigating medical accidents.

The roles of radiological technologists in Ai-CT are diverse. Most importantly, they are required to set appropriate imaging conditions and perform the scan. Furthermore, utilizing their medical knowledge, technologists must provide optimal images for cause-of-death investigations and forensic inquiries [5)]. Through these roles, radiological technologists enhance the reliability and reproducibility of Ai-CT examinations, serving as key personnel in supporting more accurate cause-of-death determi-

nations and medical accident investigations.

The "Role of Radiological Technologists in Ai – Ai Examination Guidelines –" (hereafter, the Guidelines), published in 2017 [6], details the procedures for Ai-CT examinations and the roles of radiological technologists. These Guidelines were created by the Japan Association of Radiological Technologists (JART) and serve as a reference in many facilities. However, more than seven years have passed since their publication, during which CT equipment has continued to advance. Examples of such advancements include improved spatial resolution, reduced radiation doses [7], and the development of advanced image analysis software [8]. Furthermore, new image reconstruction methods, such as iterative reconstruction (IR) and metal artifact reduction (MAR), have been continuously introduced [9, 10]. Consequently, the current imaging conditions used in Ai-CT examinations may no longer align with the contents of the Guidelines created seven years ago.

The purpose of this study was to investigate the current practices of imaging protocols in Ai-CT examinations. Specifically, a nationwide survey was conducted regarding the current usage of CT equipment, scanning sequences, and imaging parameters to clarify existing practices. This survey aimed to contribute to the revision of the existing Guidelines and to improve the reliability of Ai-CT examinations.

1. Materials and Methods

1-1. Subjects

The subjects were medical professionals who had performed Ai-CT examinations, regardless of facility type (e.g., hospitals, university facilities, or research laboratories). Although the majority of these professionals were radiological technologists, in university facilities or other institutions without technologists, physicians or other medical staff involved in the procedures were also included.

1-2. Questionnaire Contents

The survey consisted of 20 items divided into three categories: facility information, CT equipment information, and imaging conditions (Fig. 1). With the exception of a few open-ended items, predefined multiple-choice options were provided, and respondents selected the applicable answers. The imaging conditions section

Q1.	Please provide the name of your facility.
Q2.	Please provide the approximate average number of postmortem CT examinations per month at your facility.
Q3.	Please indicate the installation location of the CT equipment used for postmortem CT examinations.
Q4.	Please indicate the manufacturer of the CT equipment used for postmortem CT examinations.
Q5.	Please indicate the model name of the CT equipment used for postmortem CT examinations.
Q6.	Please indicate the detector element width (mm).
Q7.	Please indicate the number of detector rows.
Q8.	If the anatomical regions are divided as follows, please indicate how you combine them for scanning: "Brain, Face, Neck, Chest, Abdomen, Pelvis, Thigh, Lower leg, Foot"
Q9.	Please indicate the tube voltage setting for each series.
Q10.	Please indicate the reconstruction slice thickness (displayed image slice thickness) for each series.
Q11.	Please indicate the acquisition slice thickness (thinnest reconstructable slice thickness) for each series.
Q12.	Please indicate the scan time (time/rotation) for each series.
Q13.	Please indicate the reconstruction kernel for each series.
Q14.	Please describe the usage of CT-AEC.
Q15.	Please describe the settings of the automatic exposure control (CT-AEC).
Q16.	Please describe the method for setting the reconstruction FOV.
Q17.	Please describe the use of metal artifact reduction (MAR: Metal Artifact Reduction).
Q18.	Please describe the use of iterative reconstruction.
Q19.	Please indicate whether limitations due to X-ray tube heat capacity occur during postmortem CT examinations.
Q20.	Please provide any comments regarding the imaging methods for postmortem CT examinations.

Fig. 1 Questionnaire on imaging methods for Ai-CT examinations

was based on the parameters described in "Standardization in X-ray CT Imaging: GALACTIC" [11]. By collecting information in a format consistent with this standard, the results could potentially serve as a basis for future guideline development.

1-3. Consent Procedures and Ethical Considerations

Initially, participants were recruited through mailing lists of academic societies related to postmortem imaging. Interested individuals were then asked to submit their names, affiliated institutions, and contact information (email addresses) via an online application form. The form provided detailed explanations of the following: the purpose and significance of the study; that the aim was to investigate actual imaging practices of Ai-CT and that no patient personal information would be collected; that respondents' personal information would be used solely for research purposes; that participants could withdraw at any time, even after submitting the questionnaire; and that the results would be presented at academic conferences and published in journals. Informed consent was thereby obtained.

Participants provided their consent by clicking a consent button on the agreement form after understanding the above explanations. This study was conducted with the approval of the Ethics Committee of Fukushima Medical University (Approval Number: REC2024-037, Date of Approval: May 28, 2024).

1-4. Statistical Analysis

IBM SPSS Statistics Version 29 (IBM, Armonk, NY, USA) was used to tabulate and analyze the collected data. Descriptive statistics were performed on the questionnaire responses.

2. Results

2-1. Facility Information

Responses were obtained from 132 facilities. The installation locations of the CT equipment and the average number of cases per month are shown in Table 1. The average number of Ai-CT cases per month was less than 1 in 19.7% (26 facilities), 1 to less than 10 in 53.0% (70 facilities), 10 to less than 30 in 22.0% (29 facilities), 30 to less than 50 in 3.8% (5 facilities), and 50 or more in 1.5% (2 facilities). Regarding the location of the CT equipment, general clinical departments in hospitals were the most common at 64.4% (85 facilities), followed by hospital emergency centers at 25.8% (34 facilities). University departments included 6 research laboratories/departments (4.5%) and 4 cause-of-death investigation centers (3.0%). Other locations, including an autopsy center and a clinic, accounted for 3 facilities (2.2%).

2-2. CT Equipment Information

The CT equipment used was categorized by four manufacturers. Canon Medical Systems

Table 1 Installation location of CT equipment and average number of Ai-CT examinations per month

		Average number of cases per month					
		Less than 1	1 to less than 10	10 to less than 30	30 to less than 50	More than 50	Total
Location of CT equipment	Hospital (General clinical departments)	21	52	11	1	0	85
	Hospital (Emergency centers)	5	13	14	2	0	34
	University Department (Laboratories, etc.)	0	2	2	0	1	5
	University Department (Centers, etc.)	0	2	0	1	1	4
	Other	0	1	2	1	0	4
	Total	26	70	29	5	2	132

was the most common, with 82 facilities (62.1%), followed by GE Healthcare with 25 facilities (18.9%), Siemens Healthineers with 21 facilities (15.9%), and FUJIFILM Healthcare with 4 facilities (3.0%).

Table 2 shows the detector element widths and the number of detector rows along the z-axis. Equipment with a detector element width narrower than 1.0 mm accounted for 128 units (97.0%), while those with a width of 1.0 mm or greater accounted for 4 units (3.0%). All units were multi-slice CTs; no single-detector-row CTs were included.

2-3. Imaging Conditions Information

2-3-1. Setting of the Imaging Range and Scanning Sequences

To ascertain the scanning sequences, the following question was asked using a multiple-response checkbox format (Fig. 2): "If the anatomical regions are divided as follows, please indicate how you combine them for scanning: Brain, Face, Neck (Cervical spine), Chest, Abdomen, Pelvis, Thigh, Lower leg, Foot." To identify general trends, when regions were selected in multiple scan sequences, they were assigned to the sequence covering the region closest to the head.

In all responses, continuous scanning was performed from the brain without interruption. The inferior margin of the imaging range was the chest in 1 facility (0.8%), the pelvis in 22 facilities (16.7%), the thigh in 22 facilities (16.7%), the lower leg in 4 facilities (3.0%), and the foot in 83 facilities (62.9%).

A total of 39 patterns of scanning sequences were identified. The top 8 patterns are shown in Fig. 3. The most common sequence was scanning from the brain to the neck (cervical spine) first, followed by scanning from the

Table 2 Detector element width and number of detector rows

		Number of detector rows along the z-axis [Row]						
		4	16	64	80	128	256	320
Detector element width [mm]	0.25	0	0	0	1	0	0	0
	0.5	0	11	9	40	2	1	22
	0.6	0	1	7	0	3	1	0
	0.625	0	1	26	0	0	2	0
	0.8	0	0	1	0	0	0	0
	1.0	1	2	0	0	0	0	0
	1.2	0	1	0	0	0	0	0
Total		1	16	43	41	5	4	22

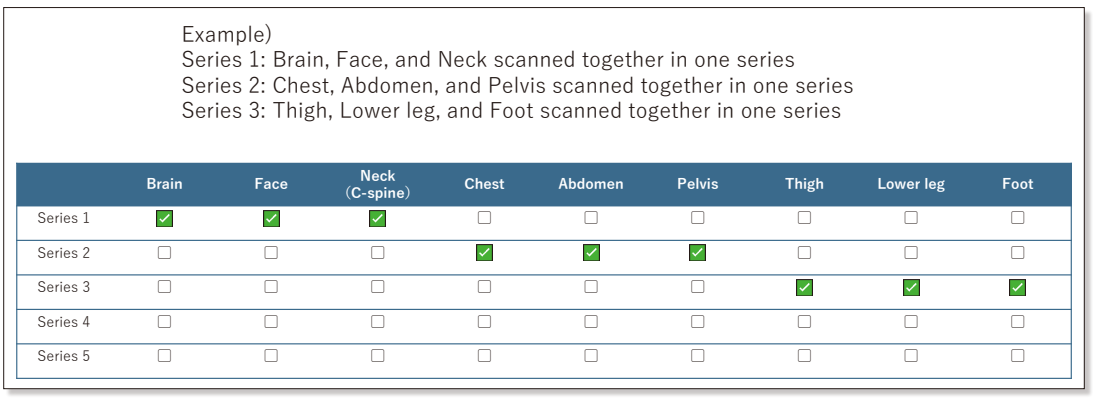

Fig. 2 Examples of imaging range settings and scanning sequences

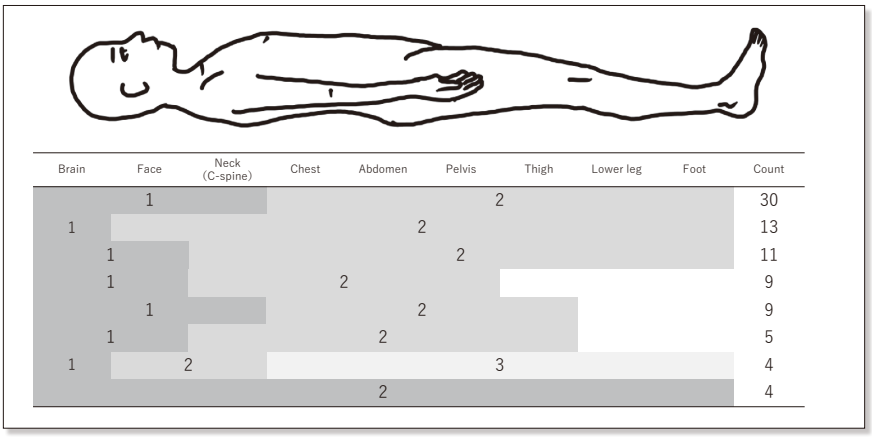

Fig. 3　Results regarding the imaging range and scanning sequences

chest to the foot. The differences among the multiple sequence patterns were primarily based on the boundary between the brain-to-neck scan and the subsequent scan, as well as the inferior margin of the total imaging range.

2-3-2. Setting of Scan Parameters

The usage of CT automatic exposure control (CT-AEC) is shown in Fig. 4a. "Used in all series" was reported by 88 facilities (66.7%), "Used in most series" by 15 facilities (11.3%), "Used in some series" by 10 facilities (7.6%), "Not used in any series" by 15 facilities (11.3%), "Cannot be used" by 2 facilities (1.5%), and other responses by 2 facilities (1.5%). Regarding CT-AEC settings (Fig. 4b), 68 facilities (51.5%) responded "Set to deliver a higher X-ray dose than the clinical setting," 40 facilities (30.3%) responded "Almost the same as the clinical setting," 5 facilities (3.8%) responded "Set to deliver a lower X-ray dose than the clinical setting," 14 facilities (10.6%) responded "CT-AEC is not used," and 5 facilities (3.8%) provided other responses.

Regarding the occurrence of limitations due to X-ray tube heat capacity (Fig. 4c), 58 facilities (43.9%) responded "Never occurs," 56 facilities (42.4%) responded "Rarely occurs," 12

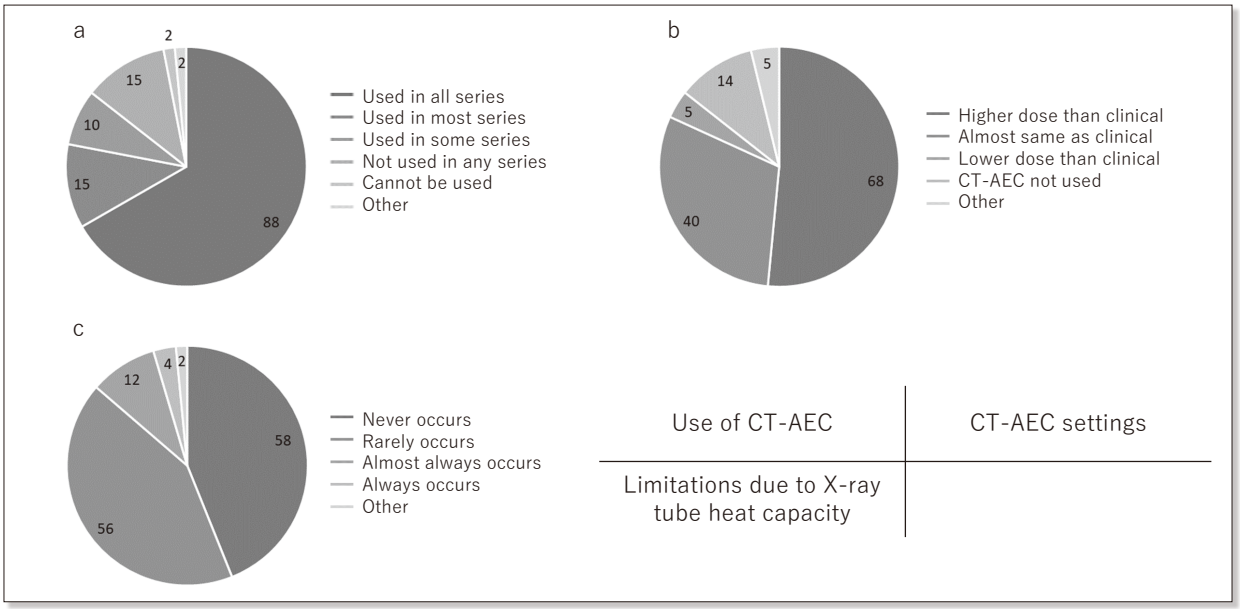

Fig. 4　Results regarding scan parameter settings

a. Use of CT-AEC, b. CT-AEC settings, c. Limitations due to X-ray tube heat capacity

facilities (9.1%) responded "Almost always occurs," 4 facilities (3.0%) responded "Always occurs," and 2 facilities (1.5%) provided other responses.

2-3-3. Image Reconstruction Settings

The methods for setting the reconstruction field of view (FOV) are shown in Fig. 5a. "Adjusted for each body to include the extremities" was reported by 59 facilities (44.7%), "Adjusted for each body to encompass the trunk" by 43 facilities (32.6%), "Always uses a fixed FOV" by 14 facilities (10.6%), "Always uses the maximum FOV" by 7 facilities (5.3%), and other responses by 9 facilities (6.8%).

The use of MAR is shown in Fig. 5b. "Always used" was reported by 2 facilities (1.5%), "Used when considered necessary" by 52 facilities (39.4%), "Sometimes used when considered necessary" by 35 facilities (26.5%), "Available but not used" by 15 facilities (11.4%), "Cannot be used" by 26 facilities (19.7%), and other responses by 2 facilities (1.5%).

The use of IR is shown in Fig. 5c. "Always used" was reported by 73 facilities (55.3%), "Used when considered necessary" by 28 facilities (21.2%), "Sometimes used when considered necessary" by 7 facilities (5.3%), "Available but not used" by 15 facilities (11.4%), "Cannot be used" by 5 facilities (3.8%), and other responses by 4 facilities (3.0%).

2-3-4. Relationship Between CT-AEC Settings and Scan Parameters

The relationship between CT-AEC settings and the use of IR is shown in Fig. 6a. IR was used in more than 50% of facilities regardless of the CT-AEC setting. Notably, in the group where the X-ray dose was set lower than the clinical setting, approximately 80% of facilities reported always using IR, indicating active use of this technology.

The relationship between CT-AEC settings and limitations due to X-ray tube heat capacity is shown in Fig. 6b. Differences were observed depending on the CT-AEC setting. With settings nearly identical to clinical settings, approximately 40% of facilities experienced no limitations related to X-ray tube heat capacity. When settings aimed for a higher X-ray dose, the proportion of facilities experiencing no heat capacity limitations increased. Conversely,

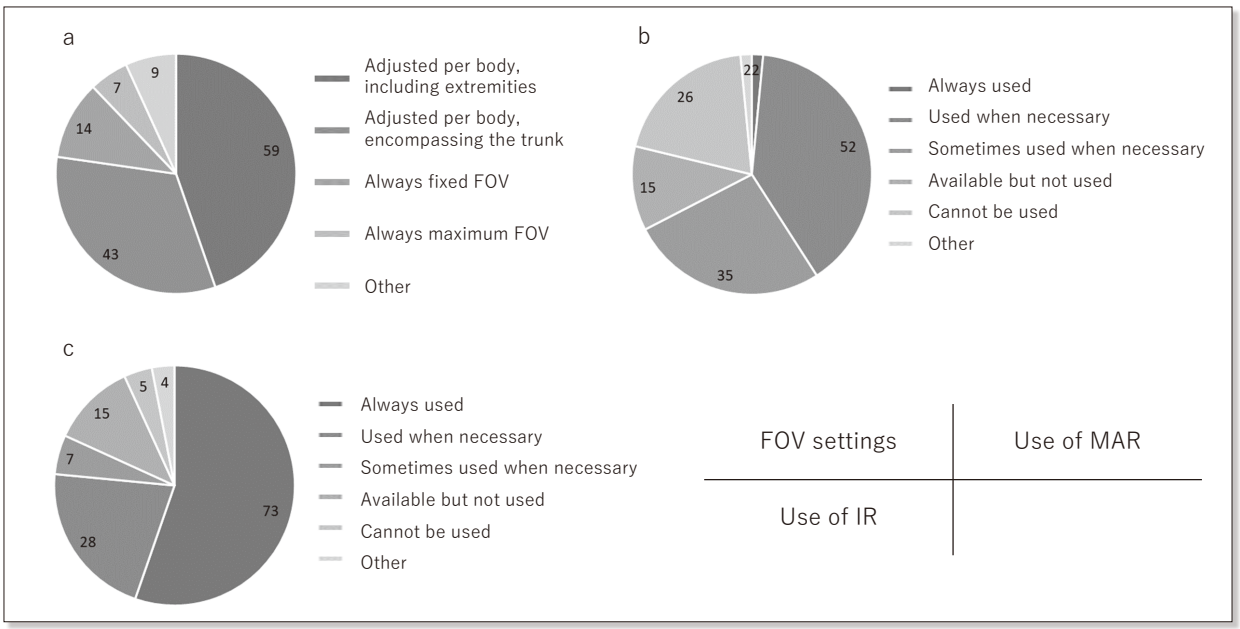

Fig. 5 Results regarding image reconstruction settings
a. FOV settings, b. Use of MAR, c. Use of IR

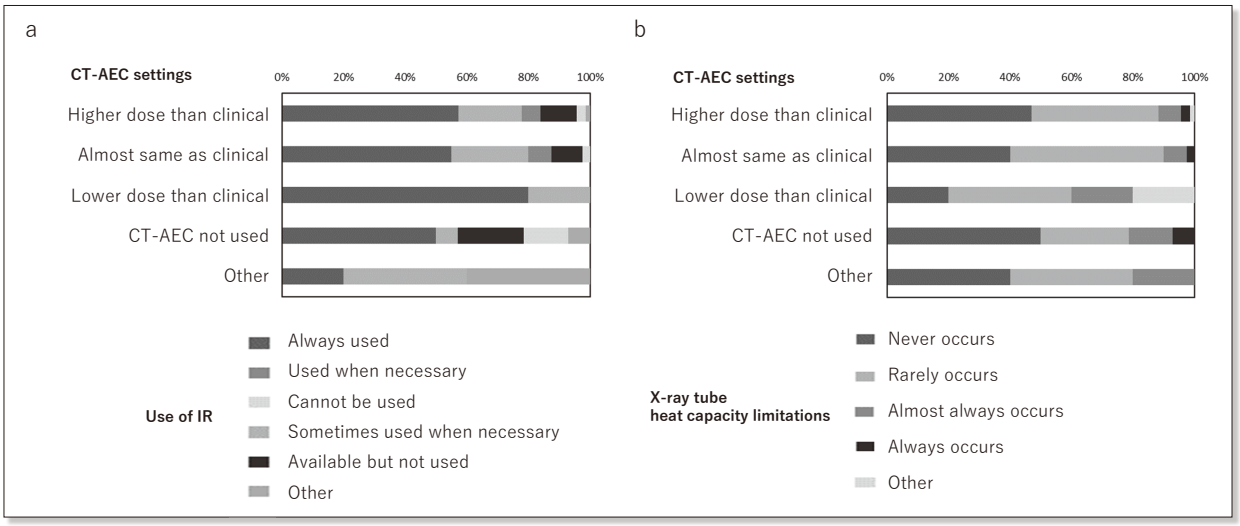

Fig. 6 Relationship between CT-AEC settings and scan parameters

a. Relationship between CT-AEC settings and the use of IR
b. Relationship between CT-AEC settings and limitations due to X-ray tube heat capacity

when settings aimed for a lower X-ray dose, the proportion of facilities experiencing no limitations decreased.

3. Discussion

The average number of Ai-CT examinations per month ranged widely from less than 1 to 50 or more, suggesting that examination volumes vary considerably depending on facility size and specialty. University departments specializing in Ai-CT tended to have higher annual examination volumes. Among hospitals, emergency centers tended to handle more cases than general clinical departments. In emergency centers, cases in which an individual's condition rapidly deteriorates due to trauma or acute illness, leading to death, occur frequently. Because Ai-CT can be performed in a short time and excels at depicting fractures and air distribution, it is considered an effective means for the rapid determination of the cause of death [12].

The CT equipment used for Ai-CT appears to have become increasingly sophisticated. The vast majority of detector element widths were less than 1.0 mm, suggesting that systems suitable for acquiring high-resolution images have become mainstream. All units along the z-axis were multi-slice CTs, enabling both high-speed scanning and thin-slice acquisition [13]. Because this also enables the creation of multiplanar reconstruction (MPR) images and three-dimensional images, it is expected to contribute to improved diagnostic accuracy in Ai-CT examinations [14].

Various patterns existed regarding the setting of the imaging range. The survey results showed that continuous scanning from the brain downward was performed in all cases. This indicates that comprehensive whole-body scanning is required in postmortem CT examinations for cause-of-death determination and detailed pathological analysis. The Guidelines also address the imaging range [6], suggesting that scanning down to the lower extremities (at least to the knees) is necessary to cover systemic lesions. However, there was inter-facility variability in the inferior margin of the scan range; while 83 facilities (62.9%) scanned down to the feet, some facilities did not image the lower extremities. This difference may be attributable to each facility's operational policies, the performance of their CT equipment, and the specific objectives of the examinations.

It became evident that scanning sequences

varied considerably among facilities. The existence of 39 combination patterns indicates that each facility selects its optimal scanning method according to its specific needs and equipment characteristics. In particular, there was inter-facility variability in the boundary between the brain-to-neck (cervical spine) scan and the subsequent scan, as well as in the extent of the imaging range to the lower extremities. This variability could affect the consistency and reproducibility of examination results, potentially making comparison and interpretation difficult. Therefore, standardization of the imaging range and scanning sequences is warranted.

CT-AEC was utilized in many facilities. CT-AEC is a function that automatically adjusts the radiation dose and is expected to contribute to dose optimization for each subject. Although radiation dose reduction is not a concern in Ai-CT, CT-AEC is considered to be used for mitigating X-ray tube heat capacity limitations and ensuring uniform image quality [15]. The finding that the largest proportion of facilities used CT-AEC in all series suggests that its utility is widely recognized. X-ray tube heat capacity limitation is an important issue in Ai-CT examinations, as it affects examination efficiency. Although the majority of facilities reported that heat capacity limitations rarely or never occurred, a certain number of facilities did experience them. This variation may be attributable to differences in CT equipment performance and examination conditions.

The FOV was adjusted individually for each body in most facilities. The finding that 102 facilities adjusted the FOV for each body indicates that a flexible approach is the mainstream practice. This method is considered important for obtaining optimal images tailored to the size and anatomical features of the body. The Guidelines recommend scanning with the maximum FOV [6]. However, uniformly using a fixed or maximum FOV may lack flexibility. In particular, when there are significant differences in body size or pathology, a fixed FOV may not yield appropriate images due to spatial resolution constraints [16]. Nevertheless, a fixed FOV may be adopted in some facilities because it contributes to simplicity in settings and consistency, depending on operational policies or technical constraints.

MAR was utilized in many facilities. MAR is a processing technique that suppresses metal artifacts, and the survey suggested that it is used on an as-needed basis in many institutions. Reasons for not using MAR may include the complexity of selecting appropriate settings from the various types available. Additionally, MAR can sometimes introduce noise across the entire image or degrade overall image quality [17], which may have led some facilities to refrain from using it. On the other hand, the high proportion of facilities using MAR as needed suggests that its utility is recognized to a certain extent.

IR was also utilized in many facilities. More than half of the surveyed facilities responded that they “always use” IR, indicating a high regard for its utility. This technology significantly contributes to noise reduction and image quality improvement [9]. In postmortem CT examinations, where contrast agents are rarely used, images with high low-contrast detectability are required, making the use of IR particularly important. A certain number of facilities responded “Available but not used” or “Cannot be used.” The Guidelines state that indiscriminate use of IR should be avoided [6]. Furthermore, smaller facilities or those with limited budgets may find it difficult to adopt the latest technologies.

The use of IR and the incidence of X-ray tube heat capacity limitations varied depending on the CT-AEC settings. When CT-AEC was set to deliver a lower X-ray dose, a greater proportion of facilities always used IR. This is likely because IR was employed to compensate for the increased image noise resulting from the reduced radiation output. Conversely, when

the X-ray dose was set higher, the frequency of IR use decreased. Regarding X-ray tube heat capacity limitations, an inverse trend was observed relative to the CT-AEC settings. Specifically, when set to a lower X-ray dose, the proportion of facilities experiencing no heat capacity limitations decreased, while the proportion experiencing such limitations increased. This seemingly paradoxical finding is considered to be dependent on the inherent performance of the CT equipment. Normally, reducing the X-ray dose decreases the load on the X-ray tube. However, in practice, heat capacity limitations are heavily influenced by differences in equipment specifications. In other words, facilities equipped with systems having a low X-ray tube heat capacity may have been compelled to reduce the X-ray dose, or the limitations may have occurred precisely because the heat capacity of their equipment was inherently low, resulting in this observed correlation.

Further investigation is required for the standardization of Ai-CT imaging techniques. Although this survey performed descriptive statistics on the questionnaire responses, it did not address individual scan parameters in detail. Settings such as tube voltage, slice thickness, and scan time vary considerably depending on the performance of the CT equipment. Similarly, the survey did not investigate whether radiological technologists were exclusively responsible for performing Ai-CT scans. In the future, it will be necessary to examine the setting of imaging conditions according to CT equipment specifications, including these factors. This will enable comparisons with the existing guidelines [11].

This survey investigated the current practices of imaging protocols in Ai-CT examinations. Previous surveys conducted in Japan have focused primarily on implementation systems and costs [18], or have presented imaging methods from single institutions [19, 20]; no survey specifically focusing on imaging techniques has been conducted. The same holds true internationally [21], underscoring the significance of this study for the standardization of imaging protocols. The survey results suggest that imaging protocols for Ai-CT vary from facility to facility and lack standardization. Furthermore, the appropriate use of image reconstruction technologies such as MAR and IR is expected to contribute to improving the image quality of Ai-CT examinations. It is considered important to deepen the understanding of these technologies and to use them at the appropriate timing. By revealing the current state of Ai-CT imaging methods, this study has highlighted existing issues and inter-facility variability. Based on these findings, the data can serve as a foundation for developing standardized protocols in the future. As a next step, it is expected that specific protocol proposals and guideline revisions will be undertaken based on this data. This would enable the consistent implementation of high-quality Ai-CT examinations nationwide, contributing to improved diagnostic reliability.

Conflicts of Interest

The first author and all co-authors have no conflicts of interest to disclose.

Acknowledgments

We would like to express our sincere gratitude to all individuals who cooperated in this survey.

References

1) Roberts Ian S. D., et al.: Post-mortem imaging as an alternative to autopsy in the diagnosis of adult deaths: a validation study. The Lancet, 379 (9811), 136-142, 2012.
2) Ikeda N.: Forensic usefulness and issues of post-mortem imaging. Fukuoka Igaku Zasshi, 101(2), 27-33, 2010. (in Japanese)
3) Yamamoto S.: Ai and Medical Accident Investigation System. J Jpn Soc Clin Anesth, 39(7), 748-752, 2019. (in Japanese)
4) Shiraiwa Y, et al.: The significance of the autopsy imaging (Ai) in Japanese corpse examination: From the interview with a bereaved family of traffic accident experienced judicial autopsy. Jpn J Human Environ Stud, 16(1), 25-34, 2018. (in Japanese)
5) Kobayashi Tomoya, et al.: Roles of radiological technologists at Tsukuba Medical Examiner's Office equipped with a computed tomography system dedicated for the examination of corpses. Forensic Imaging, 30, 200508, 2022.
6) Japan Association of Radiological Technologists (ed.): Role of Radiological Technologists in Ai (Autopsy imaging) - Ai Examination Guidelines. 2017. (in Japanese)
7) Muramatsu Y, et al.: Performance Evaluation for CT-AEC (CT Automatic Exposure Control) Systems. Jpn J Radiol Technol, 63(5), 534-545, 2007. (in Japanese)
8) Krupinski E. A., et al.: Choosing a radiology workstation: technical and clinical considerations. Radiology, 242(3), 671-682, 2007.
9) Geyer Lucas L., et al.: State of the Art: Iterative CT Reconstruction Techniques. Radiology, 276(2), 339-357, 2015.
10) Meyer E., et al.: Normalized metal artifact reduction (NMAR) in computed tomography. Med Phys, 37(10), 5482-5493, 2010.
11) Takagi T, et al.: Standardization in X-ray CT imaging: GALACTIC. Publishing Committee of the Japanese Society of Radiological Technology, 2015. (in Japanese)
12) Sakamoto N, et al.: Questionnaire survey on the current status and problems of postmortem imaging in critical care medical centers nationwide. The Japanese Journal of Acute Medicine, 33(8), 985-989, 2009. (in Japanese)
13) Tsujioka K.: Principles of multislice CT. Jpn J Radiol Technol, 56(12), 1391-1396, 2000. (in Japanese)
14) Ford Jonathan M., et al.: Computed tomography slice thickness and its effects on three-dimensional reconstruction of anatomical structures. Journal of Forensic Radiology and Imaging, 4, 43-46, 2016.
15) Ikuta K, et al.: Investigation of image quality uniformity using CT automatic exposure control. Matsue City Hospital Med J, 16(1), 21-24, 2012. (in Japanese)
16) Tsujioka K, et al.: Practice of CT examination (1): Setting scan parameters. Jpn J Radiol Technol, 58(11), 1456-1460, 2002. (in Japanese)
17) Shiraishi T, et al.: Usefulness of metal artifact reduction processing in CT examinations. Kochi Red Cross Hospital Med J, 27(1), 17-20, 2022. (in Japanese)
18) Tashiro K, et al.: Current status and prospects of Ai in Ibaraki Prefecture based on questionnaire results. InnerVision, 33(12), 51-55, 2018. (in Japanese)
19) Usui A, et al.: Operation and actual examination/diagnosis at the Autopsy Imaging Center of Tohoku University. InnerVision, 33(1), 42-44, 2018. (in Japanese)
20) Tashiro M, et al.: Role of radiological technologists at the Cause of Death Investigation Center, Fukushima Medical University. InnerVision, 33(12), 37-40, 2018. (in Japanese)
21) Arthurs Owen J., et al.: Current status of paediatric post-mortem imaging: an ESPR questionnaire-based survey. Pediatric Radiology, 44(3), 244-251, 2014.

Received July 26, 2024; accepted December 17, 2024

Examination of the optimal imaging angle for lateral X-rays of the knee joint in a standing position with both legs

HORIKAWA Ryota[1)]*, SHIMIZU Yuya[2)], KITANO Syoma[2)], SUZUKI Tomohiro[2)], ABE Takashi[2)]

1) Department of Brain Function Imaging Development, National Center for Geriatrics and Gerontology
2) Department of Radiology, National Center for Geriatrics and Gerontology

* E-mail: horikawa.ryota.rc@mail.hosp.go.jp

Note: This paper is secondary publication, the first paper was published in the JART, vol. 72 no. 871: 20-26, 2025.

Key words: knee osteoarthritis, knee joint lateral X-rays

【Abstract】
This study aimed to determine the optimum imaging angle suitable for lateral radiography of the knee joint in a standing position with both legs. The femoral rotation angle for knee rotation correction was determined from the knee joint X-ray computed tomography image as the corrected angle of limb position. Next, the X-ray incidence angle for abduction correction was determined from the frontal X-ray image of the knee joint in a standing position with both legs. As a result, the inward femoral rotation angle was 84.6 degrees. The X-ray incidence angle was 3.2 degrees in the cephalocaudal direction when aligned with the supratibial articular line, and 5.4 degrees in the cephalocaudal direction when aligned with the intra-external subcondylar edge line of the femur. This study clarified the optimum imaging angle for lateral X-ray photography of the knee joint in a standing position with both legs.

Introduction

In an aging society, X-ray imaging is essential for evaluating musculoskeletal disorders such as locomotive syndrome, which can lead to a decline in standing and walking function. X-rays used to evaluate locomotive syndrome must be taken in a standing position, not a supine position. [1)]

Knee osteoarthritis (knee OA) is a representative disease that causes musculoskeletal disorders in weight-bearing joints. In the severity classification and the progression or clinical course of knee OA, evaluation using frontal X-ray images of the knee joint in a standing position has become the standard, and the Kellgren-Lawrence classification is widely used. Standing positions include the extended and flexed positions, and it is believed that flexed imaging allows for a more accurate evaluation of the minimum joint space width. [2, 3)] However, this study was conducted based on frontal images in the extended position to determine the optimal angle for lateral imaging in a natural standing position with both legs.

X-ray imaging is considered superior for depicting joint space narrowing and alignment changes, as it is easier to perform in a standing position compared to X-ray computed tomography (CT) or magnetic resonance imaging (MRI). Furthermore, in two-directional joint imaging, it is essential to perform lateral imaging in the same position as the frontal imaging.[3)] Nevertheless, although many facilities perform frontal imaging with both legs in a standing position, current practice is to perform lateral imaging in a supine rather than a standing position. Even in facilities that adopt standing imaging, the positions used vary widely. [4)]

While lateral images in a standing position are in demand, Omori et al. [5)] reported a study on lateral knee X-ray imaging in a single-leg standing position. However, from the perspective of safety and reproducibility, our center

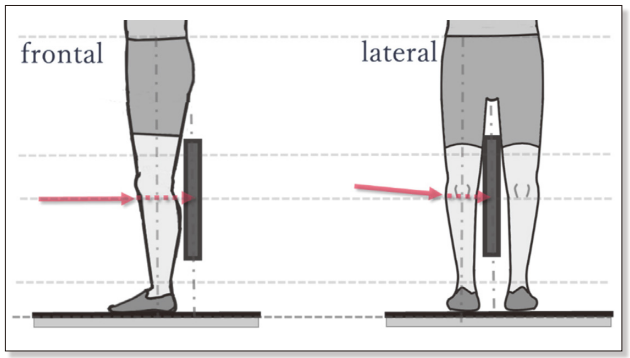

Fig. 1 X-ray of knee joint in standing position with both legs

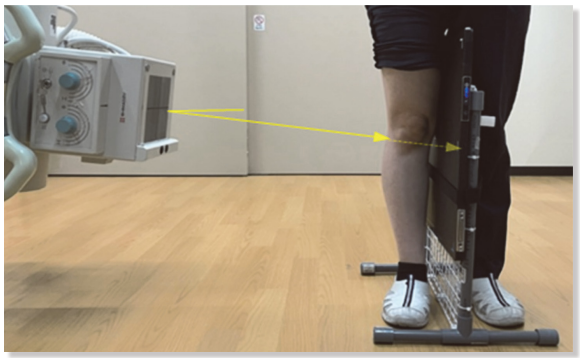

Fig. 2 Lateral X-ray of knee joint in standing position with both legs

adopts a standing position with both legs (Fig. 1), which allows for the same position in both frontal and lateral imaging.

In actual lateral knee X-ray imaging in a standing position with both legs (hereafter, standing lateral imaging), after performing frontal knee X-ray imaging in a standing position with both legs (hereafter, standing frontal imaging), the body is turned sideways from the position used for standing frontal imaging. As shown in Fig. 2, with the X-ray receiver placed in the imaging auxiliary tool, the patient stands with both legs (natural standing position) straddling the X-ray receiver, and the X-rays are directed from the lateral to the medial side of the knee joint. The imaging auxiliary tool is one introduced by the Bone and Joint Imaging Subcommittee of the Japan Association of Radiological Technologists.

For a lateral image of the knee joint, as shown in Fig. 3, both the medial and lateral condyles of the distal femur must be aligned for proper laterality, and the X-ray beam must be directed tangentially to the superior tibial articular surface (hereafter, the tibial plane) [3]. In clinical images of knee OA, alignment abnormalities such as rotation of the lower leg and femur occur due to the loss of knee joint cartilage [6]. Therefore, for the positioning of laterality in lateral imaging, it is necessary to consider two-axis correction in the rotational and abduction directions, as shown in Fig. 4.

The purpose of this study was to determine

Fig. 3 Lateral X-ray image of knee joint in standing position with both legs

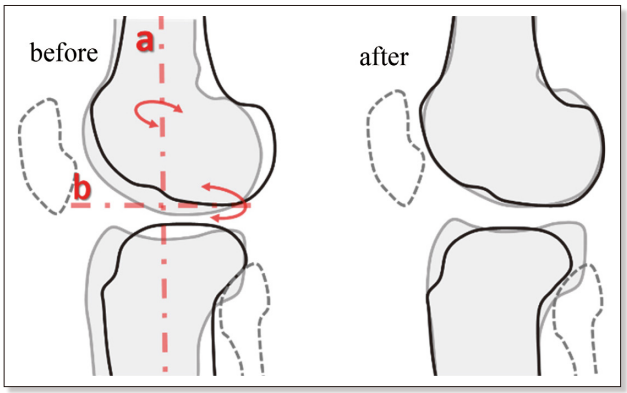

Fig. 4 Correction of rotation and abduction
(a) Rotation shaft (b) Abduction shaft

the optimal imaging angle as basic data for the positioning of standing lateral imaging as an imaging technique. Yasuda et al. [7] reported correction angles to propose auxiliary tools for lateral imaging of the knee joint in the supine

position. However, there are no reports on the correction angles or X-ray incidence angles for lateral alignment in standing imaging. Therefore, using clinical images for knee OA taken at our center, we measured the femoral rotation angle for rotation correction and the X-ray incidence angle for abduction correction when performing standing lateral imaging and clarified their angle distributions.

The subjects were 73 individuals (74 knees) diagnosed with knee OA who underwent knee joint X-ray CT, and 366 individuals (498 knees) diagnosed with knee OA who underwent standing frontal imaging. However, patients who had undergone total knee arthroplasty were excluded from the standing frontal imaging group.

Methods

1. Femoral rotation correction

The subjects for this measurement were 74 knees from patients diagnosed with knee OA at our center who had undergone knee joint CT (Table 1). The average age was 78.0 ± 6.5 years (14 male knees: 77.6 ± 6.7 years; 60 female knees: 78.1 ± 6.5 years).

From the target X-ray CT images, the femoral rotation angle for femoral rotation correction in the lateral limb position was determined. The reference frontal image (A) of the pseudo-X-ray images shown in Fig. 5 was generated using Ray Summation (hereafter, Ray Sum) images processed from X-ray CT images on a 3D workstation (hereafter, 3D-WS), such that the intercondylar notch (f) of the femur was symmetrical. The inward femoral rotation angle required to transition from the frontal image (A) to a lateral image (B), where the posterior edges of the medial and lateral condyles (p) were aligned, was then calculated by rotating the image on the 3D-WS. The obtained rotation angle was defined as the femoral rotation correction angle for actual standing lateral imaging. The X-ray CT scanners used were Aquilion ONE TSX-305A and Aquilion CXL64 (Canon Medical Systems, Tochigi, Japan), and the 3D-WS used was Ziostation2 (Ziosoft, Tokyo, Japan).

Table 1 Femoral rotation correction

	Male (n=10)	Female (n=64)	Total (n=74)
Age, mean±SD	77.6±6.7	78.1±6.5	78.0±6.5

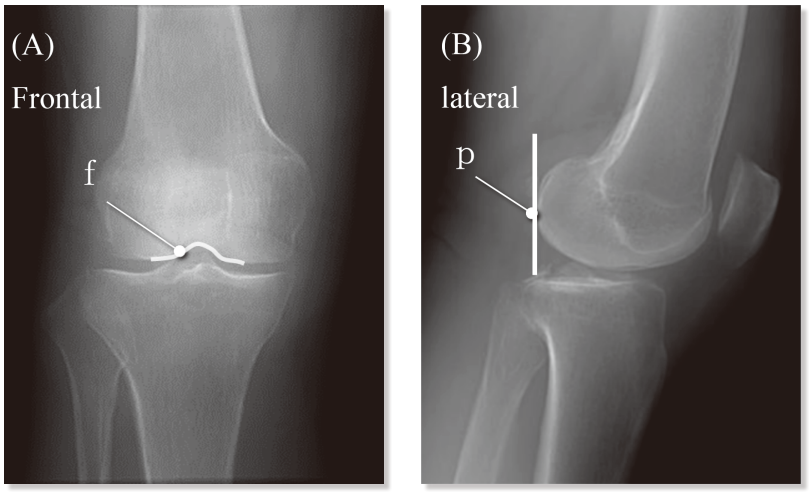

Fig. 5 Ray Sum images
(f) Intercondylar notch
(p) Posterior edges of the medial and lateral femoral condyles

Table 2 Abduction correction of the tibiofemoral joint

	Male (n=129)	Female (n=369)	Total (n=498)
Age, mean±SD	77.3±9.9	78.6±8.8	78.3±9.1

2. Abduction correction of the femorotibial joint

The subjects for this measurement consisted of 498 knees from patients diagnosed with knee OA at our center who had undergone standing frontal imaging (Table 2). The average age was 78.3 ± 9.1 years (129 male knees: 77.3 ± 9.9 years; 369 female knees: 78.6 ± 8.8 years). The X-ray systems used were RADspeed Safire (Shimadzu Corporation, Kyoto, Japan) and CALNEO U (Fujifilm Medical, Tokyo, Japan).

2-1. Measurement of the angle for tangential X-ray incidence to the tibial plane

As shown in Fig. 6, the angle formed by the floor (c) and the "tibial plane line" (the line connecting the midpoint of the superior edge of the lateral condyle [a] and the midpoint of the inferior edge of the medial condyle [b] on the tibial plane) was measured from the frontal image (C). The angle was defined as 0° when the tibial plane line was parallel to the floor. A positive angle was recorded when the lateral condyle was higher than the medial condyle, and a negative angle was recorded when the medial condyle was higher than the lateral condyle.

2-2. Measurement of the angle for tangential X-ray incidence to the inferior edges of the medial and lateral femoral condyles

As shown in Fig. 7, the angle formed by the floor (e) and the "inferior femoral condylar line" (the line connecting the two points [d] at the inferior edges of the medial and lateral femoral condyles) were measured from the frontal image (D) (Fig. 5). The angle was defined as 0° when the inferior femoral condylar line was parallel to the floor (e). A positive angle was recorded when the lateral condyle was higher than the medial condyle, and a negative angle was recorded when the medial condyle was higher than the lateral condyle.

3. Ethical considerations

This study was conducted with the approval of the Ethics and Conflict of Interest Committee of the National Center for Geriatrics and Gerontology (Approval No. 1789).

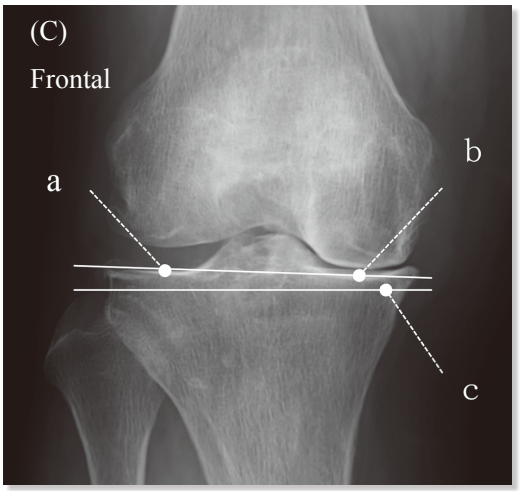

Fig. 6 Tibial plane line
(a) Midpoint of the upper end of the lateral condyle
(b) Midpoint of lower end of medial condyle
(c) Floor surface line

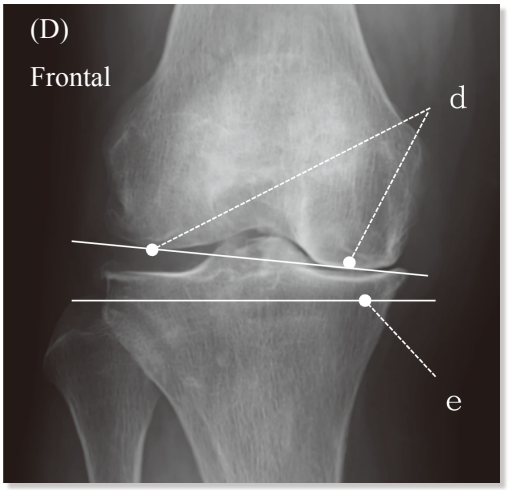

Fig. 7 Lower edge line of medial and lateral femoral condyles
(d) Midpoint of the lower end of both femoral condyles
(e) Floor surface line

Results

1. Femoral rotation correction

The inward femoral rotation angles required to obtain appropriate lateral images from the reference frontal images, as determined from Ray Sum images of knee joint X-ray CT, were 86.1 ± 2.1° for males, 84.6 ± 3.3° for females, and 84.6 ± 3.3° for the total population (Fig. 8). The inward femoral rotation angle obtained on the 3D-WS was defined as the femoral rotation correction angle.

2. Abduction correction of the femorotibial joint

2-1. Measurement of the angle for tangential X-ray incidence to the tibial plane

The angle formed by the tibial plane line and the floor, as determined from standing frontal X-ray images of the knee joint with both legs, was 4.6 ± 2.7° for males, 2.8 ± 3.2° for females, and 3.2 ± 3.2° for the total population (Fig. 9). The obtained angle between the tibial plane line and the floor was defined as the abduction correction angle of the femorotibial joint for tangential X-ray incidence to the tibial plane.

2-2. Measurement of the angle for tangential X-ray incidence to the inferior edges of the medial and lateral femoral condyles

The angle formed by the inferior femoral condylar line and the floor in the standing frontal X-ray images was 5.8 ± 3.0° for males, 5.3 ± 2.8° for females, and 5.4 ± 2.9° for the

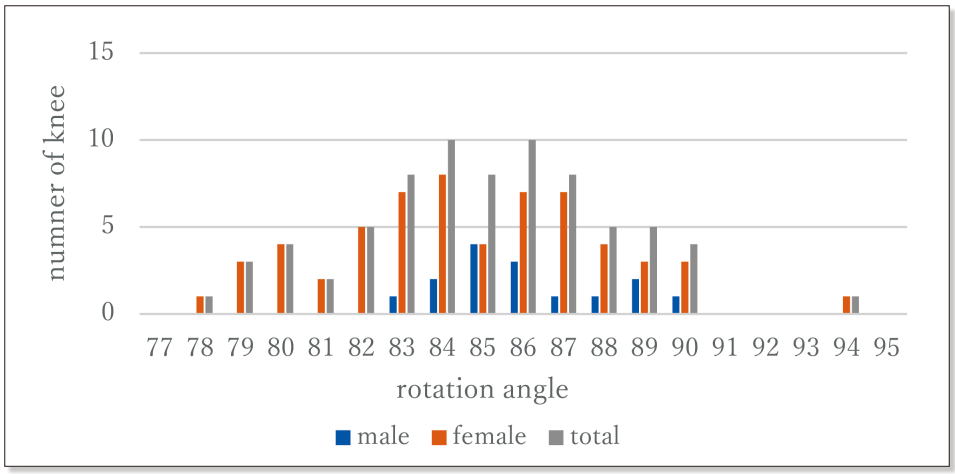

Fig. 8 Femoral rotation angle

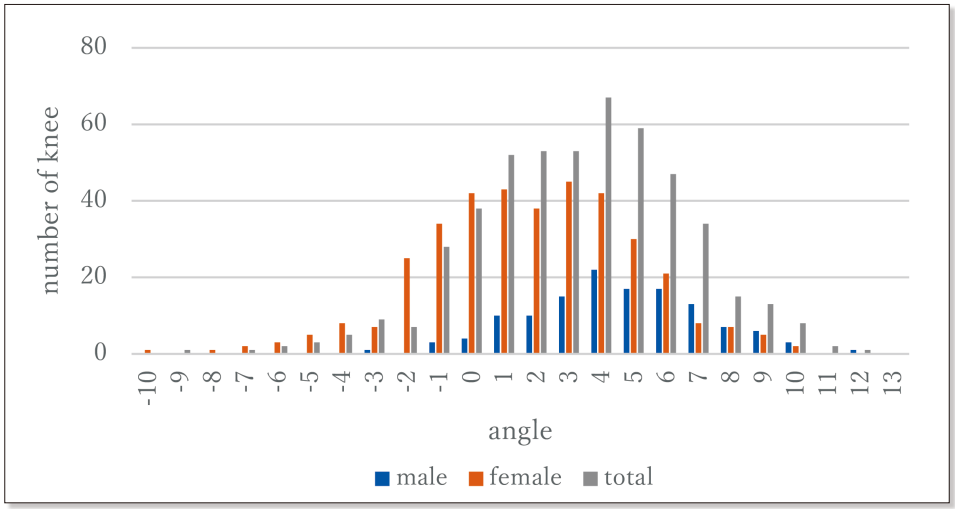

Fig. 9 Angle between supratibial joint line and floor

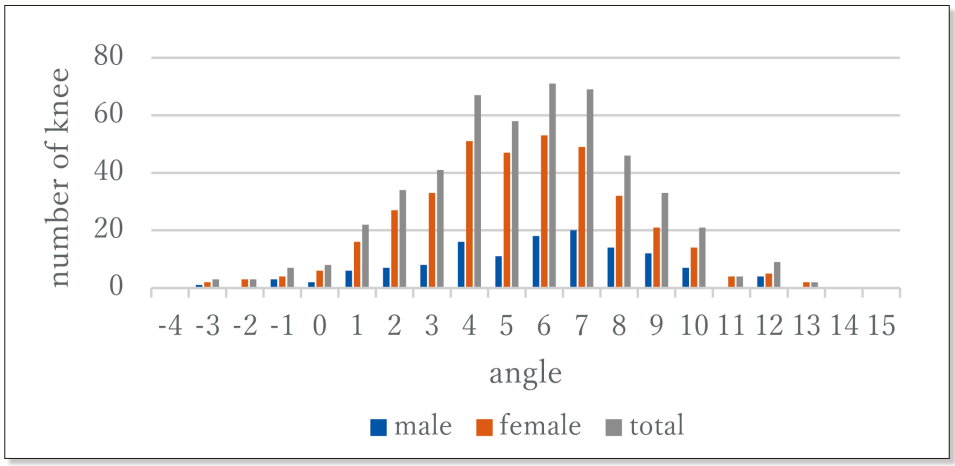

Fig. 10 Angle between the lower edge line of medial and lateral femoral condyles and floor

total population (Fig. 10). The obtained angle between the inferior femoral condylar line and the floor was defined as the abduction correction angle of the femorotibial joint for tangential X-ray incidence to the inferior edges of the medial and lateral femoral condyles.

Discussion

The knee joint is a weight-bearing joint, and because OA degeneration is accompanied by joint space narrowing and changes in lower limb alignment [8], lateral radiography of the knee joint is one of the imaging procedures that poses a challenge for radiological technologists (hereafter, technologists) [7, 9]. Lateral knee imaging can be performed in either single-leg or double-leg standing. At our center, we use the natural double-leg standing position shown in Figure 1 as a patient-friendly and safe option for elderly patients. To achieve accurate standing lateral images in this position, we measured and determined the angles for femoral rotation correction and abduction correction of the femorotibial joint.

Regarding femoral rotation correction for lateral positioning, the average inward femoral rotation angle required to obtain an appropriate lateral image from the reference frontal image was 84.6°. This indicates that the posterior edges of the medial and lateral femoral condyles align not at 90°, but at 84.6° from the reference frontal position. As shown in Fig. 6, the difference between males and females in the inward femoral rotation angle required for an appropriate lateral image was only 1.5°; therefore, we believe there is no need to adjust the imaging angle based on gender. We propose using the same angle of 84.6° as the rotation correction angle for both males and females.Regarding abduction correction for the X-ray incidence angle to the femorotibial joint, there was a difference of 2.1° between the total average of 3.2° for tangential incidence to the tibial plane line and the total average of 5.3° for tangential incidence to the inferior femoral condylar line. This difference is likely influenced by varus knee OA [10].

The angles for tangential X-ray incidence showed variability, with a total average of 3.2 ± 3.2° when aligned with the tibial plane line and 5.4 ± 2.9° when aligned with the inferior femoral condylar line. This variability is thought to include gender differences, individual differences, and differences depending on the degree of progression of knee OA.

The gender difference was only 1.8° on average for tangential incidence to the tibial plane line (males: 4.6 ± 2.7°, females: 2.8 ± 3.2°) and only 0.5° on average for tangential incidence to the inferior femoral condylar line (males: 5.8 ± 3.0°, females: 5.3 ± 2.8°). Chang-

ing the imaging angle for each gender would be complicated; therefore, it is considered more rational to use the same abduction correction angle for both males and females. Although referring to standing frontal images for each case is one possible method, doing so every time would also be cumbersome. Therefore, we propose an abduction correction angle of 3.2° in the cephalocaudal direction for tangential incidence to the tibial plane line, which likely has the highest success rate, and 5.4° in the cephalocaudal direction for tangential incidence to the inferior femoral condylar line. Since the choice between tangential incidence to the tibial plane line (Fig. 11A) and the inferior femoral condylar line (Fig. 11B) may vary by facility, we have proposed suitable abduction correction angles for both. Determining which incidence angle is superior remains a task for future study. In standing imaging, alignment abnormalities in knee OA are more pronounced due to weight-bearing compared to the supine position. In normal cases, as shown in Fig. 3, an image where both the tibial plane line and the inferior femoral condylar line are aligned is appropriate. However, in cases of knee OA, alignment abnormalities make it impossible to align both, necessitating a choice between them. Currently, as imaging methods for knee OA have not been fully established, we consider that the choice should be determined at each facility in consultation with physicians.

Regarding abduction correction, if the foot-to-foot distance differs between the frontal and lateral positions, the required correction angle will vary significantly. Therefore, it is necessary to maintain the same foot width position during imaging. To ensure reproducibility between the frontal and lateral positions, we recommend performing the imaging using a natural standing foot width.

Currently, standing imaging is recommended for the evaluation of knee OA [2]. However, in actual practice, many facilities still perform lateral imaging in the supine position. This is likely because a standardized method for standing lateral imaging has not yet been widely adopted, and many technologists do not provide it; as a result, objective evaluations have not been conducted. By clarifying the femoral rotation correction angle and the abduction correction angle of the femorotibial joint using knee joint X-ray CT images, we aimed to establish a standing lateral imaging method that contributes to the diagnosis of knee OA. We would be grateful if this study helps in the widespread adoption of standing lateral imaging.

The knee joint X-ray CT used to determine

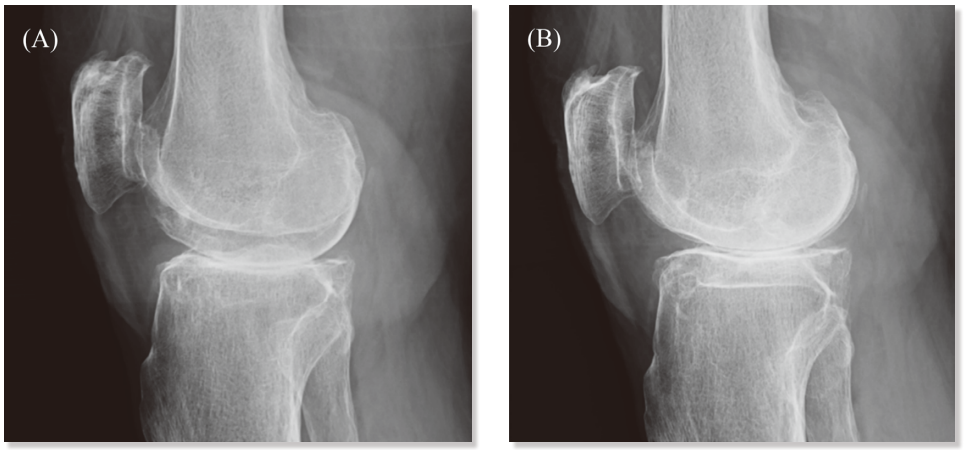

Fig. 11 Lateral image with abduction correction

(A) Tangential incidence to the tibial plane line
(B) Tangent to the lower border of the medial and lateral condyle of the femur incident

the femoral rotation correction angle was performed in the supine position, which differs from the natural standing position used for the actual standing lateral imaging. Although the shape of the femur determines the correction angle, the calculated femoral rotation correction angle may change in standing lateral imaging, as lower limb alignment varies depending on whether weight-bearing is applied.

Conclusion

For standing lateral radiography of patients with knee OA, it was suggested that a diagnostically valuable double-leg standing lateral X-ray image can be obtained by rotating the patient 84.6° inward from the standing frontal position and applying an X-ray incidence angle of 3.2° in the cephalocaudal direction when aligning with the tibial plane, or 5.4° when aligning with the inferior edges of the medial and lateral femoral condyles.

Conflicts of interest

The authors have no conflicts of interest to disclose in connection with this study.

Acknowledgments

We would like to express our sincere gratitude to Professor Eiji Ando of Jikei University of Health Care Sciences, Mr. Takayuki Harada of the National Hospital Organization Kanazawa Medical Center, and the staff of the Radiology Department at the National Center for Geriatrics and Gerontology for their significant cooperation in this study.

This study was previously presented at the 1st Japanese Congress of Radiological Technology in Medicine.

References

1) Cho E, et al.: Locomo Series 1: Knee Osteoarthritis. Journal of Nihon University Medical Association, 72(2), 77-80, 2013 (in Japanese).
2) Japanese Orthopaedic Association, ed.: Clinical Practice Guidelines for Management of Knee Osteoarthritis 2023. 37, Nankodo, 2023 (in Japanese).
3) Ando E: Illustrated Radiography of the Lower Extremities (Revised 2nd Edition). 35-46, 2023 (in Japanese).
4) Bone and Joint Radiography Subcommittee, Japan Association of Radiological Technologists: Report on the Results of the Questionnaire on Knee Joint Radiography. The journal of the Japanese Association of Radiological Technicians, 71(7), 92-101, 2024 (in Japanese).
5) Omori K, et al.: Lateral radiography of the knee with single-leg standing. Japanese Journal of Radiological Technology, 58(7), 940-947, 2002 (in Japanese).
6) Yoshii I, et al.: Rotational Deformity of the Leg in Varus Knee Osteoarthritis: Evaluation Using Single-Leg Standing Radiographs. Orthopedics & Traumatology, 37(3), 1000-1003, 1989 (in Japanese).
7) Yasuda Y, et al.: Proposal for an auxiliary tool designed to reduce retake rates for lateral radiography of the knee joint. Japanese Journal of Radiological Technology, 69(10), 1140-1145, 2013 (in Japanese).
8) Koga Y: Epidemiological Study on Knee Osteoarthrosis and the Background of Development of Three-Dimensional Alignment Assessment System. Physical Therapy Japan, 34(8), 340-344, 2007 (in Japanese).
9) Tanaka D, et al.: Support for retake of lateral knee radiographs by using content-based image retrieval. Bulletin of Butsuryo College of Osaka, 10(0), 39-43, 2022 (in Japanese).
10) Arizono T, et al.: Investigation of the Joint Surface Opening Angle in High Tibial Osteotomy. Orthopedics & Traumatology, 35(4), 1244-1246, 1987 (in Japanese).

Received May 12, 2024; accepted December 17, 2024

Evaluation of an Integrated MR Safety Information Management System Using a Hospital Logistics System and Investigation of Implanted Medical Device Cases

FUKUNAGA Masaaki, Ph.D.[1)]*, MIYAZAKI Takayuki[1)], OGASAHARA Takashi[1)], NOBUE Miyuki[1)], OSUMI Shinji[1)], FUJIOKA Hitoshi[2)], SEKIGUCHI Maiko[2)], TANAKA Haruna[2)]

1) Department of Radiological Technology, Kurashiki Central Hospital, Ohara HealthCare Foundation
2) Medie, Co., Ltd.

* E-mail: mf12895@kchnet.or.jp

Note: This paper is secondary publication, the first paper was published in the JART, vol. 72 no. 872: 12-20, 2025.

Key words: Implantable medical devices, Magnetic resonance safety information labeling, Safety management

【Abstract】
The purpose of this study was to evaluate the number of patients with implantable medical devices (IMDs) undergoing magnetic resonance imaging (MRI) and the number of IMDs per patient undergoing IMD implantation at our hospital.

The proportion of patients undergoing MRI increased from 1.5% in October 2016 to 4.9% in October 2020. There were 262 cases (72.6%) with 1 to 5 IMD implants per patient, and one case with 44 IMD implants. The percentage of MRI examination cases with IMDs increased, and there were cases with multiple IMDs implanted.

The integrated MR safety information management system will become increasingly useful because this system can check the IMD data and MR safety information simultaneously. An integrated MR safety information management system using the hospital logistics system was found to improve patient medical safety and MRI workflow.

Introduction

Magnetic resonance imaging (MRI) is a diagnostic imaging modality to examine all organs in the human body. Advantages of MRI include obtaining vascular information without contrast media, avoiding radiation exposure, and evaluating local pathologies by acquiring multiple images in a single examination. However, MRI uses a strong magnetic field of up to 3.0 Tesla, which increas the risk of adsorption accidents due to radio frequency irradiation, as well as the occurrence of magnetic effects and heat generation [1, 2].

There are various types of implantable medical devices (IMDs), which are classified as either active or passive. Active IMDs include neurostimulators, pacemakers, and cochlear implants. Passive IMDs include orthopedic implants, cerebral aneurysm clips, and metal coils. Since package inserts for new IMDs include magnetic resonance (MR) safety information labeling and MR safety information, physicians ordering MRIs and radiological technologists operating MR scanners must adjust the settings on the scanners accordingly.

ASTM international's F2503 [3] is the key standard that establishes the following three labels: MR Safe, MR Conditional, and MR Unsafe. In addition, the Food and Drug Administration [4] defined the Safety in MRI Not Evaluated label. MR safety information on IMD package inserts describes the MR-related conditions and the results of nonclinical testing, including the permitted static magnetic field strength [T], the maximum specific absorption rate (SAR) [W/kg], patient positioning, operating mode, the maximum gradient slew rate [T/m/s], the maxi-

mum spatial gradient field [T/m], scan duration [min], the maximum rate of change of the magnetic field [T/s], and the root mean square of B_{1+} (B_{1+RMS}) [μT]. Additional information is also described, such as temperature rise values, artifact evaluation, and precautions to take during an MRI examination.

Fujiwara et al. developed a system involving a patient interview before an MRI examination, with the aim of verifying the compatibility of any implanted metals or devices, and managing this information as an accurate medical history record [5]. However, constructing and maintaining the database is time-consuming and labor-intensive placing an additional burden on radiological technologists and administrative staff.

The contents of the package inserts can be viewed on the websites of the relevant device manufacturer or on the Pharmaceuticals and Medical Devices Agency (PMDA) website. Although the package insert of an IMD is the most fundamental document for ensuring its safe use; it is time-consuming to review in detail due to the large amount of information it contains. The MR compatibility search system for package inserts, developed by Fujiwara et al., enables users to easily verify the MR safety information labeling and MR safety information of IMDs prior to MRI examinations, as its database is specifically constructed based on the MR safety information labeling and MR safety information described in the package inserts [6, 7]. However, to use this system effectively, the commercial name of the IMD and the date it was implanted are essential; without this information, the system cannot be fully utilized. Traditionally, such information has been obtained from surgical records within the electronic medical record system. Because these records are typically written in free-text format, the commercial name of the IMD is not always documented accurately. We considered this to be a significant limitation when attempting to verify MR safety information. Therefore, we focused on the hospital logistics system to collect accurate IMD data. Also, an IMD information database could be constructed using the data stored in this system. Furthermore, by incorporating Medie codes, which uniquely identify IMDs at the product level, these data could be integrated with the newly developed product-level MR safety information database (Nextant; Medie, Co., Ltd., Tokyo, Japan). The integrated MR safety information management system—created by linking the IMD data from the hospital logistics system with the MR safety information database—enables users to confirm both the accurate information about IMDs implanted at our institution and the corresponding MR safety information labeling and MR safety information on a single screen simply by entering a patient identification (ID) number [8]. Because, this system's usefulness has not yet been evaluated, we sought to determine it by calculating the percentage of IMD carriers who undergo MRI and counting the number of IMDs each patient had.

The purpose of this study was to evaluate the utility of the integrated MR safety information management system by investigating the number and proportion of MR examinations performed in patients with IMDs, as well as the number of IMDs implanted per patient.

1 Methods

1-1 Integrated MR safety information management system

The integrated MR safety information management system developed by Fukunaga et al. was employed in this study [8]. The system was constructed on FileMaker Pro 16 (Claris International, Santa Clara, CA, USA). IMD data were extracted from the hospital logistics system, Web SPD III (Danknet, Tokyo, Japan), as consumption records in monthly comma-separated value (CSV) format, which were generated by the purchasing department from January 2012 onward. These consumption records in-

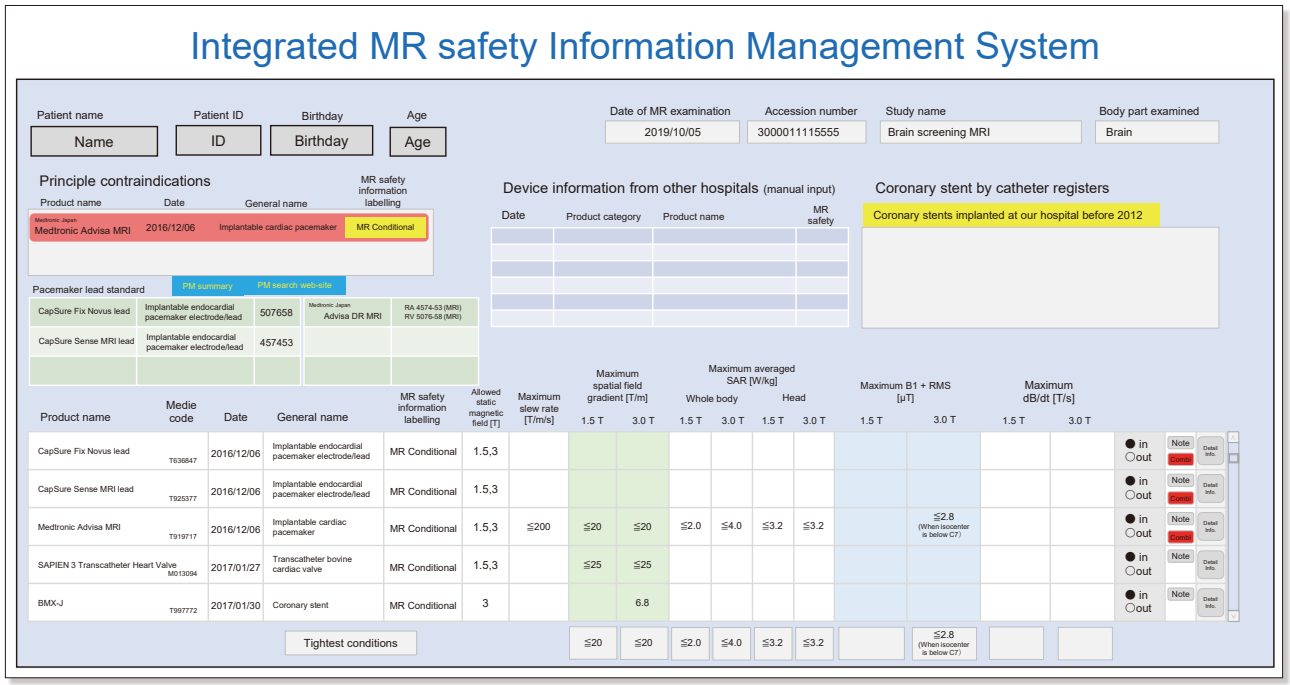

Fig. 1　Screen layout of the integrated MR safety information management system

This system enables a cross-search for information about a patient's surgical history and IMD package inserts on a single screen by entering the patient identification number. The MR safety information label can be checked at a glance, even when multiple IMDs are implanted.

MR, magnetic resonance; IMD, implantable medical device

cluded patient ID, patient name, commercial name of the device, material name, date of implantation, and product identification information (Medie code). The MR safety information database, created by Medie, Co., Ltd., was linked to the consumption records using the Medie code. The integrated MR safety information management system allows users to verify the commercial name of the IMD, implantation date, and MR safety information all on one screen by simply entering the patient ID (Fig. 1).

1-2　MR safety information database

The MR safety information database is based on the package inserts published on the PMDA website (https://www.pmda.go.jp) and is provided through, Nextant. As of December 2021, the MR safety information database used in this study included 117 Japan Medical Device Nomenclature (JMDN) code categories and 10,021 IMD products. The target IMDs were selected from devices for which MR safety verification is critical during MRI examinations and for which usage history is documented at our institution.

1-3　MR safety information labeling

MR safety information labeling was classified into the following six labels: MR Safe [3], MR Conditional [3], MR Unsafe [3], Safety in MRI Not Evaluated [4], MR Safety Unlabeled [9] or excluded IMD data.

MR Safe refers to items that pose no known hazards in any MR environment and are composed of nonconductive, nonmetallic, and nonmagnetic materials [3]. MR Conditional indicates items that pose no known hazards in a specified MR environment under specified conditions of use [3]; therefore, MRI examinations can be safely performed when conducted under the conditions described in the package insert. MR Unsafe refers to items that pose hazards in all MR environments; in principle, MRI examinations cannot be performed on patients with devices labeled as MR Unsafe [3]. Safety in MRI Not Evaluated denotes items for which

MRI safety has not been evaluated [4]. MR Safety Unlabeled refers to items that do not fall into the categories of MR Safe [3], MR Conditional [3], MR Unsafe [3], or Safety in MRI Not Evaluated [4], and for which no MR safety information is described in the package insert [9]. Excluded IMD Data refers to IMDs that were not included in the MR safety information database used in this study.

1-4 Subjects

The study included 11,834 MRI examinations performed in October each year from 2016 to 2020. Patient data were exported as CSV files from the radiology information management system (J-MAC System, Sapporo, Japan) based on the examination records of MRI procedures conducted during the study period and were subsequently imported into FileMaker. Because the number of eligible cases was large, only the October examinations were selected for analysis.

This study was approved by the institutional ethics review board (approval number: 3284).

1-5 Trends in the Number of MRI Examinations in Patients with IMDs

We counted the number of MRI examinations performed on patients with IMDs and those without IMDs in October each year from 2016 to 2020 at our institution. Only IMDs identifiable within the integrated MR safety information management system were included; IMDs implanted at other institutions were excluded from the analysis.

1-6 Number of IMDs Implanted per Patient Undergoing MRI

For patients undergoing MRI at our institution in October each year from 2016 to 2020, we counted the number of IMDs implanted per patient for those identified as having IMDs.

1-7 MR safety information labeling and Classification of IMDs

For patients with IMDs undergoing MRI in October each year from 2016 to 2020 at our institution, we investigated the MR safety information labeling and classifications of the IMDs. The MR safety information labeling was evaluated based on the 10,021 IMD products corresponding to 117 JMDN codes included in the database as of December 2021.

2 Results

2-1 Trends in the Number of MRI Examinations in Patients with IMDs

Table 1 shows the number of patients with and without IMDs among those who underwent MRI in October each year from 2016 to 2020. The number of MRI examinations performed in October was 2,297 in 2016, 2,430 in 2017, 2,616 in 2018, 2,330 in 2019, and 2,161 in 2020. The proportion of MRI examinations performed on patients with IMDs increased year by year: 1.5% in 2016, 2.6% in 2017, 2.9% in 2018, 3.4% in 2019, and 4.9% in 2020.

2-2 Number of IMDs Implanted per Patient

Figure 2 shows the relationship between the number of IMDs implanted per patient and the

Table 1 Number of MRI examinations and patients with and without IMDs in October each year

	October 2016	October 2017	October 2018	October 2019	October 2020
Total	2297	2430	2616	2330	2161
IMD (−)	2262	2366	2539	2250	2056
IMD (+)	35	64	77	80	105
Percentage of IMD (+)	1.5%	2.6%	2.9%	3.4%	4.9%

MRI, magnetic resonance imaging; IMD, implantable medical device

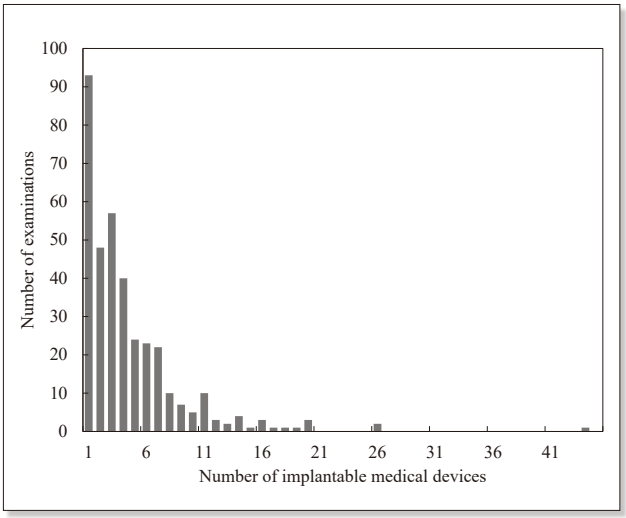

Fig. 2 Number of IMDs implanted in each patient
IMD, implantable medical device

corresponding number of MRI examinations. The largest group consisted of patients with one IMD, totaling 93 cases. The number of patients with 1 to 5 IMDs was 262, accounting for 72.6% of all IMD carriers, while 67 patients (18.6%) had 6 to 10 IMDs. There was one patient with 44 IMDs and two patients with 26 IMDs each.

2-3 MR safety information labeling and Classification of IMDs

Table 2 shows the number and proportion of IMDs for each MR safety information labeling category among IMD carriers who underwent MRI in October each year from 2016 to 2020. No IMDs were classified as MR Safe or MR Unsafe during the study period. The number of MR Conditional IMDs ranged from 24 to 197 (19.5% to 50.5% of all IMDs). The number of MR Safety Unlabeled IMDs ranged from 11 to 39 (3.6% to 13.8% of all IMDs). IMDs that were not included in the MR safety information database used in this study ranged from 82 to 314 (45.9% to 66.7% of all IMDs).

Table 3 shows the types of IMDs implanted in patients who underwent MRI in October each year. These patients had a total of 1,626 IMDs.

The most common IMDs were vascular embolization assist materials for the central circulatory system (JMDN code: 35449004, Class IV), totaling 437 devices. Spinal fixation devices (JMDN code: 37272003, Class III) were the second most common, with 193 devices. Next were coronary stents (JMDN code: 36035004, Class IV), with 167 devices; internal fixation screws (JMDN code: 16101003, Class III), with 148 devices; and internal fixation plates (JMDN code: 35241003, Class III), with 99 devices.

Table 2 MR safety information labeling in patients with IMDs undergoing MRI

	October 2016	October 2017	October 2018	October 2019	October 2020
MR Safe	0 (0.0%)	0 (0.0%)	0 (0.0%)	0 (0.0%)	0 (0.0%)
MR Conditional	24 (19.5%)	154 (50.5%)	139 (44.0%)	106 (31.8%)	197 (35.9%)
MR Unsafe	0 (0.0%)	0 (0.0%)	0 (0.0%)	0 (0.0%)	0 (0.0%)
Safety in MRI Not Evaluated	0 (0.0%)	0 (0.0%)	0 (0.0%)	3 (0.9%)	0 (0.0%)
MR Safety Unlabeled	17 (13.8%)	11 (3.6%)	27 (8.5%)	39 (11.7%)	38 (6.9%)
Excluded IMD data	82 (66.7%)	140 (45.9%)	150 (47.5%)	185 (55.6%)	314 (57.2%)
Total	123	305	316	333	549

MR, magnetic resonance; MRI, magnetic resonance imaging; IMD, implantable medical device

Table 3 Number of IMDs by JMDN code

(a) Cardiovascular medicine

No	JMDN	General Name	Classification	Number of IMDs
1	36035004	Coronary stent	Ⅳ	167
2	70489000	Coronary arterial stent graft	Ⅳ	1
3	61535004	Bioabsorbable coronary stent	Ⅳ	0
4	46919004	Drug-eluting stent for femoral artery	Ⅳ	1
5	44279000	Iliac stent	Ⅳ	14
6	70515000	Implantable biventricular pacing pulse generator without defibrillation feature	Ⅳ	0
7	12913000	Implantable cardiac pacemaker	Ⅳ	10
8	60789004	Implantable leadless cardiac pacemaker	Ⅳ	0
9	35223000	Implantable endocardial pacemaker electrode/lead	Ⅳ	20
10	36241000	Implantable defibrillator/pacemaker electrode/lead	Ⅳ	2
11	36102000	Implantable pacemaker adaptor	Ⅳ	0
12	35039000	Implantable epicardial pacemaker electrode/lead	Ⅳ	0
13	70514000	Implantable biventricular pacing pulse generator with defibrillation feature	Ⅳ	1
14	47932014	Heparin-coated stent-graft for central circulatory system	Ⅳ	1
15	60245114	Transcatheter porcine pericardial valve	Ⅳ	6
16	60245004	Transcatheter bovine cardiac valve	Ⅳ	3
17	70327000	Inferior vena cava filter	Ⅳ	6
18	35852000	Automatic implantable defibrillator	Ⅳ	0
19	37265000	Implantable automatic dual-chamber defibrillator	Ⅳ	0
20	36035003	Vascular stent	Ⅲ	2

(b) Cardiovascular surgery

No	JMDN	General Name	Classification	Number of IMDs
1	35591100	Bovine pericardium valve	Ⅳ	4
2	35644000	Annuloplasty ring	Ⅳ	6
3	35590010	Cardiac valve for mechanical artificial	Ⅳ	4
4	35591200	Porcine cardiac valve	Ⅳ	0
5	35591300	Porcine cardiac valve with vascular prosthesis	Ⅳ	0
6	70488000	Aortic stent graft	Ⅳ	14
7	35590020	Mechanical cardiac valve with vascular prosthesis	Ⅳ	0

(c) Neurosurgery and stroke

No	JMDN	General Name	Classification	Number of IMDs
1	35449004	Central circulatory intravascular embolization prosthesis	Ⅳ	437
2	16244000	Hydrocephalic shunt	Ⅳ	8
3	70302000	Hydrocephalic shunt auxiliary valve for prevention of excessive outflow of cerebrospinal fluid	Ⅳ	0
4	70421010	Intracranial aneurysm surgical clip	Ⅳ	42
5	70421020	Cerebral arteriovenus malformation surgical clip	Ⅳ	2
6	70491000	Cerebral artery stent	Ⅳ	0
7	45851000	Carotid artery stent	Ⅳ	4
8	70600000	Implantable stimulator for pain relief	Ⅳ	0
9	37307000	Tremor brain electrical stimulator	Ⅳ	0
10	36007000	Analgestic electrical stimulator	Ⅳ	0

(d) Orthopedic surgery

No	JMDN	General Name	Classification	Number of IMDs
1	32854004	Absorbable implantable fixation pin	Ⅳ	0
2	16101004	Absorbable implantable fixation screw	Ⅳ	24
3	33180000	Hip prosthesis bone cement restrictor	Ⅲ	0
4	35666000	Femoral component for hip prosthesis	Ⅲ	26
5	35661000	Hip prosthesis acetabular component	Ⅲ	27
6	33704000	Hemi hip prosthesis	Ⅲ	2
7	17751000	Artification bone matrix implant	Ⅲ	21
8	36315000	Total hip prosthesis	Ⅲ	3
9	33179000	Hip prosthesis acetabular support component	Ⅲ	0
10	33982003	Cement spacer	Ⅲ	0
11	16101003	Implantable fixation screw	Ⅲ	148
12	34031003	Cement bone plug	Ⅲ	0
13	35669000	Knee prosthesis tibial component	Ⅲ	0
14	35668000	Knee prosthesis femoral component	Ⅲ	0
15	35667000	Total knee prosthesis	Ⅲ	48
16	32833000	Unicondylar knee prosthesis	Ⅲ	0
17	35679000	Knee prosthesis patellar component	Ⅲ	0
18	70496000	Total elbow prosthesis	Ⅲ	0
19	33701000	Elbow prosthesis radial component	Ⅲ	0
20	35671003	Tendon spacer	Ⅲ	0
21	35642003	Implantable fixation system	Ⅲ	0
22	38153000	Implantable humerus intramedullary fixation nail	Ⅲ	9
23	33187000	Implantable femur intramedullary fixation nail	Ⅲ	20
24	34003000	Implantable fixation compression hip plate	Ⅲ	3
25	38152000	Implantable tibia intramedullary fixation nail	Ⅲ	6
26	32854003	Implantable fixation pin	Ⅲ	0
27	16103003	Implantable fixation staple	Ⅲ	0
28	35685003	Implantable fixation wire	Ⅲ	0
29	70504000	Implantable fixation cable	Ⅲ	3
30	36174003	Ligament fixation anchor	Ⅲ	4
31	35217000	Orthopaedic bone cement	Ⅲ	0
32	37272003	Spinal internal fixation system	Ⅲ	193
33	38161003	Spinal cage	Ⅲ	27
34	34170003	Artifical vertebral body	Ⅲ	1
35	35647003	Extrasomatic fixation system	Ⅲ	0
36	32835000	Shoulder prosthesis humeral component	Ⅲ	5
37	36259000	Shoulder prosthesis glenoid component	Ⅲ	0
38	35670000	Total shoulder prosthesis	Ⅲ	13
39	37845000	Digit prosthesis	Ⅲ	0
40	35241003	Implantable fixation plate	Ⅲ	99
41	35717003	Non-absorbable ligament prosthesis	Ⅲ	0
42	34602000	Plastic suture	Ⅲ	0
43	70426000	Implantable suture retention device	Ⅲ	0

(e) Urology, obstetrics and gynecology

No	JMDN	General Name	Classification	Number of IMDs
1	34926003	Long-term use ureteral tube stent	Ⅲ	2
2	36211000	Urethral stent	Ⅲ	0
3	34149002	Pelvic-organ-supporting pessary	Ⅱ	0

4	35237000	Reusable contraceptive pessary	Ⅱ	0
5	70261000	Body orifice obstruction balloon catheter	Ⅱ	0

(f) Respiratory medicine

No	JMDN	General Name	Classif cation	Number of IMDs
1	36029000	Tracheal stent	Ⅲ	0
2	17957000	Bronchial stent	Ⅲ	0

(g) Otolaryngology

No	JMDN	General Name	Classif cation	Number of IMDs
1	30084000	Middle ear implant hearing aid	Ⅲ	0
2	35643000	Auditory electrical stimulator	Ⅲ	0
3	34180000	Implantable bone-conduction hearing aid	Ⅲ	0

(h) Gastroenterology and hepatology

No	JMDN	General Name	Classif cation	Number of IMDs
1	36227000	Stent for esophageal	Ⅲ	0
2	70493000	Colorecutal stent	Ⅲ	3
3	70494000	Gastroduodenal stent	Ⅲ	0
4	17672000	Biliary stent	Ⅲ	10
5	36143000	Pancreatic stent	Ⅲ	0
6	35649000	Implantable ligating clip	Ⅲ	0

(i) Catheter, vascular prosthesis, and clip

No	JMDN	General Name	Classif cation	Number of IMDs
1	16615120	Peripheral insertion central venous catheterization kit	Ⅳ	0
2	16615110	Central venous catheterization kit	Ⅳ	0
3	36257100	Peripheral insertion central venous catheter	Ⅳ	0
4	10729100	Catheter for central venous	Ⅳ	0
5	10729400	Urokinase-coated central venous catheter	Ⅳ	0
6	35093204	Collagen-containing coated vascular prosthesis	Ⅳ	5
7	35093104	Gelatine-containing vascular prosthesis	Ⅳ	18
8	35093404	Heparin-coated vascular prosthesis	Ⅳ	0
9	35281004	Central circulatory vascular prosthesis	Ⅳ	9
10	34606010	Absorbable suture clip	Ⅳ	0
11	35281003	Non-central circulatory vascular prosthesis	Ⅲ	4
12	70487103	Heparin-coated temporary use indwelling vascular prosthesis	Ⅲ	0
13	35093103	Gelatine-containing non-central circulatory vascular prosthesis	Ⅲ	0
14	35093403	Vascular prosthesis with heparin for non-central circullatory system	Ⅲ	0
15	35640003	Implantable vascular clip	Ⅲ	0
16	35449003	Vascular embolization prosthesis	Ⅲ	0

(j) Others

No	JMDN	General Name	Classif cation	Number of IMDs
1	71027000	Capsule imaging and tracking device	Ⅱ	0
2	71030000	Implantable electrocardiographic data recorder	Ⅳ	2
3	70961000	Reusable extension fixator	Ⅰ	0
4	35797000	Orthopedic cerclage applier	Ⅰ	0
5	38819001	Single-use natural orifices non-active endotherapy device	Ⅰ	0

(k) Implantable medical device other than magnetic resonance safety information database

No	JMDN	General Name	Classif cation	Number of IMDs
1	70511000	Synthetic artificial dura mater	Ⅳ	27
2	70485100	Extracorporeal pacemaker electrode wire	Ⅳ	43
3	70164020	Single-use high-frequency current procedure endoscopic active instrument	Ⅱ	4
4	10696013	Long-term use biliary catheter	Ⅲ	6
5	70434000	Absorbable tissue reinforcement material	Ⅳ	7
6	35241004	Absorbable implantable fixation plate	Ⅳ	7
7	32390000	Reusable surgical drill bit	Ⅰ	2
8	35911204	Heparin-coated long-term use implantable infusion port	Ⅳ	7
9	35911104	Long-term use implantable infusion port	Ⅳ	3
10	70296004	Central circulatory microcatheter	Ⅳ	17
11	38827000	Single-use electrosurgical endoscopic snare	Ⅱ	1
12	45418004	Intracardiac prosthesis	Ⅳ	4
13	15033001	Defibrillation body surface electrode	Ⅰ	6
14	36182000	Artifitial pericardial prosthesis	Ⅳ	1
15	70964001	Reusable joint operating instrument	Ⅰ	1

IMD, implantable medical device; JMDN, Japanese medical device nomenclature

3 Discussion

In this study, we investigated the number and proportion of MRI examinations performed on patients with IMDs, as well as the number of IMDs implanted per patient. The integrated MR safety information management system allows verification of the IMDs implanted in each patient based on IMD data obtained from the hospital logistics system. By retrospectively examining the number of MRI examinations performed on IMD carriers, the number and types of IMDs, and their MR safety information labeling, we evaluated the usefulness of the integrated MR safety information management system for MRI examinations in patients with IMDs.

The number of MRI examinations performed in October decreased in 2020 compared with previous years (Table 1). This decrease may be

due to the COVID 19 pandemic. From 2016 to 2020, the proportion of MRI examinations performed on IMD carriers increased from 1.5% to 4.9%. This steady increase indicates that the usefulness of the integrated MR safety information management system will continue to grow.

Of the IMD carriers who underwent MRI, the largest group was patients with a single IMD, accounting for 93 patients. A total of 262 patients (72.6%) had 1 to 5 IMDs, whereas 67 patients (18.6%) had 6 to 10 IMDs (Fig. 2). There was one patient with 44 IMDs and two patients with 26 IMDs each. Figure 3 shows the difference between the conventional method for confirming MR safety information for IMDs and the workflow for using the integrated MR safety information management system. The conventional method required identifying the commercial name of each IMD, checking comments in the radiology information system, reviewing plain X ray or computed tomography images, examining surgical records in the electronic medical record, and accessing departmental systems used by each clinical specialty. Even when the commercial name could be identified, MR safety information then needed to be obtained either through online MR compatibility search systems [6, 7] or by manually checking the package inserts. When multiple IMDs were implanted or when devices were placed by multiple clinical departments, various verification steps had to be used, resulting in a substantial time and labor burden for staff responsible for MRI examinations. In contrast, the integrated MR safety information management system enables users to view the commercial names, implantation dates, and MR safety information of IMDs on a single screen, thereby markedly reducing the workload of MRI staff compared with the conventional method. This study demonstrated that MRI examinations are being performed on patients with multiple implanted devices. The integrated MR safety information management system is expected to facilitate efficient verification of MR safety information and allow MRI staff to determine appropriate SAR and $B_{1+\,RMS}$ settings directly on the MR console for patients with

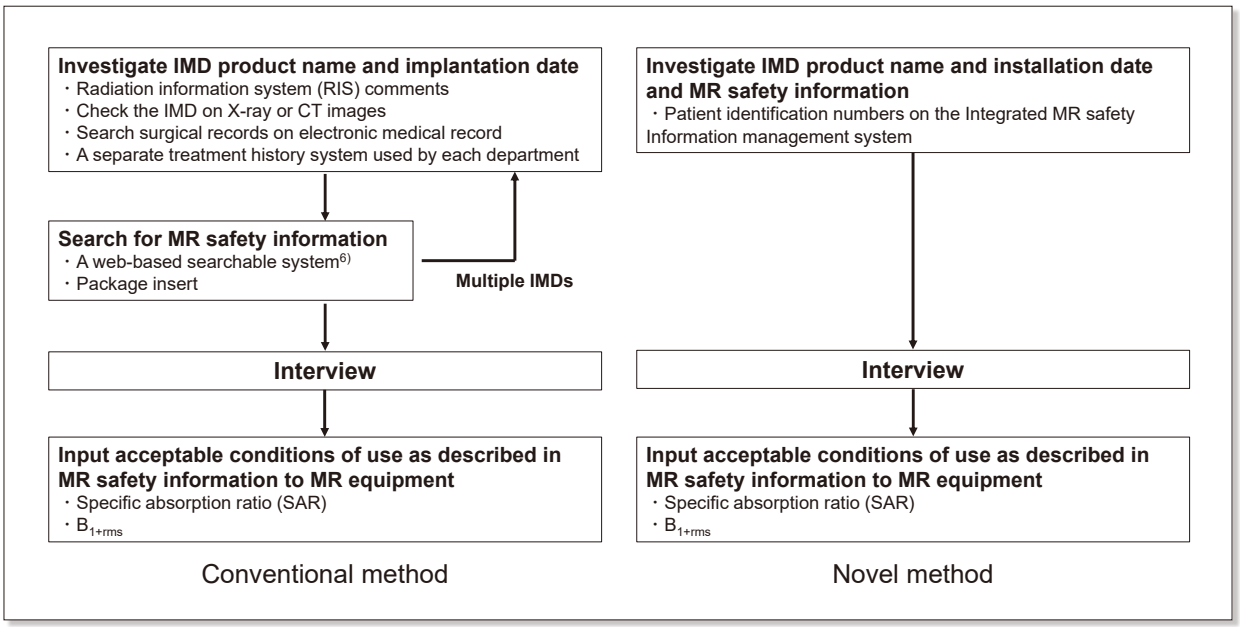

Fig. 3 Workflow of checking the product name, implantation date, and MR safety information before MRI

In conventional methods, it is necessary to search several systems used by different departments to obtain data. If multiple IMDs were present, the procedure was repeated for each IMD. The integrated MR safety information management system enables the cross-search for information about a patient's surgical history and IMD package inserts on a single screen by entering the patient identification number.

IMD, implantable medical device; MR, magnetic resonance; MRI, magnetic resonance imaging

multiple IMDs.

No IMDs were classified as MR Safe. According to Fukunaga et al., only 41 IMD products had been labeled as MR Safe by 2021 [8], indicateing that the number of IMDs originally designated as MR Safe was small. No IMDs were classified as MR Unsafe during the study period. Because MR Unsafe devices pose hazards in all MR environments, this finding demonstrates that our institution did not perform MRI examinations on patients with MR Unsafe devices.

However, in the orthopedic field, it has been reported that internal fixation pins (JMDN code: 32854003, Class III) and internal fixation wires (JMDN code: 35685003, Class III) have 16 and 4 products, respectively, labeled as MR Unsafe [8]. In response to notifications issued by the Ministry of Health, Labour and Welfare, MR safety information about orthopedic IMDs has improved sinidicantly [8-11]. Situations may arise in which MRI must be performed on patients with devices that were previously considered safe, but for which the MR safety information labeling has since been revised to MR Unsafe. In such circumstances, it is crucial for MRI facilities to carefully consider and establish appropriate management strategies.

The number of MR Conditional IMDs was 197 (35.9%) in October 2020. MR Conditional safety information includes specific parameters such as SAR or $B_{1+\,RMS}$ limits and the applicable magnetic field strength (1.5 T or 3.0 T). Because MRI must be conducted in accordance with these specified MR conditions, it is crucial to provide an environment in which MR safety information can be readily accessed.

Of the five most frequently implanted IMDs, vascular embolization assist materials for the central circulatory system are used in coil embolization procedures during endovascular treatment. These devices are used in many clinical departments, including neurovascular procedures for cerebral aneurysms and dural arteriovenous fistulas, bronchial and pulmonary artery fistulas and subclavian artery lesions in the thoracic region, as well as in abdominal and pelvic regions during stent-graft placement for aortic aneurysms. Consequently, the implantation sites vary widely. Moreover, multiple IMDs are often implanted during a single embolization procedure. Because patients with cerebral vascular lesions frequently undergo MRI, this category of IMDs was the most common in our study.

Although the current integrated MR safety information management system can identify the clinical department responsible for device implantation, it does not include details about the specific anatomical implantation site. Incorporating implantation site data into the integrated MR safety information management system will be an important sted toward improving the system in future.

Spinal fixation devices, internal fixation screws, and internal fixation plates are IMDs used in the orthopedic field. Many orthopedic IMDs that were previously classified as MR Safety Unlabeled have since been relabeled as MR Conditional or Safety in MRI Not Evaluated. Most orthopedic IMDs are made of non-magnetic materials, and therefore the risk associated with static magnetic field interactions is considered low. As a result, MRI examinations are less likely to be restricted for patients implanted with these devices.

For coronary stents, 98.8% of the products included in the MR safety information database used in this study are classified as MR Conditional [8], which likely contributes to the fact that MRI examinations for patients with coronary stents are rarely limited.

This study has several limitations. Because only IMDs implanted at our institution and recorded in the hospital logistics system were included, IMDs implanted at other institutions were excluded. Therefore, the total number of MRI examinations for IMD carriers may have been underestimated, as patients with IMDs implanted elsewhere were not captured. Additionally, temporary IMDs, such as epidural

anesthesia catheters and nasogastric or orogastric feeding tubes for short-term use, were excluded from the integrated MR safety information management system. Thus, they were not counted as IMD carriers in this study.

4 Conclusions

In this study, we investigated the number and proportion of MRI examinations performed on patients with IMDs, as well as the number of IMDs implanted per patient, using the integrated MR safety information management system. The proportion of MRI examinations performed on IMD carriers showed an increasing trend, reaching 4.9% in October 2020. The number of implanted IMDs also demonstrated an upward trend. These findings indicate that the integrated MR safety information management system—which enables simultaneous confirmation of IMD information and MR safety information on a single screen—is useful for improving patient safety and operational efficiency in MRI examinations.

Conflict of Interest

Hitoshi Fujioka, Maiko Sekiguchi and Haruna Tanaka are employees of Medie, Co., Ltd.

Funding

This study did not receive any specific grants from funding agencies in the public, commercial, or non-profit sectors.

Acknowledgements

We would like to express our sincere gratitude to the Purchasing Management Division, the MRI Examination Unit of the Department of Radiological Technology, and the Medical Innovation Promotion Office at Kurashiki Central Hospital for their invaluable cooperation in the development of the integrated MR safety information management system.

We thank Miho Kobayashi (Kurashiki Central Hospital) for extensive proofreading.

References

1) European Society of Radiology, et al.: Patient safety in medical imaging: A joint paper of the European Society of Radiology (ESR) and the European Federation of Radiographer Societies (EFRS). Radiography, 25(2), e26-e38, 2019.
2) Blankholm AD, et al.: Incident reporting and level of MR safety education: a Danish national study. Radiography, 26(2), 147-153, 2020.
3) ASTM International. ASTM F2503-20: standard practice for marking medical devices and other items for safety in the magnetic resonance environment. 2020.
4) Food and Drug Administration: Testing and labeling medical devices for safety in the magnetic resonance (MR) environment. Draft guidance for industry and Food and Drug Administration Staff. 2021. https://www.fda.gov/regulatory-information/search-fda-guidance-documents/testing-and-labeling-medical-devices-safety-magnetic-resonance-mr-environment. Accessed 25 April 2023.
5) Fujiwara Y, et al.: Development of an magnetic resonance imaging safety management system for metallic biomedical products using an magnetic resonance compatibility database and inquiry-based patient records. Nippon Hoshasen Gijutsu Gakkai Zasshi, 70, 1413-19, 2014. https://doi.org/10.6009/jjrt.2014_JSRT_70.12.1413
6) Fujiwara Y, et al.: A web-based searchable system to confirm magnetic resonance compatibility of implantable medical devices in Japan: a preliminary study. Radiol Phys Technol, 10, 340-8, 2017. https://doi.org/10.1007/s12194-017-0409-2
7) Fujiwara Y, et al.: Development of a searchable system to confirm MR imaging safety information for implantable medical devices. Magn Reson Med Sci, 18, 286-92, 2019. https://doi.org/10.2463/mrms.tn.2018-0100
8) Fukunaga, M, et al.: Survey on the Number and Percentage of MR Safety Labeling Changed for Implantable Medical Devices. Nihon Hoshasen Gijutsu Gakkai Zasshi, 80(2), 188-194, 2024.
9) Sekiguchi M. Recent Trends in the MR Safety Information Database for Medical Devices. Jpn J Magn Reson Med, 41(3), 54-60, 2021.
10) Ministry of Health, Labour and Welfare: Measures Regarding MR Safety of Implantable Medical Devices. 2019. https://www.pmda.go.jp/files/000230872.pdf (Accessed 27 January 2023).
11) Kuroda K, et al.: New insights into MR safety for implantable medical devices. Magnetic Resonance in Medical Sciences, 21, 110-31, 2022. https://doi.org/10.2463/mrms.rev.2021-0160

Received October 11, 2024; accepted February 13, 2025

Patient dose levels based on the nature and complexity of fluoroscopy-guided endoscopic procedures

MORI Hiroshige, Ph.D.[1)]*, BABA Masaru, M.D.[2)], HOSHINO Hirobumi[3)]

1) Department of Radiology, Japan Community Healthcare Organization Hokkaido Hospital
(Present address: Department of Radiology, Japan Community Healthcare Organization Sapporo Hokushin Hospital)
2) Center for Gastroenterology and Hepatology, Japan Community Healthcare Organization Hokkaido Hospital
3) Department of Radiology, Japan Community Healthcare Organization Sapporo Hokushin Hospital

* E-mail: mori-hiroshige@hokushin.jcho.go.jp

Note: This paper is secondary publication, the first paper was published in the JART, vol. 72 no. 873: 13-23, 2025.

Key words: endoscopic retrograde cholangiopancreatography (ERCP), diagnostic reference level (DRL), complexity indices, under-couch tube X-ray unit, size correction factor

【Abstract】
In the endoscopic retrograde cholangiopancreatography (ERCP) performed with a C-arm unite and under-tube position, body size-corrected patient doses were totaled according to the nature and complexity of the procedure. The entrance-surface air kerma rate at fluoroscopy was 4.81 mGy/m. In the endoscopic biliary drainage, endoscopic pancreatic drainage, endoscopic lithotripsy, endoscopic nasogallbladder drainage, and balloon assisted endoscope-guided ERCP, the air kerma was 31.7 mGy, 30.8 mGy, 49.2 mGy, 140.3 mGy, and 155.0 mGy, respectively. The ERCP doses varied up to about five times higher depending on the content. The ERCP doses in highly complex cases were about twice as high as those in normal cases. In the future, it is recommended to consider the complexity and nature of the ERCP procedure when setting the diagnostic reference level.

INTRODUCTION

In recent years, the several diagnostic reference levels (DRLs) for endoscopic retrograde cholangiopancreatography (ERCP) have been proposed in Japan[1-3)]. The Japan Network for Research and Information on Medical Exposure has proposed Japan DRLs 2020[1)], aligning with International Commission on Radiological Protection (ICRP) Publication 117[4)], by categorizing ERCP into diagnostic and therapeutic purposes. However, due to advances in other imaging technologies, diagnostic ERCP is now limited to procedures aimed at intraductal ultrasonography (IDUS) or obtaining pathological specimens[5)]. In addition, patient dose levels are expected to depend on the performed procedure[5)], because various procedures are performed in therapeutic ERCP[6-8)].

Furthermore, ICRP Publication 135 notes that patient anatomy and lesion characteristics bring complexity of procedures, leading to variability in patient doses even for the same procedure[9)]. Consequently, DRLs considering procedural complexity are beginning to be proposed[10-11)]. Radiation Exposure from Gastrointestinal Fluoroscopic Procedures (REX-GI) study categorizes DRLs by disease state and lesion locations[2-3, 12)]. However, it does not examine procedural complexity.

ICRP Publication 117 notes that fluoroscopic procedures using over-tube systems are not appropriate, yet they are widely used for ERCP procedures[4)]. However, to reduce radiation exposure, the use of under-tube or C-arm systems is recommended for ERCP[13)]. Japanese DRLs are mostly proposed based on data from over-tube systems or mixed over-tube and under-tube systems[1-3)]. If there were typical values[9)] based solely on data from under-tube systems, they could serve as guidelines for future optimization of radiation protection.

In this study, we evaluated patient radiation doses during ERCP procedures performed using the under-tube position with a C-arm device, categorizing doses by procedure type and complexity. We compared these doses to the DRLs in Japan (Japan DRLs 2020[1] and REX-GI study[2]), evaluating the patient dose levels of our institution. Based on these findings, we discuss the elements required for future ERCP DRLs.

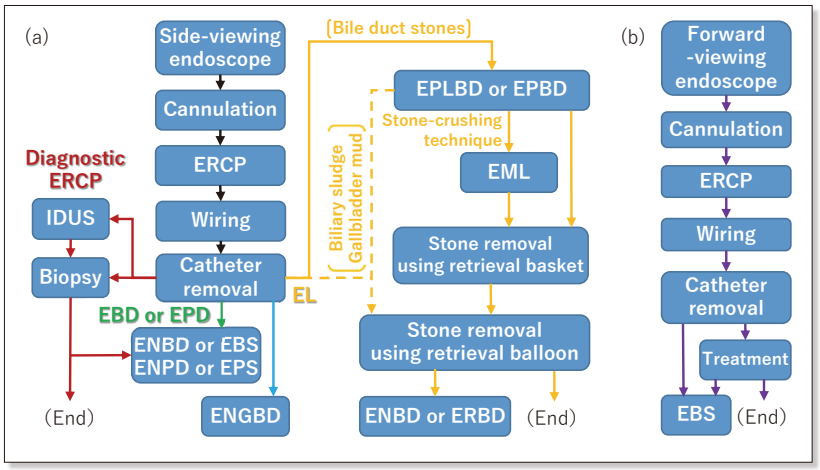

Fig. 1 Description of ERCP procedures covered in this study.

(a) Procedures using a side-viewing endoscope. After the removal of the contrast catheter, ERCP procedures are divided into diagnostic ERCP (red lines), endoscopic biliary or pancreatic drainage (EBD or EPD) (green lines), endoscopic nasogallbladder drainage (ENGBD) (blue line), and endoscopic lithotripsy (EL) (yellow lines).
(b) Procedures using a forward-viewing endoscope. Balloon assisted endoscope-guided ERCP (BAE-ERCP) is shown by purple lines.
IDUS, intraductal ultrasonography; ENBD, endoscopic nasobiliary drainage; EBS, endoscopic biliary stenting; ENPD, endoscopic nasopancreatic drainage; EPS, endoscopic pancreatic stenting; EPLBD, endoscopic papillary large balloon dilatation; EPBD, endoscopic papillary balloon dilatation; EML, endoscopic mechanical lithotripsy; ERBD, endoscopic retrograde biliary drainage.

1. Methods

1-1. Clinical subjects

1-1-1. Subjects

The study content and methodology were approved by our hospital's Ethics Committee (Research Approval No. 2023-29). Following approval, a retrospective cohort study was conducted on 766 patients (415 males, 351 females) who underwent ERCP at a single institution and using a single device between September 28, 2021, and March 31, 2024 (2.5 years). The age was 75.0 ± 13.8 years (range: 22 – 104 years), height was 159.1 ± 1.0 cm (range: 134.0 – 186.0 cm), and weight was 57.7 ± 12.3 kg (range: 27.6 – 101.0 kg) [mean ± standard deviation (maximum value – minimum value)].

1-1-2. Procedure details

The subject procedures were diagnostic ERCP with IDUS and biopsy, and therapeutic ERCP. Therapeutic ERCP was categorized by procedure type: endoscopic biliary drainage (EBD) performed for biliary strictures caused by tumors or cholangitis, endoscopic pancreatic drainage (EPD) for managing pancreatic juice flow obstruction, endoscopic nasogallbladder drainage (ENGBD)[14], which is selective cannulation of the gallbladder duct for acute cholecystitis, and endoscopic biliary stone removal[15] for common bile duct stones, which is referred to as endoscopic lithotripsy (EL) in this paper. Urgent ERCP[6,16], selected when there is a risk of septic shock due to cholelithiasis-induced pancreatitis or biliary obstruction, was grouped together with EBD in the statistics since it involves the same procedure content as EBD. Furthermore, balloon-assisted endoscope-guided ERCP (BAE-ERCP), selected for patients undergoing intestinal reconstruction via the Roux-en-Y procedure, uses a balloon-equipped forward-viewing endoscope (rather than the side-viewing endoscope used in ERCP). Therefore, it was excluded from the above procedure categories and counted separately. The procedures included in this study are shown in Fig. 1.

1-1-3. Procedure complexity

Cases where prolonged procedure time is anticipated, such as those with high cannula-

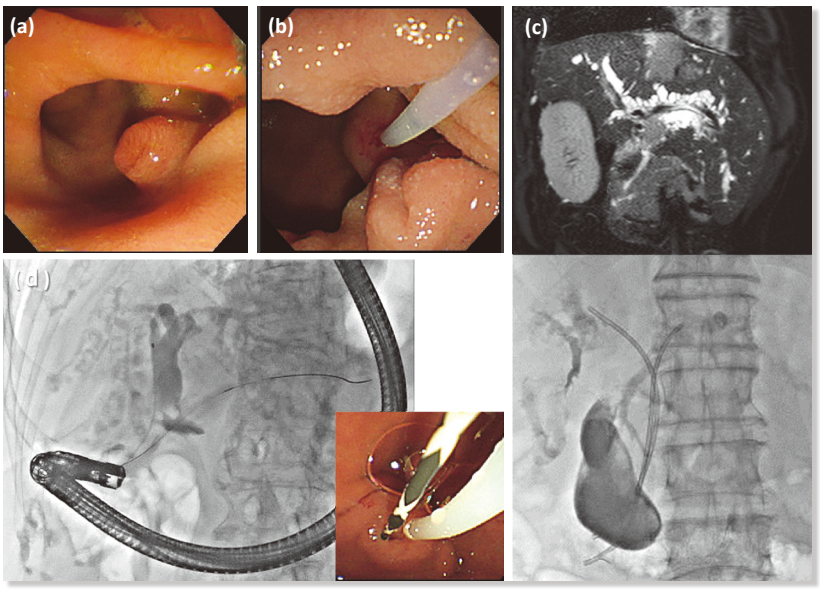

Fig. 2 Cases with complexity in ERCP.

(a) Juxtapapillary duodenal diverticula.
(b) Intra diverticular papilla.
(c) Proximal biliary obstruction. In the figure, the upper image is the T_2 weighted image of magnetic resonance imaging, and the lower image is the radiograph after endoscopic biliary stenting.
(d) Pancreatic guidewire cannulation. What is reflected in the X-ray image is a guidewire inserted into the pancreatic duct and a catheter inserted into the bile duct. In addition, the one in the bottom right is this endoscopic image.

tion difficulty, are also expected to require extended fluoroscopy time. Therefore, among cases undergoing EBD and EL, those where prolonged procedure time is anticipated or confirmed in the preceding studies[2, 17-19] were categorized as cases with high procedural complexity and analyzed separately from other cases to compare radiation exposure data with standard cases. Cases classified as having high procedural complexity were cases with juxtapapillary duodenal diverticula and intra diverticular papilla[17, 18], cases with biliary stricture at the hepatic hilum[2], and cases where the pancreatic duct guidewire method was selected to stabilize difficult-to-intubate papillae and straighten the distal bile duct[18, 19] (Fig. 2).

1-2. Equipment

The X-ray generator used in the under-tube position was a C-arm fluoroscopic diagnostic system (Alphenix INFX-8000C/TU, Canon Medical Systems Corporation, Otawara City, Tochigi Prefecture, Japan). This system consists of an X-ray high-voltage generator XTP-8100XG, an X-ray tube DSRX-T7735GFS with inherent filtration of 1.1 mmAl equivalent, an aperture BLA-900A with additional filtration of 1.8 mmAl equivalent, a catheter table CAT-880B with maximum 1.5 mmAl equivalent, and a 12 × 16 inches indirect flat panel detector (FPD) TFP-1216C/A1.

The cumulative air kerma for one ERCP procedure was measured using the area dosimeter included with the above device (calibration constant: 1.1025). The air kerma in phantom measurements was measured using a non-contact semiconductor detector[20] and quality assurance software (Piranha 557 and Ocean 2014 Professional, both from RTI Group, Mölndal, Sweden) (calibration constant: 1.0018). An acrylic plate of 40 cm × 40 cm × 1 cm was used as the phantom.

1-3. Imaging conditions

Imaging conditions were automatically set using the automatic exposure control (AEC) with the FPD positioned close to the subject. The specified ranges for tube voltage and tube current variations were 50 kV – 120 kV and 10 mA – 320 mA for fluoroscopy, and 50 kV – 125 kV and 20 mA – 1000 mA for cine. The field of view (FOV) primarily used was 12 × 12 inches (30 cm).

For fluoroscopy, the automatic brightness control (ABC) was applied, with brightness set to 0 and ABC tube voltage mode set to High. The fluoroscopy mode was set to Low, the pulse rate to 7.5 f/s, the line quality adjustment filter to 0.3 mm Cu, and the patient dose limit

to Normal. For cine, the exposure conditions were automatically set based on the most recent fluoroscopy conditions. The FPD incident dose was set to Normal, the pulse rate to 3.0 f/s, the maximum pulse width to 12.0 ms. The X-ray quality adjustment filter was automatically selected from four types (0.2 mm Cu, 0.3 mm Cu, 0.5 mm Cu, and 1.8 mm Al) according to the conditions.

In air kerma measurements using an acrylic phantom, the FOV was 12 × 12 inches (30 cm), the distance between the tube and FPD was 90 cm, the distance between the tube and dosimeter was 59 cm, and the height of the catheter table was 88 cm.

1-4. Dosimetry

1-4-1. Measurement of the air kerma of the devices

Using twenty acrylic phantoms stacked, the dose rate of entrance-surface air kerma ($K_{a,e}$) was measured at the patient entrance reference point (PERP). Under the above irradiation conditions, the acrylic plate was viewed under fluoroscopy. Once the tube voltage and tube current stabilized, the exposure was stopped to fix the fluoroscopy conditions. A non-contact X-ray dosimeter was then inserted beneath the phantom to measure the dose rate. The dose rate measured under these fluoroscopy conditions was compared to the reference fluoroscopy dose rate specified in Japan DRLs 2020[1].

The non-contact X-ray detector used for measuring $K_{a,e}$ cannot detect backscattered radiation due to its poor backward directional characteristics[20]. Therefore, the backscatter factor (BF) was calculated from the FOV (20 cm equivalent square) in PERP[21], and $K_{a,e}$ was calculated from the semiconductor detector measurement ($K'_{a,e}$) using the following equation.

$$K_{a,e} = K'_{a,e} \times BF \quad \cdots\cdots (1)$$

1-4-2. Measurement of clinical air kerma

The radiation dose structured report, which accumulates dose information per ERCP output from the X-ray equipment, was compiled. The collected dose information comprised the air kerma at the PERP ($K_{a,r}$) measured using an area dosimeter, the air kerma-area product (P_{KA}), and the fluoroscopy time. The $K_{a,r}$ and P_{KA} were aggregated separately for fluoroscopy and cine, then the total dose was calculated. The median and third quartile were then calculated for each of the collected dose parameters.

1-4-3. Size correction

In Japan DRLs 2020, only standard body type samples are used for ERCP DRLs (weight banding)[1]. However, it is often difficult to collect a sufficient number of samples matching the standard body type within a single facility[22]. On the other hand, the REX-GI study collected dose information without considering body size[2]. Analysis using all data regardless of weight reported no clinically significant differences compared to analysis using weight banding[9, 22]. Nevertheless, when sample sizes are small, dose differences due to body size may not be negligible[22]. Therefore, normalizing $K_{a,r}$ and P_{KA} is desirable to correct for body size differences between patients[9]. Considering these points, this study employed size correction[22, 23] that can eliminate the influence of AEC and ABC on dose and can utilize a small sample size efficiently. The $K_{a,r}$ and P_{KA} were normalized as follows.

The following relationship holds between P_{KA} and equivalent diameter (d_e)[23].

$$\ln P_{KA} = k \cdot d_e + c \quad \cdots\cdots (2)$$

$$d_e = 2\sqrt{\frac{W}{\pi H}} \quad \cdots\cdots (3)$$

The k (cm^{-1}) is the slope, the c is the intercept, the W (g) is body weight, and the H (cm) is height. P_{KA} (P'_{KA}) measured by ERCP is nor-

malized as follows using the subject's d_e (d'_e) calculated by equation (3), based on equation (2) [23].

$$\frac{P_{KA}}{P'_{KA}} = \frac{e^{(k \cdot d_{e,ref} + C)}}{e^{(k \cdot d'_e + C)}} \quad \cdots\cdots\cdots\cdots\cdots\cdots (4)$$

$$P_{KA} = e^{\{k \cdot (d_{e,ref} - d'_e)\}} \cdot P'_{KA} \quad \cdots\cdots\cdots\cdots (5)$$

The $d_{e,ref}$ (cm) is the d_e for the standard body type. In this study, the standard body type was defined using the average height and weight for men and women aged 20 and over reported in the 2019 National Health and Nutrition Examination Survey Report [24]. W was set to 60,500 g and H to 161.0 cm. Therefore, from equation (3), $d_{e,ref}$ is 21.87 cm. Next, $K_{a,r}$ ($K'_{a,r}$) measured by ERCP is similarly normalized [22].

$$K_{a,r} \cdot A = e^{\{k \cdot (d_{e,ref} - d'_e)\}} \cdot K'_{a,r} \cdot A \quad \cdots\cdots (6)$$

$$K_{a,r} = e^{\{k \cdot (d_{e,ref} - d'_e)\}} \cdot K'_{a,r} \quad \cdots\cdots\cdots\cdots\cdots (7)$$

The A (cm^2) represents the FOV area.

In this study, we measured the relationship between acrylic plate thickness and P_{KA} using 25 plates in increments of 5 plates, and calculated k for fluoroscopy and cine. Then, we substituted d'_e into equations (5) and (7), and performed size correction for P'_{KA} and $K'_{a,r}$.

1-5. Comparison with DRLs

This study investigates whether patient dose levels vary depending on the procedure performed, categorizing procedures by easily identifiable clinical terms (examination names). Furthermore, based on procedures identifiable in stored medical images (Fig. 2), cases with high complexity were categorized. However, Japan DRLs 2020 categorizes procedures by purpose [1], while the REX-GI study categorizes them by pathological condition [2], differing from the categorization method used in this study.

Therefore, when comparing with therapeutic ERCP categorized in Japan DRLs 2020, we grouped the five procedures which are EBD, EPD, EL, ENGBD, and BAE-ERCP into a single category.

Regarding to classification in REX-GI study, the ERCP, common bile duct stones, and pancreatic disease were compared with all ERCPs, EL, and EPD categorized in this study, respectively. DRL for malignant biliary obstruction (MBO) was not employed in this study's classification because it would exclude non-malignant biliary stenosis. However, DRL for MBO was compared with EBD, which is performed as a treatment for MBO. DRL for distal MBO (papillary side), which has the lowest DRL among MBO types, was compared with normal EBD. DRL for proximal MBO, which has biliary strictures at the hepatic hilum, was compared with complex EBD. Furthermore, because DRL for BAE in the REX-GI study is assumed to refer to general BAE for small bowel observation and biopsy, it was not used as a comparison target for BAE-ERCP in this study, which aims to treat strictures at anastomotic sites and in the biliary tract.

1-6. Statistical tests

Nonparametric tests were used to determine statistical significance [22], and statistical significance was determined when the probability (p) fell below the 1% significance level. Correlation between two groups was detected using Spearman's rank correlation coefficient test. Differences between two groups and among multiple groups were detected using the Mann-Whitney U test and Kruskal-Wallis test, respectively. Multiple comparisons were performed using the Steel-Dwass method. These statistical analyses were performed using EZR (Saitama Medical Center, Jichi Medical University, Saitama City, Saitama Prefecture, Japan) [25], which is a graphical user interface for R (The R Foundation for Statistical Computing, Vienna, Austria).

2. Results

2-1. Characteristics of the target information and devices

2-1-1. Number of cases for target procedures

Among the 766 ERCP cases retrospectively collected, the number of cases for the target procedures was 70 for diagnostic ERCP and 679 for therapeutic ERCP. Within therapeutic ERCP, there were 242 cases of EBD, 70 cases of EPD, 11 cases of ENGBD, 336 cases of EL, and 20 cases of BAE-ERCP. Among these, highly complex procedures were 105 cases of EBD and 122 cases of EL.

2-1-2. Patient dose for all ERCPs (uncorrected)

The relationship between d'_e from collected ERCP cases and $K'_{a,r}$ or P'_{KA}, which is the values before size collection, is shown in Fig. 3. Correlations of 0.333 and 0.375 was confirmed between d'_e and $K'_{a,r}$ and between d'_e and P'_{KA}, respectively (both $p < 0.01$).

2-1-3. k value

The relationship between P_{KA} and d_e used for size correction is shown in Fig. 4. The k values for fluoroscopy and cine conditions were 0.183 $cm^{-1}$and 0.213 cm^{-1}, respectively. The coefficient of determination for the regression line used to calculate k values was 0.997 for both conditions.

2-2. Air kerma of the device

The $K_{a,e}$ dose rate measured under fluoroscopy conditions was 4.81 ± 0.01 mGy/m (mean ± standard deviation) (80 kV; 33 mA; pulse width, 4.5 ms; half-value layer, 6.01 mmAl equivalent; BF, 1.5). This was approximately 70% lower than the reference fluoroscopy dose rate of 17 mGy/m[1)] proposed for interventional radiology in Japan DRLs 2020.

2-3. Clinical air kerma

The distribution of total ERCP doses collected is shown in Fig. 5. A very high correlation

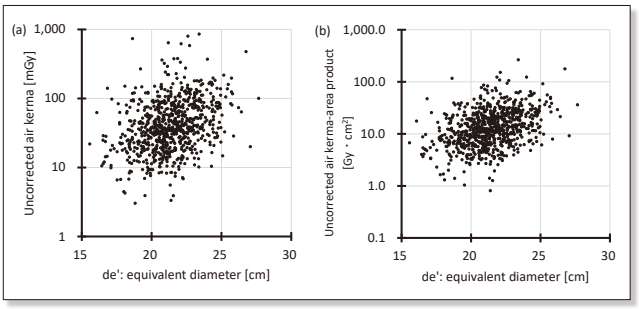

Fig. 3 Relationship between the equivalent diameters of subjects and the doses before size correction.

(a) Uncorrected air kerma at the patient entrance reference point.
(b) Uncorrected air kerma-area products.

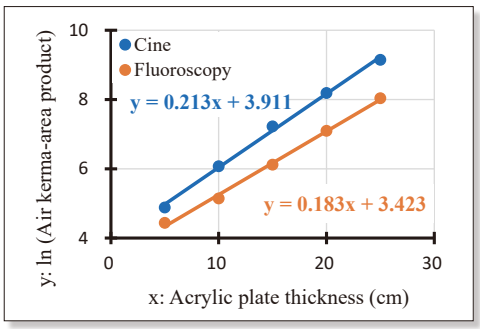

Fig. 4 Relationship between equivalent diameters (acrylic plates thickness) and air kerma-area products.

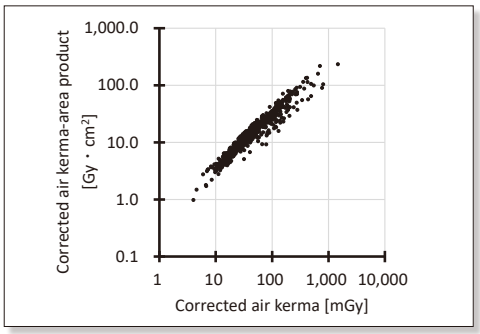

Fig. 5 Distribution of the patient doses after size correction in all ERCPs.

coefficient of 0.966 was confirmed between $K_{a,r}$ and P_{KA} ($p < 0.01$).

Comparison with DRL is shown in Table 1. For all ERCPs and therapeutic ERCPs, the doses were markedly lower than the DRL. For diagnostic ERCP, the median was below the DRL but slightly higher than the survey results that formed the basis for setting the Japan DRLs

Table 1　Comparison of the patient dose levels with the DRLs in Japan.

Items	Air kerma at the PERP: $K_{a,r}$ (mGy)					Air kerma-area product: P_{KA} (Gy・cm^2)					Fluoroscopy time: FT (min)				
	This study		DRL study		DRL	This study		DRL study		DRL	This study		DRL study		DRL
	Median	Q_3	Median	Q_3		Median	Q_3	Median	Q_3		Median	Q_3	Median	Q_3	
All ERCPs	45.8	80.6	69	145	145[*1]	15.1	24.7	16	32	32[*1]	7.7	11.5	11	20	20[*1]
Diagnostic ERCP	78.9	131.8	33.0	92.6	93[*2]	24.2	39.9	14.5	25.8	26[*2]	10.4	15.4	6.8	13.6	14[*2]
Therapeutic ERCP	43.5	73.8	99.5	167.1	170[*2]	14.6	23.0	17.9	35.6	36[*2]	7.1	10.9	11.2	16.8	17[*2]

The "*1" is REX-GI (radiation exposure from gastrointestinal fluoroscopic procedures) study, and the "*2" is Japan DRLs 2020. The "DRL study" is the study, which is the source of "*1" or "*2". PERP, patient entrance reference point; Q_3, 3rd quartile (75th percentile).

2020. The correlation between fluoroscopy time and total dose was 0.861 for $K_{a,r}$ and 0.871 for P_{KA}, confirming a high correlation for both (both $p < 0.01$).

The fluoroscopy and cine doses are shown in Fig. 6. Both $K_{a,r}$ and P_{KA} were significantly higher dose for fluoroscopy than that for cine (both $p < 0.01$), with the fluoroscopy dose accounting for approximately 70% of the total dose. The correlation between fluoroscopy dose and total dose was 0.979 for $K_{a,r}$ and 0.971 for P_{KA} (both $p < 0.01$).

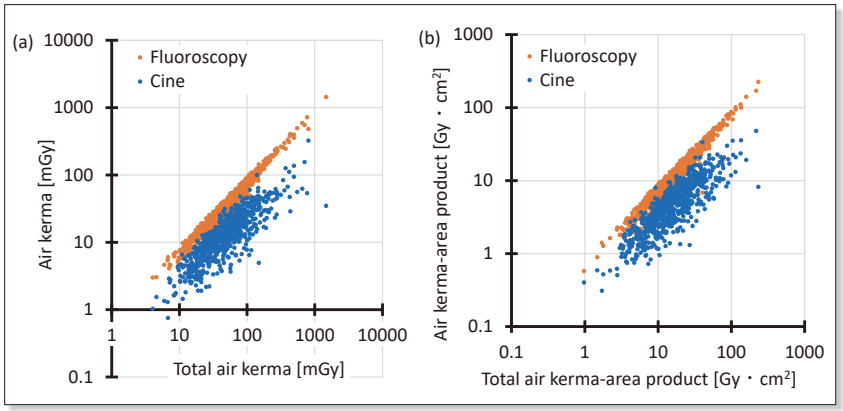

Fig. 6　Comparison between the fluoroscopy and cine doses in all ERCPs.
(a) Air kerma at the patient entrance reference point.
(b) Air kerma-area products.
All are the doses after size correction.

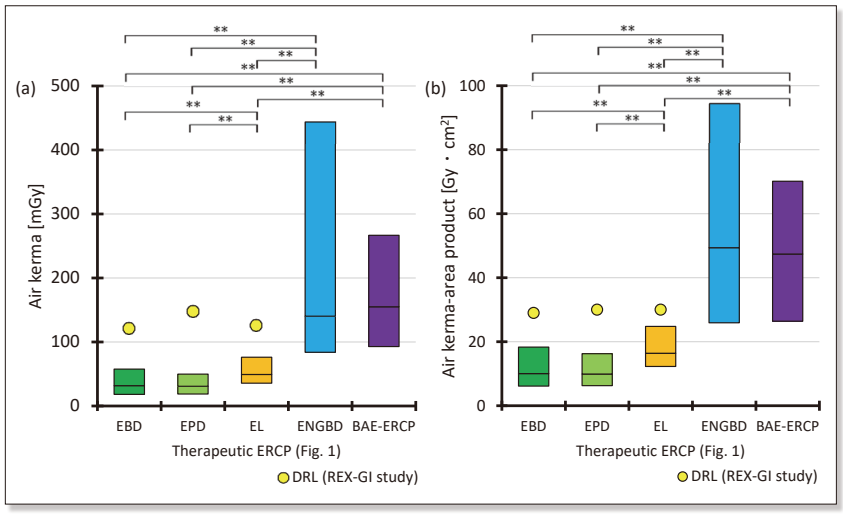

Fig. 7　Patient dose levels in each content of ERCP procedures.
(a) Air kerma at the patient entrance reference point.
(b) Air kerma-area products.
The central lines in the box indicate the median. The upper and lower bounds of the box are the 75th and 25th percentile values, respectively. The "＊＊" indicates $p < 0.01$, but there is no other significant difference. EL, endoscopic lithotripsy.

2-3-1. Classification by procedure content

Fig. 7 shows the doses for each procedure content in therapeutic ERCP. Significant differences were detected between procedure contents ($p < 0.01$). In multiple comparisons, significant differences were confirmed for all pairs except EBD and EPD, and ENGBD and BAE-ERCP (all $p < 0.01$). Specifically, ENGBD and BAE-ERCP were approximately 3 to 5 times higher than other procedures.

Table 2 shows the comparison with DRL. The doses for each procedure content were approximately half those of the REX-GI study.

Table 2 Comparison between the patient dose levels of therapeutic ERCP and the DRL of REX-GI study.

Items	Air kerma at the PERP: $K_{a,r}$ (mGy)					Air kerma-area product: P_{KA} (Gy・cm^2)					Fluoroscopy time: FT (min)				
	This study		REX-GI sutdy			This study		REX-GI sutdy			This study		REX-GI sutdy		
	Median	Q_3	Median	Q_3	DRL	Median	Q_3	Median	Q_3	DRL	Median	Q_3	Median	Q_3	DRL
EBD	31.7	57.6	59	121	121	10.0	18.3	14	29	29	5.1	9.0	10	18	18
EPD	30.8	49.8	74	148	148	9.9	16.2	15	30	30	5.7	8.8	11	20	20
EL	49.2	76.2	62	126	126	16.4	24.8	15	30	30	8.2	11.5	10	18	18
ENGBD	140.3	445.1	–	–	–	49.4	94.7	–	–	–	20.0	37.4	–	–	–
BAE-ERCP	155.0	266.7	–	–	–	47.4	70.2	–	–	–	19.8	32.4	–	–	–

The "EL" (endoscopic lithotripsy) is the endoscopic stone extraction of common bile duct stones and/or biliary sludge. In "EBD" (endoscopic biliary drainage), the DRL adopts the value for distal malignant biliary obstruction. EPD, endoscopic pancreatic drainage; ENGBD, endoscopic nasogallbladder drainage; BAE-ERCP, balloon assisted endoscope-guided ERCP; PERP, patient entrance reference point; REX-GI, radiation exposure from gastrointestinal fluoroscopic procedures; Q_3, 3rd quartile (75th percentile).

Procedures with higher doses also had longer fluoroscopy times.

The fluoroscopy and cine doses are shown in Fig. 8. Significant differences were detected between fluoroscopy and cine doses in all procedures (all $p < 0.01$). In multiple comparisons, significant differences were confirmed except between EBD and EPD, and between ENGBD and BAE-ERCP (all $p < 0.01$). However, for cine, no significant difference was observed between EL and ENGBD ($p > 0.05$), and dose difference based on procedure content was small compared to fluoroscopy. Furthermore, procedures with longer fluoroscopy times showed a higher proportion of fluoroscopy dose relative to cine dose.

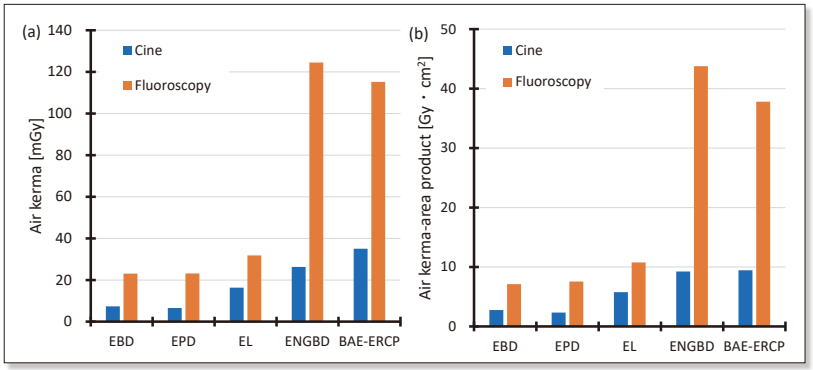

Fig. 8 Fluoroscopy and cine doses in the content of ERCP procedures.
(a) Air kerma at the patient entrance reference point.
(b) Air kerma-area products.
All doses are shown by the median. EL, endoscopic lithotripsy.

2-3-2. Classification by procedure complexity

Table 3 shows a comparison between normal and complex cases in therapeutic ERCP. Complex cases showed significantly higher doses

Table 3 Comparison of the patient dose levels between the normal and complex procedures in therapeutic ERCP.

Items	Complexity	Air kerma at the PERP: $K_{a,r}$ (mGy)					Air kerma-area product: P_{KA} (Gy・cm^2)					Fluoroscopy time: FT (min)				
		This study		REX-GI sutdy			This study		REX-GI sutdy			This study		REX-GI sutdy		
		Median	Q_3	Median	Q_3	DRL	Median	Q_3	Median	Q_3	DRL	Median	Q_3	Median	Q_3	DRL
EBD	(–)	22.4	46.7	59	121	121	8.1	13.3	14	29	29	4.0	7.3	10	18	18
	(+)	45.5	71.3	118	223	223	14.8	22.0	27	48	48	6.3	10.2	18	31	31
EL	(–)	44.7	69.4	62	126	126	15.3	22.6	15	30	30	7.8	10.6	10	18	18
	(+)	59.8	91.5	62	126	126	20.5	28.5	15	30	30	9.3	12.7	10	18	18

The cases shown in Figure 2, in which the prolongation of procedure time has been pointed out and confirmed in papers [2,17-19], are highly complex procedures, and the other cases are normal procedures. The patient dose levels of the normal and complex procedures are shown by "(–)" and "(+)", respectively. The "EL" (endoscopic lithotripsy) is the endoscopic stone extraction of common bile duct stones and/or biliary sludge. In "EBD" (endoscopic biliary drainage), the DRLs of "(–)" and "(+)" adopt the values for distal and proximal malignant biliary obstructions, respectively. PERP, patient entrance reference point; REX-GI, radiation exposure from gastrointestinal fluoroscopic procedures; Q_3, 3rd quartile (75th percentile).

than normal cases ($p < 0.01$), with increases up to approximately twofold. But doses of complex cases did not exceed the DRL.

The doses for complex cases are shown in Fig. 9. In all cases, the doses were approximately 1.5 to 2 times higher than that in normal cases, and cases where the pancreatic duct guidewire method was selected and cases meeting multiple complex items showed higher doses. However, the cases showing a significant difference compared to normal cases were only those where the pancreatic duct guidewire method was selected ($p < 0.01$). For EBD, a significant difference was also observed in cases with biliary stricture at the hepatic hilum ($p < 0.01$), where the dose was approximately twice as high as it in normal cases. Furthermore, cases with higher doses also had longer fluoroscopy times.

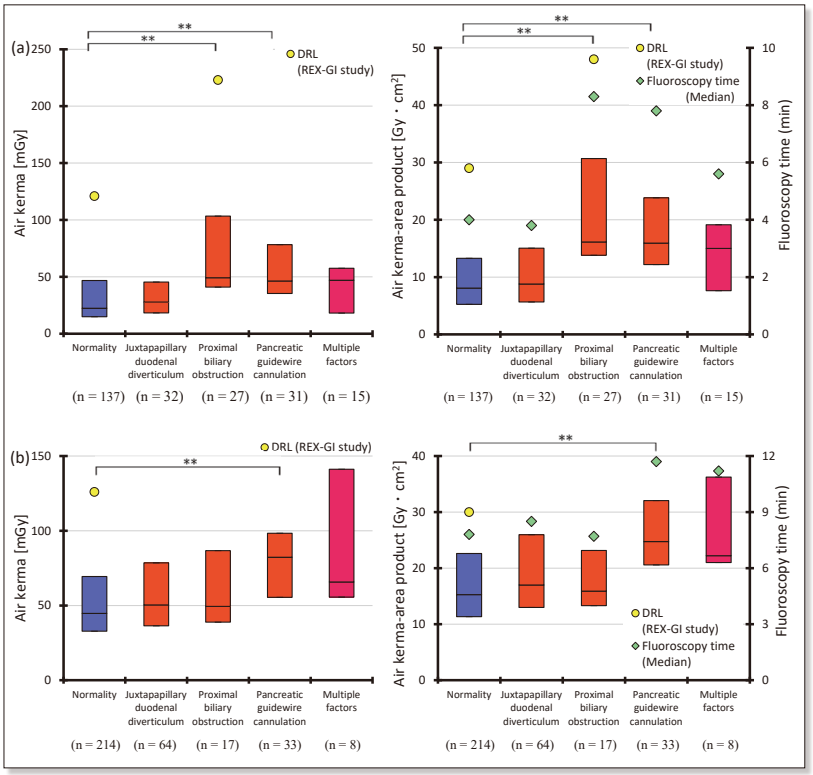

Fig. 9 Patient dose levels of the normal and complex procedures in therapeutic ERCP.

(a) Endoscopic biliary drainage.
(b) Endoscopic lithotripsy.
The central lines in the box indicate the median. The upper and lower bounds of the box are the 75th and 25th percentile values, respectively. The "＊＊" indicates p < 0.01, but there is no other significant difference. The "n" indicates the number of subjects.

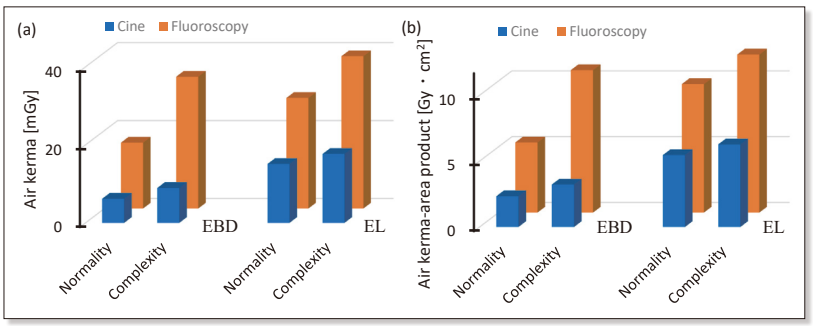

Fig. 10 Fluoroscopy and cine doses of the normal and complex procedures in the content of ERCP procedures.

(a) Air kerma at the patient entrance reference point.
(b) Air kerma-area products.
All doses are shown by the median. EBD, endoscopic biliary drainage; EL, endoscopic lithotripsy.

The fluoroscopy and cine doses are shown in Fig. 10. Differences due to procedural complexity were significantly detected between fluoroscopy and cine doses ($p < 0.01$). However, for cine, the dose difference attributable to procedural complexity was smaller than that for fluoroscopy.

3. Discussion

The ERCP DRLs in Japan DRLs 2020 were proposed based on approximately 1,300 cases[1]. This study collected 766 cases, which is sufficient for a single-institution sample size. Since the k-values in this study are high compared to previous studies[22,23], the equipment used causes significant variation in doses based on body size. Further-

more, body size is a bias that affects doses because there is a significant correlation between uncorrected dose and d'_e. However, the correlation is weak, suggesting that factors other than body size also influence doses. Comparing $K_{a,r}$ and P_{KA}, a very strong positive correlation was revealed. Therefore, the impact of FOV differences between cases on P_{KA} was considered small. P_{KA} is adopted in DRL to manage FOV size[4, 9]. Considering that P_{KA} was also lower than DRL to a similar degree compared to $K_{a,r}$, the FOV size in this study is considered to have been appropriately managed.

The total radiation dose for all ERCPs, therapeutic ERCPs, and individual procedural contents was significantly lower than each DRL. Opinions that C-arm devices and the under-tube position contribute to reducing patient exposure have existed previously[13, 26, 27]. While the dose-reducing effect of the under-tube position cannot be denied in this study, another major factor is the low fluoroscopy dose. It has been pointed out that fluoroscopy accounts for 70%–90% of the total dose in ERCP[28]. In this study, fluoroscopy also accounted for 70% of the total dose, showing a very strong correlation with the total dose. Furthermore, regarding the differences in total dose between factors of procedure content or complexity, it was suggested that these differences were primarily due to variations in fluoroscopy dose rather than cine dose. Moreover, the fluoroscopy dose rate in this study was 2/7 of the Japan DRLs 2020. This is attributed to the fact that the fluoroscopy mode was low[29] and the pulse rate was set to a lower value compared to the REX-GI study. Considering these points, it is thought that the low fluoroscopy dose is lowering the total dose in this study, and it can be said that suppressing the fluoroscopy dose has a significant effect on reducing the total dose of ERCP.

In this study, the radiation dose for diagnostic ERCP was relatively higher than that for therapeutic ERCP. This is considered to be due to the fact that diagnostic ERCP in this study included procedures such as IDUS and specimen collection (Fig. 1) in addition to EBD and EPD procedures which account for half of therapeutic ERCP, resulting in the addition of doses associated with fluoroscopy of these procedures. Conversely, Japan DRLs 2020 sets the DRL for diagnostic ERCP lower than that for therapeutic ERCP. However, since the details of the included procedures are not specified, it is impossible to examine why the value is lower. When publishing DRLs, we hope the breakdown of the collected procedures will be disclosed. For therapeutic ERCP, significant differences were observed based on procedure content, with a maximum difference of approximately five folds. Since EBD and EPD involve highly similar procedures, no difference in radiation dose was observed. Moving forward, it is necessary to present DRLs for ERCP based on disease conditions and procedure types, as demonstrated in the REX-GI study. We propose presenting DRLs separately for endoscopic biliary and pancreatic drainage procedures and endoscopic biliary stone removal procedures. Furthermore, it was suggested that procedures requiring long time for cannulation, such as ENGBD and BAE-ERCP[30, 31] should also have their DRLs presented separately from general ERCP.

The relationship between procedural complexity and DRL has been confirmed, showing that radiation dose varies according to the degree of complexity[10, 11]. In this study as well, cases with high complexity showed a significantly higher dose, approximately twice that of normal cases. Furthermore, significant dose differences were observed even among cases with high complexity. Reports indicate that cases involving duodenal papillary diverticulum and intra-diverticular papilla do not affect procedure time when performed by experienced ERCP operators[17]. Therefore, we consider the high proficiency of the operators in this study to be the reason why no significant

difference was observed compared to routine cases. Cases involving biliary strictures at the hepatic hilum showed markedly higher doses, particularly in cases of hepatic hilum MBO or primary sclerosing cholangitis[2, 32], leading to a significant difference compared to normal cases in EBD. Cases with multiple complexities, considered the most complex, had high doses but no significant difference from normal cases. This was due to the small sample size of cases with multiple complexities, resulting in insufficient statistical power. Cases where the pancreatic duct guidewire technique was selected were those where bile duct cannulation was difficult[20], resulting in longer procedure times than usual. This also extended fluoroscopy time, leading to increased total radiation exposure. Regarding DRL classification, similar to cases of hepatic portal MBO in the REX-GI study, we propose establishing a separate DRL category for cases using the pancreatic duct guidewire method. Moving forward, it is necessary to consider a method for aggregating ERCP radiation doses[30] using complexity indices based on endoscopic procedure difficulty classifications[31, 32].

In procedures requiring long time for cannulation, such as ENGBD and BAE-ERCP[30, 31], fluoroscopy time was prolonged, and the total radiation dose was higher compared to other procedures[32]. Even in highly complex cases, procedures requiring extended time, such as those using the pancreatic duct guidewire method, showed longer fluoroscopy time and higher total radiation dose compared to other cases. Furthermore, these procedures and cases also had a higher proportion of radiation exposure during fluoroscopy. This suggests a pattern where extended procedure time leads to longer fluoroscopy time, and the higher proportion of fluoroscopy results in increased total radiation dose. The high correlation between fluoroscopy time and total dose further supports this phenomenon. Therefore, reducing fluoroscopy time is also identified as a factor contributing to lower ERCP radiation doses. In this study, fluoroscopy dose and dose rate were low, and fluoroscopy time was also significantly lower than in various DRLs. It can be said that operators themselves rarely pressed the fluoroscopy pedal during the procedure. At our institution, we have long sought to build a safety culture through dialogue with stakeholders, including operators[33-35]. We believe this effort contributed to understanding the importance of low dose and dose rate during fluoroscopy, led to shorter fluoroscopy times, and ultimately helped reduce the output fluoroscopy dose.

In recent years, the lowering of the lens equivalent dose limit[36] has brought lens exposure into focus[37]. However, fundamentally reducing the output dose is crucial[38] and effective[39], and efforts to lower the total dose compared to DRL, etc.[8] should not be neglected. This approach reduces not only patient exposure but also operator exposure. Efforts should not be limited to superficial measures like lens protection alone; fundamental consideration of the output dose must not be neglected. This study, based on a substantial data set, presented dose guidelines for ERCP procedures using C-arms and under-tube systems, categorized by procedure content and complexity. We hope that facilities actively pursuing optimization of protection and exposure reduction will utilize this data as a target for reduction goals in their future efforts.

4. Conclusion

This study compiled dose information for ERCP procedures performed under C-arm, categorized by procedure content and complexity, and compared it with two Japanese DRLs. Excluding diagnostic ERCP, the doses were significantly lower than those reported in the Japan DRLs 2020 and the REX-GI study DRL. This indicates that while the dose reduction effect of the under-tube cannot be denied, the

low fluoroscopy dose rate of 4.81 mGy/m and the short fluoroscopy time contributed significantly.

The DRL for diagnostic ERCP may not correspond to current diagnostic ERCP procedures, which often include additional techniques like IDUS or specimen collection, as the specific procedure content is not disclosed. Furthermore, in therapeutic ERCP, significant differences of up to fivefold were observed depending on the procedure content, such as endoscopic biliary/pancreatic duct drainage, endoscopic biliary stone removal, and procedures requiring long time for cannulation. Therefore, it is necessary to present DRLs categorized by procedure content in the future.

Cases where the pancreatic duct guidewire technique was selected or those with biliary strictures at the hepatic hilum exhibit approximately double the radiation dose compared to normal cases. For such highly complex procedures, establishing a separate DRL distinct from the general DRL is recommended.

When comparing DRLs at a facility, body size is one factor that can introduce bias affecting dose, so consideration should be given to utilizing size correction.

Presenting Conference

Part of this research was presented at the 9th Annual Meeting of Japan Community Healthcare Society.

Conflict of Interest

The first author and all co-authors have no conflicts of interest to disclose.

References

1) Japan Network for Research and Information on Medical Exposure (J-RIME): National Diagnostic Reference Levels in Japan (2020).12, 2020. https://j-rime.qst.go.jp/report/DRL2020_Engver.pdf (Accessed 2 February 2026)
2) Shiro Hayashi, et al.: Diagnostic Reference Levels for Fluoroscopy-guided Gastrointestinal Procedures in Japan from the REX-GI Study: A Nationwide Multicentre Prospective Observational Study. Lancet Reg Health West Pac, 20(100376), 1-8, 2022.
3) Tsutomu Nishida, et al.: Multicentre prospective observational study protocol for radiation exposure from gastrointestinal fluoroscopic procedures (REX-GI study). BMJ Open, 10(2), 1-8, 2020.
4) International Commission on Radiological Protection.: Radiological protection in fluoroscopically guided procedures outside the imaging department. ICRP publication 117, Ann ICRP, 40(6), 65-70, 2010.
5) Koshi Sakiyama, et al.: Examination of Optimization of Exposure Dose by IVR Procedure Based on DRLs 2020. Japanese Journal of Radiological Technology, 79(2), 160-165, 2023.
6) Takao Itoi, et al.: Training for ERCP-related procedures. Tando, 20(5), 587-596, 2006.
7) Masafumi Mizuide, et al.: Present situation of emergent ERCP in our hospital and Analysis of the five items to diagnose medium acute cholangitis. Progress of Digestive Endoscopy, 73(2), 97-102, 2008.
8) Yoshinori Igarashi, et al.: Endoscopic lithotomy for the bile duct stones. Tando, 24(1), 30-34, 2010.
9) International Commission on Radiological Protection.: Diagnostic Reference Levels in Medical Imaging. ICRP publication 135, Ann ICRP, 46(1), 71-75, 2017.
10) R Ruiz-Cruces, et al.: Diagnostic reference levels and complexity indices in interventional radiology: a national programme. Eur Radiol, 26(12), 4268-4276, 2016.
11) Marialena Vossou, et al.: Diagnostic reference levels and complexity indices in interventional radiology. Radiat Prot Dosimetry, 199(3), 254-261, 2023.
12) Shiro Hayashi, et al.: Radiation exposure dose of fluoroscopy-guided gastrointestinal procedures: A single-center retrospective study. Endosc Int Open, 8(12), E1872-E1877, 2020.
13) N Buls, et al.: Patient and staff exposure during endoscopic retrograde cholangiopancreatography. Br J Radiol, 75(893), 435-443, 2002.
14) Sugimoto Maki, et al.: Benefit of Endoscopic Naso-Gallbladder Drainage (ENGBD) and Endoscopic Gallbladder Stenting (EGS) for Acute Cholecystitis. Journal of abdominal emergency medicine, 29(3), 487-491, 2009.
15) Earl Williams, et al.: Updated guideline on the management of common bile duct stones (CBDS). Gut, 66(5), 765-782, 2017.
16) Nicolien J Schepers, et al.: Urgent endoscopic retrograde cholangiopancreatography with sphincterotomy versus conservative treatment in predicted severe acute gallstone pancreatitis (APEC): a multicentre randomised controlled trial. Lancet, 396(10245), 167-176, 2020.
17) Tomoyuki Iwata, et al.: Relationship between juxtapapillary duodenal diverticula and endoscopic retrograde cholangiopancreatography (ERCP) including treatments by using ERCP. Progress of Digestive Endoscopy, 76(2), 35-39, 2010.
18) Mamoru Takenaka, et al.: HOW TO MAKE THE PANCREATIC GUIDEWIRE METHOD SUCCESSFUL? Gastroenterological Endoscopy, 64(1), 70-78, 2022.
19) Shuichiro Umemura, et al.: Pancreatic Guidewire Cannulation and Transpancreatic Precut

Sphincterotomy in Difficult Biliary Cannulation. Journal of abdominal emergency medicine, 36(1), 47-52, 2016.
20) Kobayashi, Ryota, et al.: Fundamental Study of a Radiation Dose-Measuring Tool for Diagnostic X-Ray Apparatus. Bulletin of School of Health Sciences Tohoku University, 24(1), 39-44, 2015.
21) Hideki Kato.: Method of calculating the backscatter factor for diagnostic X-rays using the diffeential backscatter factor. Japanese Journal of Radiological Technology, 57(12), 1503-1510, 2001.
22) Donald L Miller, et al.: Reference levels for patient radiation doses in interventional radiology: proposed initial values for U.S. practice. Radiology, 253(3), 753-764, 2009.
23) C L Chapple, et al.: A phantom based method for deriving typical patient doses from measurements of dose-area product on populations of patients. Br J Radiol, 68(814), 1083-1086, 1995.
24) Ministry of Health, Labour and Welfare.: Part 2 Results of the Physical Condition Survey. The National Health and Nutrition Survey in Japan, 2019. https://www.mhlw.go.jp/content/001066903.pdf (Accessed 2 February 2026). 116, 2020.
25) Kanda Y: Investigation of the freely-available easy-to-use software "EZR" (Easy R) for medical statistics. Bone Marrow Transplant, 48, 452-458, 2013.
26) V Tsapaki, et al.: The impact of X-ray unit type used for endoscopic retrograde cholangiopancreatography procedures on patient doses. Radiat Prot Dosimetry, 171(4), 503-508, 2016.
27) K Smans, et al.: A study of the correlation between dose area product and effective dose in vascular radiology. Radiat Prot Dosimetry, 130(3), 300-308, 2008.
28) C J Larkin, et al.: Radiation doses to patients during ERCP. Gastrointest Endosc, 53(2), 161-164, 2001.
29) Chiaki Ookawara: Efforts to reduce radiation exposure in cardiac catheterization and interventional radiology. Medical journal of Tottori Red Cross Hospital, 31, 27-30, 2022. https://redcross.repo.nii.ac.jp/record/18566/files/09_%E5%A0%B1%E5%91%8A2.pdf (Accessed 2 February 2026)
30) Peter B Cotton, et al.: Grading the complexity of endoscopic procedures: results of an ASGE working party. Gastrointest Endosc, 73(5), 868-874, 2011.
31) Greger Olsson, et al.: The H.O.U.S.E. classification: a novel endoscopic retrograde cholangiopancreatography (ERCP) complexity grading scale. BMC Gastroenterol, 17(1), 38, 2017.
32) Touko Kaasalainen, et al.: Assessing Patient Radiation Exposure in Endoscopic Retrograde Cholangiopancreatography: A Multicenter Retrospective Analysis of Procedural Complexity and Clinical Factors. Diagnostics (Basel), 14(6), 656, 2024.
33) Hiroshige Mori, et al.: Examination of Types of Exposure and Management Methods for Nurses in Interventional Radiology. Japanese Journal of Radiological Technology, 63(4), 401-411, 2007.
34) Hiroshige Mori, et al.: A novel removable shield attached to C-arm units against scattered X-rays from a patient's side. Eur Radiol, 24(8), 1794-1799, 2014.
35) Hiroshige Mori: Action research regarding the optimisation of radiological protection for nurses during vascular interventional radiology. J Radiol Prot, 35(2), 457-466, 2015.
36) International Commission on Radiological Protection (ICRP). ICRP Statement on tissue reactions/early and late effects of radiation in normal tissues and organs—Threshold doses for tissue reactions in a radiation protection context. ICRP Publication 118. Annals of the ICRP 41 (1/2), ICRP, Ottawa, Ontario, 2012.
37) Kosuke Matsubara, et al.: A multicenter study of radiation doses to the eye lenses of medical staff performing non-vascular imaging and interventional radiology procedures in Japan. Phys Med, 74, 83-91, 2020.
38) Masaaki Akahane, et al.: Radiation Protection of the Eye Lens in Fluoroscopy-guided Interventional Procedures. Interventional Radiology, 7(2), 44-48, 2022.
39) Keisuke Nagamoto, et al.: A multicenter study of radiation doses to the eye lenses of clinical physicians performing radiology procedures in Japan. Journal of Occupational Health, 63(1), e12305, 2021.

Received July 7, 2024; accepted March 18, 2025

The current status and trends of entrance surface dose in general radiography in Kanagawa Prefecture

NITTA Masahiro[1)]*, WATANABE Hiroshi, Ph.D.[2)], SEKI Masashi[3)], SAKANO Tomokazu[4)], OGAWA Yasuyoshi[1)], YAMAMOTO Kazuyuki[5)], IWASAKI Masayuki[6)], INAGAKI Naoyuki[7)], TAKAHASHI Kouta[8)]

1) Department of Radiological Technology, St. Marianna University Hospital
2) School of Radiological Sciences, Faculty of Health Science, Gunma Paz University and Graduate School of Health Sciences, Gunma Paz University
3) Department of Radiology, Kitasato University Hospital
4) Department of Radiology, Yokohama City University Hospital
5) Department of Radiological Technology, Tokai University Hospital
6) Department of Radiological Technology, Tokai University Hachioji Hospital
7) Department of Radiology, Saiseikai Yokohamashi Tobu Hospital
8) Department of Radiology, Sagami Rinkan Hospital

* E-mail: masahiro.nitta@marianna-u.ac.jp

Note: This paper is secondary publication, the first paper was published in the JART, vol. 72 no. 874: 35-42, 2025.

Key words: diagnostic reference level, benchmark dose, X-ray dose investigation, dose optimization, general radiography

【Abstract】
In accordance with the revision of the Diagnostic Reference Levels (Japan DRLs), we conducted a questionnaire-based dose survey in 2021 to clarify the current status and trends of entrance surface dose (ESD) in general radiography in Kanagawa Prefecture. The survey included 274 medical institutions spanning 14 regions. The response rate was 24%. The mean ESD values were 0.14 ± 0.06 mGy for the Chest PA, 1.14 ± 0.72 mGy for the abdomen, and 0.096 ± 0.068 mGy for the infant chest. The 75th percentile values for all regions were below the 2020 Japan DRLs. Compared with the results of a survey conducted in 2015, the use of flat panel detectors has increased, leading to a decrease in the mean ESD.

1. Introduction

The International Commission on Radiological Protection (ICRP) recommends three fundamental principles of radiological protection. Among these, the justification of practices and the optimization of protection are essential in radiological imaging [1, 2]. Additionally, both the ICRP and the International Atomic Energy Agency advocate for the use of diagnostic reference levels (DRLs) as a key tool for optimizing radiation doses [3, 4].

In Japan, the initial DRLs (Japan DRLs 2015) were introduced in June 2015 by the Japan Network for Research and Information on Medical Exposure (J-RIME). Following the revision of the Ordinance for Enforcement of the Medical Care Act in March 2019, DRLs became an integral statutory and clinical benchmark for optimizing medical radiation exposure. The Japan DRLs 2015 were revised in July 2020, and the Japan DRLs 2020 now serve as the current national standard [5].

To optimize medical radiation exposure within the region, the Kanagawa Association of Radiological Technologists (KART) conducted a questionnaire-based survey in 2015. This survey assessed radiation doses in general radiography for three common examinations: adult chest (posteroanterior [PA]), adult abdomen (supine), and infant chest (aged 0–1 year) [6]. The results indicated that radiation doses in medical institutions across Kanagawa Prefecture were well-optimized relative to the nation-

al mean, leading to the development of benchmark doses as a novel, equipment-specific dose index.

Since more than 5 years have passed since the initial survey, and in light of the updates to the national DRLs, a new questionnaire-based survey (KANAGAWA 2021) was conducted in 2021 to re-evaluate the current dose levels in general radiography across the prefecture.

The objective of this study was to compare the KANAGAWA 2021 survey data with the Japan DRLs 2020 in order to assess the current status of general radiography doses in Kanagawa Prefecture and to examine the longitudinal trends in entrance surface dose (ESD) between 2015 and 2021.

2. Materials and Methods

2.1. Ethical Considerations

This study involved 274 medical institutions in Kanagawa Prefecture, all of which employed members of the KART. Questionnaires were distributed to each institution, and responses were gathered via a dedicated online survey platform. The study was conducted between April 1 and June 30, 2021. The study protocol received approval from the Institutional Review Board of the authors' affiliated institution (Approval No. 5112). The survey invitation letter clearly outlined the investigators' contact information, the voluntary nature of participation, the right to withdraw responses at any time, data privacy protocols concerning personal information, plans for disseminating the findings, and a guarantee that non-participation would not result in any disadvantage.

2.2. Data Collection

The questionnaire sought data on various radiographic parameters and institutional characteristics, including tube voltage, tube current-time product (mAs), added filtration (aluminum [Al] and copper [Cu]), source-to-image receptor distance (SID), irradiation field size, the use of an antiscatter grid, grid ratio, institutional classification, bed capacity, and type of image receptor. Additional questions assessed the methods employed to determine and review exposure settings, protocols for monitoring reject/retake rates, and the frequency of implementation of dose-reduction strategies.

In accordance with the Japan DRLs 2020, the survey examined 14 specific radiographic examinations: chest posteroanterior (PA) (<100 kV), chest PA (≥100 kV), chest PA for Medical check-up (≥100 kV), abdomen anteroposterior (AP) (supine), infant hip (ages 0–1 year), infant chest (ages 0–1 year), child chest (age 5 years), skull frontal (AP/PA), cervical spine AP, thoracic spine AP, thoracic spine lateral, lumbar spine AP, lumbar spine lateral, and pelvis AP. For adult examinations, the reported values were derived from the median data of 15 to 20 patients with a standard body weight of 50 to 60 kg. Pediatric patients were strictly defined as those aged 0 to 1 year for infants and 5 years for child.

2.3. Calculation of ESD

ESD was calculated using the "Estimation of Patient Dose in Diagnostic X-ray Examination" (EPD) software developed by Sato [7]. EPD is an advanced tool based on the numerical dose determination (NDD) method. Like NDD-Modify [8], EPD can compute both ESD and organ/tissue doses for standard radiographic examinations, depending on the exposure parameters employed. Additionally, EPD is officially recommended as a calculation tool for ESD and organ doses in general radiography, as outlined in the DRL operational manual published by the Japanese Society of Radiological Technology (JSRT) [9]. For this study, only the ESD values generated by the EPD software were used for analysis.

2.4. Statistical Analysis

Statistical analysis was performed using the Mann-Whitney U test. A P value of < .05 was

considered statistically significant. All analyses were conducted using Microsoft Excel (Microsoft Corporation).

3. Results

3.1. Survey Response Rate

The overall response rate was 24% (67 out of 274 institutions). Among the 67 responding institutions, general hospitals (excluding university hospitals) made up the largest group, with 43 facilities (64%), followed by university hospitals (including affiliated hospitals) with 12 (18%), clinics with 8 (12%), Medical check-up centers with 3 (4.5%), and a welfare facility with 1 (1.5%).

3.2. Dose Survey

Table 1 summarizes the number of responses, as well as the maximum, minimum, mean, standard deviation (SD), median, first quartile, third quartile, and maximum-to-minimum ratio for each anatomical region. The mean ESD ± SD was 0.14 ± 0.06 mGy for the chest PA (≥100 kV), 1.14 ± 0.72 mGy for the abdomen AP (supine), 0.096 ± 0.068 mGy for the infant chest (ages 0–1 year), 1.37 ± 0.75 mGy for the skull frontal (AP/PA), 2.04 ± 0.82 mGy for the lumbar spine AP, and 1.39 ± 0.64 mGy for the pelvis AP.

3.3. Types of Image Receptors

In adult examinations, flat-panel detectors (FPDs) were used in approximately 80% or more of the institutions across all anatomical regions, except for the skull frontal examination. For infant and child examinations, FPDs were used exclusively by all responding institutions (Fig. 1).

3.4. Comparison of ESD by Image Receptor

Table 2 presents the ESD values according to the type of image receptor. The mean ESD using FPDs was lower than the mean ESD using computed radiography (CR) for the following examinations: chest PA (<100 kV), chest PA (≥100 kV), abdomen AP (supine), cervical spine AP, thoracic spine AP, lumbar spine AP, lumbar spine lateral, and pelvis AP. However, there were no statistically significant differenc-

Table 1 Kanagawa prefecture survey results (2021) for entrance surface dose (ESD) in general radiography

Regions	Number of facilities	Maximum value (mGy)	Minimum value (mGy)	Mean value (mGy)	Standard deviation	Coefficient of variation	50% tile value (mGy)	25% tile value (mGy)	75% tile value (mGy)	Ratio of maximum value to minimum value
Chest PA (below 100 kV)	43	0.68	0.05	0.26	0.14	0.54	0.23	0.16	0.33	13.6
Chest PA (100 kV or above)	59	0.33	0.06	0.14	0.06	0.43	0.13	0.10	0.17	5.5
Chest PA (medical check-up)	40	0.28	0.056	0.14	0.06	0.43	0.13	0.10	0.17	5.0
Abdomen AP (supine)	56	3.4	0.33	1.14	0.72	0.63	0.94	0.66	1.47	10.3
Infant hip joint	29	0.72	0.03	0.12	0.13	1.08	0.08	0.06	0.12	24.0
Infant chest	31	0.31	0.03	0.096	0.068	0.71	0.08	0.05	0.11	10.3
Child chest	33	0.28	0.03	0.10	0.06	0.60	0.08	0.05	0.13	9.3
Skull	50	3.65	0.46	1.37	0.75	0.55	1.18	0.81	1.81	7.9
Cervical spine	53	1.37	0.09	0.45	0.25	0.56	0.42	0.3	0.58	15.2
Thoracic spine	50	3.50	0.41	1.65	0.79	0.48	1.57	0.95	2.13	8.5
Thoracic spine lateral	49	7.55	0.55	2.68	1.42	0.53	2.45	1.62	3.49	13.7
Lumbar spine	54	4.08	0.47	2.04	0.82	0.40	1.91	1.41	2.63	8.7
Lumbar spine lateral	53	14.53	0.92	5.22	2.52	0.48	4.73	3.61	6.26	15.8
Pelvis	52	3.04	0.54	1.39	0.64	0.46	1.31	0.91	1.75	5.6

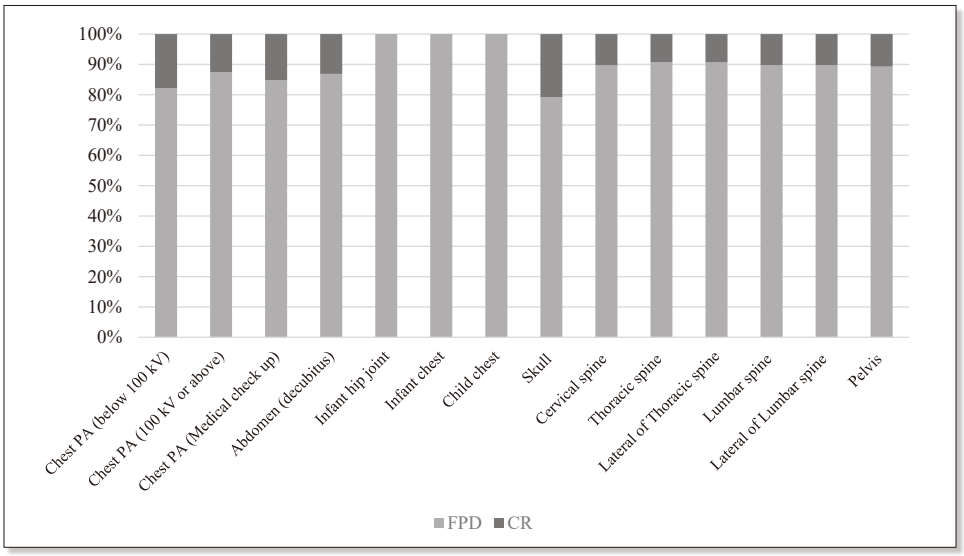

Fig. 1 Percentage of image receptors for each region in general radiography

Table 2 Comparison of entrance surface dose (ESD) for each image receptor in general radiography

Regions	Image receptor	Number of facilities	Mean value (mGy)	Standard deviation	test results	p value
Chest PA (below 100 kV)	FPD	35	0.25	0.13	NS	0.41
	CR	8	0.27	0.2		
Chest PA (100 kV or above)	FPD	52	0.14	0.06	NS	0.45
	CR	7	0.15	0.09		
Chest PA (medical check-up)	FPD	36	0.14	0.06	NS	0.31
	CR	4	0.14	0.02		
Abdomen AP (supine)	FPD	50	1.11	0.6	NS	0.41
	CR	6	1.23	1.2		
Skull	FPD	40	1.38	0.7	NS	0.49
	CR	10	1.37	1.01		
Cervical spine	FPD	48	0.44	0.22	NS	0.32
	CR	5	0.55	0.46		
Thoracic spine	FPD	46	1.63	0.78	NS	0.35
	CR	4	1.89	1.14		
Thoracic spine lateral	FPD	46	2.61	1.3	NS	0.14
	CR	3	2.11	0.58		
Lumbar spine	FPD	49	2.03	0.81	NS	0.42
	CR	5	2.14	1.14		
Lumbar spine lateral	FPD	48	5.11	2.27	NS	0.32
	CR	5	6.21	4.74		
Pelvis	FPD	47	1.38	0.62	NS	0.42
	CR	5	1.46	0.92		

NS: No significant

es in the mean ESD between FPDs and CR for any of the anatomical regions.

3.5. Awareness of the Japan DRLs 2020 and Institutional Doses

Regarding the comparison of institutional

dose levels with the Japan DRLs 2020, 25% of the institutions reported comparing their doses and concluded that no revision of exposure parameters was necessary. Twenty-four percent compared their doses and subsequently optimized their exposure parameters. Furthermore, 26% performed a comparison without making any adjustments to their protocols, and the remaining 25% had not compared their doses with the Japan DRLs 2020 (Fig. 2).

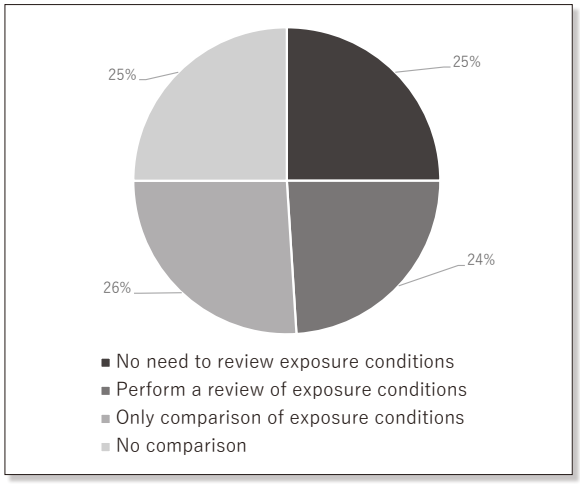

Fig. 2 Recognition of Japan DRLs 2020 and dose at each facility

4. Discussion

4.1. Comparison with the Japan DRLs 2020

Table 3 compares the median dose values between the KANAGAWA 2021 survey and 57 radiology specialist training institutions. It also compares the third quartile values among the KANAGAWA 2021 survey, the 57 radiology specialist training institutions, and the Japan DRLs 2020. The third quartile values in KANAGAWA 2021 were lower across all anatomical regions compared to the Japan DRLs 2020.

Compared to the training institutions, both the median and third quartile values in KANAGAWA 2021 were similar, with slight variations by anatomical region. This suggests that radiographic examinations in Kanagawa Prefecture are performed at doses comparable to those of radiology specialist training institutions, mostly consisting of university hospitals. However, for the chest PA (≥100 kV), abdomen AP (supine), skull frontal (AP/PA), thoracic spine AP, thoracic spine lateral, lumbar spine AP, lumbar spine lateral, and pelvis AP, the median values in KANAGAWA 2021 were higher

Table 3 Comparison of entrance surface dose (ESD) between survey results for Kanagawa prefecture (2021) and radiology specialist training institutions in general radiography

Regions	50% tile value (mGy)		75% tile value (mGy)		
	KANAGAWA 2021	Radiology specialist training institution	KANAGAWA 2021	Radiology specialist training institution	Japan DRLs 2020
Chest PA (below 100 kV)	0.23	0.24	0.33	0.38	0.4
Chest PA (100 kV or above)	0.13	0.1	0.17	0.18	0.3
Abdomen AP (supine)	0.94	0.93	1.47	1.64	2.5
Infant hip joint	0.08	0.09	0.12	0.12	0.2
Infant chest	0.08	0.08	0.11	0.11	0.2
Child chest	0.08	0.1	0.13	0.16	0.2
Skull	1.18	0.94	1.81	1.45	2.5
Cervical spine	0.42	0.46	0.58	0.63	0.8
Thoracic spine	1.57	1.35	2.13	1.84	3
Thoracic spine lateral	2.45	2.11	3.49	3.01	5
Lumbar spine	1.91	1.55	2.63	2.27	3.5
Lumbar spine lateral	4.73	3.61	6.26	5.17	9
Pelvis	1.31	1.17	1.75	1.66	2

than those in the training institutions. This discrepancy is likely due to the fact that data from training institutions are mainly derived from university hospitals and large medical facilities, where advanced infrastructures are in place, and dose optimization is more developed. In contrast, the KANAGAWA 2021 survey collected data from a wide range of facilities in Kanagawa Prefecture, from university hospitals to small clinics with varying scales and institutional characteristics. This diversity likely explains the higher median values observed in certain regions compared to those of the training institutions.

Because the KANAGAWA 2021 survey includes a broad range of facilities, such as general clinics and small-to-medium-sized institutions, it provides an accurate representation of the conditions throughout Kanagawa Prefecture, without bias toward any particular type of medical institution. Based on this representative data, there is room for further dose optimization in the anatomical regions mentioned earlier. However, as shown in the results (Section 3.5), 75% of the surveyed institutions have already compared their dose levels with the Japan DRLs 2020, indicating that some degree of optimization has been implemented. Moving forward, it is essential to continue promoting educational initiatives on dose optimization for institutions that have not yet conducted comparisons with the Japan DRLs 2020, helping to facilitate broader optimization across all facilities.

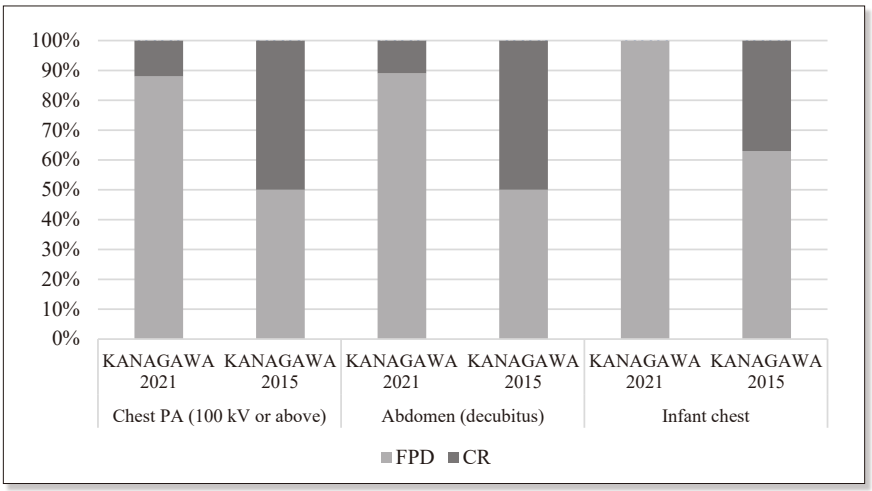

Fig. 3 Comparison of the percentage of image receptors between Kanagawa Prefecture survey results in 2021 and 2015

Table 4 Comparison of entrance surface dose (ESD) between Kanagawa prefecture survey results in 2021 and 2015 in general radiography

Regions	Survey type	Number of facilities	Mean value (mGy)	Standard deviation	test results	p value
Chest PA (100 kV or above)	KANAGAWA 2021	59	0.14	0.06	**	0.3×10^{-9}
	KANAGAWA 2015	96	0.20	0.20		
Abdomen AP (supine)	KANAGAWA 2021	56	1.14	0.72	**	0.003
	KANAGAWA 2015	89	1.40	0.70		
Infant chest	KANAGAWA 2021	31	0.096	0.068	NS	0.8
	KANAGAWA 2015	48	0.099	0.056		

NS: No significant
* : $p < 0.05$
** : $p < 0.01$

4.2. Comparison with the 2015 Survey (KANAGAWA 2015)

Compared with the KANAGAWA 2015 survey, the utilization rate of FPDs in the KANAGAWA 2021 survey increased for the chest PA (≥100 kV), abdomen AP (supine), and infant chest, reaching 100% for the infant chest (Fig. 3).

Table 4 compares the mean ESDs for the chest PA (≥100 kV), abdomen AP (supine), and infant chest. The mean ESD ± SD in KANAGAWA 2021 was 0.14 ± 0.06 mGy, 1.14 ± 0.72 mGy, and 0.096 ± 0.068 mGy, respectively. Compared with the KANAGAWA 2015 values of 0.20 ± 0.20 mGy, 1.40 ± 0.70 mGy, and 0.099 ± 0.056 mGy, the doses for the chest PA (≥100 kV) and abdomen AP (supine) decreased significantly (P < .01), whereas no significant difference was observed for the infant chest (P = .80).

Table 5 shows a comparison of the mean ESDs specifically for FPDs in these same three regions. The values in KANAGAWA 2021 were 0.14 ± 0.06 mGy, 1.11 ± 0.60 mGy, and 0.096 ± 0.068 mGy, respectively, compared to 0.16 ± 0.06 mGy, 1.20 ± 0.60 mGy, and 0.086 ± 0.048 mGy in KANAGAWA 2015. A significant decrease was noted only for the chest PA (≥100 kV) (P < .05), with no significant differences for the abdomen AP (supine) or infant chest (P = .29 and P = .81, respectively).

Table 6 compares the mean ESDs specifically for CR in the chest PA (≥100 kV) and abdomen AP (supine). The KANAGAWA 2021 values of 0.15 ± 0.09 mGy and 1.23 ± 1.21 mGy showed a significant decrease in the chest PA (≥100 kV) (P < .05) compared to the KANAGAWA 2015 values of 0.24 ± 0.10 mGy and 1.6 ± 0.70 mGy. No significant difference was observed for the abdomen AP (supine) (P = .49).

The significant decrease in the mean ESD for the chest PA (≥100 kV) across all image receptor types suggests that institutions have actively assessed their dose levels and optimized their

Table 5 Comparison of entrance surface dose (ESD) in flat panel detector (FPD) between Kanagawa prefecture survey results in 2021 and 2015 in general radiography

Regions	Survey type	Number of facilities	Mean value (mGy)	Standard deviation	test results	p value
Chest PA (100 kV or above)	KANAGAWA 2021	52	0.14	0.06	*	0.02
	KANAGAWA 2015	48	0.16	0.06		
Abdomen AP (supine)	KANAGAWA 2021	50	1.11	0.60	NS	0.29
	KANAGAWA 2015	44	1.20	0.60		
Infant chest	KANAGAWA 2021	31	0.096	0.068	NS	0.81
	KANAGAWA 2015	30	0.086	0.048		

NS: No significant
* : $p < 0.05$
** : $p < 0.01$

Table 6 Comparison of entrance surface dose (ESD) in computed radiography (CR) between Kanagawa prefecture survey results in 2021 and 2015 in general radiography

Regions	Survey type	Number of facilities	Mean value (mGy)	Standard deviation	test results	p value
Chest PA (100 kV or above)	KANAGAWA 2021	7	0.15	0.09	*	0.02
	KANAGAWA 2015	47	0.24	0.10		
Abdomen AP (supine)	KANAGAWA 2021	6	1.23	1.21	NS	0.49
	KANAGAWA 2015	44	1.6	0.70		

NS: No significant
* : $p < 0.05$
** : $p < 0.01$

Table 7 Comparison of entrance surface dose (ESD) between survey results for Kanagawa prefecture (2021) and Rosai hospital group (2016) for each image receptor in general radiography

Regions	Image receptor	Survey type	Number of facilities	Mean value (mGy)	Standard deviation	test results	p value
Chest PA (100 kV or above)	FPD	KANAGAWA 2021	52	0.14	0.06	*	0.02
		Rosai[a]	16	0.16	10.6		
	CR	KANAGAWA 2021	7	0.15	0.09	NS	0.13
		Rosai[a]	15	0.21	10.2		
Infant hip joint	FPD	KANAGAWA 2021	29	0.12	0.13	NS	1.00
		Rosai[a]	10	0.12	4.1		
	CR	KANAGAWA 2021	–	–	–	–	–
		Rosai[a]	–	–	–		
Infant chest	FPD	KANAGAWA 2021	31	0.096	0.068	NS	0.26
		Rosai[a]	11	0.11	23.9		
	CR	KANAGAWA 2021	–	–	–	–	–
		Rosai[a]	–	–	–		
Child chest	FPD	KANAGAWA 2021	33	0.10	0.06	NS	0.06
		Rosai[a]	12	0.12	22.1		
	CR	KANAGAWA 2021	–	–	–	–	–
		Rosai[a]	–	–	–		
Abdomen AP (supine)	FPD	KANAGAWA 2021	50	1.11	0.6	NS	0.41
		Rosai[a]	16	1.04	8.6		
	CR	KANAGAWA 2021	6	1.23	1.2	NS	0.27
		Rosai[a]	15	1.84	5.9		
Skull	FPD	KANAGAWA 2021	40	1.38	0.7	**	0.01
		Rosai[a]	13	1.08	3.4		
	CR	KANAGAWA 2021	10	1.37	1.01	NS	0.39
		Rosai[a]	18	1.53	3.5		
Cervical spine	FPD	KANAGAWA 2021	48	0.44	0.22	NS	0.35
		Rosai[a]	14	0.41	0.8		
	CR	KANAGAWA 2021	5	0.55	0.46	NS	0.93
		Rosai[a]	17	0.57	3.2		
Thoracic spine	FPD	KANAGAWA 2021	46	1.63	0.78	**	0.001
		Rosai[a]	15	1.21	3.5		
	CR	KANAGAWA 2021	4	1.89	1.14	NS	0.45
		Rosai[a]	16	2.38	3.2		
Thoracic spine lateral	FPD	KANAGAWA 2021	46	2.61	1.3	NS	0.38
		Rosai[a]	15	2.44	14.2		
	CR	KANAGAWA 2021	3	2.11	0.58	*	0.04
		Rosai[a]	16	4.74	6.4		
Lumbar spine	FPD	KANAGAWA 2021	49	2.03	0.81	**	0.001
		Rosai[a]	15	1.6	5.1		
	CR	KANAGAWA 2021	5	2.14	1.14	NS	0.23
		Rosai[a]	16	3.18	2.8		
Lumbar spine lateral	FPD	KANAGAWA 2021	48	5.11	2.27	NS	0.22
		Rosai[a]	15	4.79	4.8		
	CR	KANAGAWA 2021	5	6.21	4.74	NS	0.16
		Rosai[a]	16	8.37	3.6		
Pelvis	FPD	KANAGAWA 2021	47	1.38	0.62	**	0.01
		Rosai[a]	15	1.12	3.4		
	CR	KANAGAWA 2021	5	1.46	0.92	NS	0.28
		Rosai[a]	16	1.97	4.5		

a : Rosai hospital group survey results (2016)

NS: No significant
* : $p < 0.05$
** : $p < 0.01$

exposure parameters. The 2015 dose survey and the ongoing efforts of KART—which include calculating institutional doses and providing feedback by comparing them with the 2015 Japan DRLs and KANAGAWA 2015—are believed to have contributed significantly to dose optimization in general radiography within Kanagawa Prefecture. Furthermore, although no significant difference in the mean ESD by image receptor type was observed for the abdomen AP (supine), the overall mean ESD decreased significantly. This overall reduction is likely attributed to the increased adoption of FPDs, indicating that the widespread implementation of FPDs has contributed to ESD reduction in Kanagawa Prefecture.

For the infant chest (ages 0–1 year), no significant difference in the mean ESD was observed when using FPDs exclusively. This is likely due to the already low baseline dose, and the detective quantum efficiency (DQE) of FPDs does not substantially exceed that of CR at such low dose levels [10]. Thus, achieving further substantial dose reduction is difficult. Additionally, the number of responses for the infant chest (ages 0–1 year) was small, and since facilities performingradiography are limited, it is possible that the responding institutions in both surveys were largely the same.

4.3. Comparison between FPD and CR

Regarding the lack of a significant difference in ESD between FPDs and CR in the KANAGAWA 2021 survey, our results diverge from the findings of Fukuda et al [11], who reported that FPDs yielded significantly lower doses in 9 of 18 anatomical regions. Table 7 presents a comparison between the results of Fukuda et al. and KANAGAWA 2021.

Compared to the findings of Fukuda et al., the mean ESDs using FPDs in KANAGAWA 2021 were significantly higher in four regions: the skull, thoracic spine AP, lumbar spine AP, and pelvis. In contrast, the mean ESD using CR in KANAGAWA 2021 was significantly lower only for the thoracic spine lateral, with no significant differences observed in other regions. These findings suggest two possibilities: first, that the exposure parameters for CR in Kanagawa Prefecture have been sufficiently optimized, and second, that despite the increased utilization rate of FPDs, some institutions may still be using legacy CR exposure parameters for FPDs, thereby failing to fully exploit the dose-reduction potential of FPDs.

5. Conclusion

This study clarified the current status of ESD in general radiography within Kanagawa Prefecture and outlined the dose trends between 2015 and 2021. The KANAGAWA 2021 survey showed that the ESDs for all evaluated anatomical regions were below the Japan DRLs 2020. Furthermore, our findings confirmed that radiographic examinations in the prefecture are performed at dose levels comparable to those at radiology specialist training institutions. Additionally, the utilization rate of FPDs has increased since 2015, with over 80% of the surveyed institutions transitioning from CR to FPDs.

By conducting a detailed investigation stratified by region and type of image receptor and providing direct feedback to participating institutions, this study successfully facilitated further dose optimization. These efforts have significantly contributed to the optimization of medical radiation exposure in Kanagawa Prefecture. Moving forward, we anticipate that implementing similar surveys in other regions will promote local dose optimization efforts, ultimately supporting nationwide optimization of medical radiation exposure.

Disclosure of Conflicts of Interest

The author and co-authors have no conflicts of interest to disclose.

Acknowledgments

The authors express their sincere gratitude to the staff at the participating medical institutions in Kanagawa Prefecture for their invaluable cooperation in the dose survey, and to the members of the Radiation Safety Committee of the Kanagawa Association of Radiological Technologists (KART). This survey was conducted as part of the medical radiation exposure optimization project led by the KART Radiation Safety Committee. Portions of this study were presented at the Kanto-Koshinetsu Academic Conference of Radiological Technologists, held in Gunma, Japan, in 2022.

References

1) International Commission on Radiological Protection (ICRP): The 2007 Recommendations of the International Commission on Radiological Protection. ICRP Publication 103. Ann ICRP, 37(2-4), 2007.
2) International Commission on Radiological Protection (ICRP): Radiological protection in medicine. ICRP Publication 105. Ann ICRP, 37(6), 2007.
3) International Commission on Radiological Protection (ICRP): Radiological protection and safety in medicine. ICRP Publication 73. Ann ICRP, 26(2), 1996.
4) International Atomic Energy Agency (IAEA): International Basic Safety Standards for Protection Against Ionizing Radiation and for the Safety of Radiation Sources. IAEA Safety Series No. 115, Vienna, Austria, IAEA, 1996.
5) Japan Network for Research and Information on Medical Exposure (J-RIME): National Diagnostic Reference Levels in Japan. http://www.radher.jp/J-RIME/report/JapanDRL2020_jp.pdf (accessed September 1, 2022), 2020. [in Japanese]
6) Watanabe H, et al.: Propose for the Benchmark Dose (BD) for the Optimization of Protection in Medical Exposure in General Radiography. Jpn J Radiol Technol, 74(5), 443-451, 2018. [in Japanese]
7) Ibaraki Association of Radiological Technologists: Estimation of patient dose in diagnostic x-ray examination (EPD). http://www.iart-web.org/public/epd.html (accessed August 20, 2022). [in Japanese]
8) Mori T, et al.: A Study of Creating Guidance Level in Medical Exposure. J Suzuka Univ Med Sci, 4, 109-129, 1997. [in Japanese]
9) Japanese Society of Radiological Technology (JSRT): Diagnostic reference level operation manual. http://www.jsrt.or.jp/data/wpontent/uploads/2013/07/drl_manual_20161001_ver3.pdf (accessed August 1, 2022). [in Japanese]
10) Kunitomo H, et al.: Physical image properties of digital radiography systems in low dose range. Jpn J Radiol Technol, 68(8), 961-969, 2012. [in Japanese]
11) Fukuda T, et al.: Proposal for Rosai Diagnostic Reference Levels (DRLs) as Local DRLs and Benchmark Doses (BDs) in General Radiography. J Japan Assoc Radiol Technol, 67(1), 21-28, 2020. [in Japanese]

Received December 16, 2024; accepted April 20, 2025

Effect of ultrasound experience on the measurement accuracy of bladder ultrasound

KAWASAKI Yoshiyuki[1)*], YOSHIDA Tatsuya[2)], HAYAKAWA Tomoki[2)], KAWADAI Toshiyuki[2)]

1) Department of Radiology, Okinawa Central Hospital
2) Department of central Radiology, Tatebayashi Kosei General Hospital

* E-mail: zenkou0226@gmail.com

Note: This paper is secondary publication, the first paper was published in the JART, vol. 72 no. 875: 20-24, 2025.

Key words: Ultrasound skill, Measurement accuracy, Bladder volume, Prostate, Radiotherapy

【Abstract】
Purpose: Ultrasound devices are used in radiation therapy for prostate cancer, and there have been scattered reports on their measurement accuracy. However, no reports have examined differences in accuracy between operators. Thus, this study evaluated the impact of operator experience on bladder ultrasound measurement accuracy.
Methods: Bladder volume measured by ultrasound was compared between experienced and inexperienced operators. The reference values were obtained from the bladder region of interest on treatment planning computed tomography images.
Results: The difference from the reference values was − 4.5 ± 31.4 mL in the experienced group, versus − 19.9 ± 36.0 mL in the inexperienced group. A strong correlation was observed with the reference values in both the experienced (correlation coefficient = 0.91) and inexperienced groups (correlation coefficient = 0.88), with no difference in coefficients between the groups.
Conclusion: The measurement accuracy of the inexperienced group was comparable to that of the experienced group when the bladder volume was ≥150 mL.

Introduction

Given the increasing incidence of prostate cancer [1)], radiation therapy has become a common treatment option, providing comparable therapeutic outcomes as surgical intervention [2, 3)]. To ensure the safe delivery of high-precision radiotherapy, the integration of image-guided radiotherapy with advanced techniques, such as three-dimensional conformal radiotherapy, intensity-modulated radiotherapy, and volumetric-modulated arc therapy, has been widely recommended in recent years [2–4)].

Historically, radiation-induced proctitis leading to rectal bleeding was considered the most significant late complication. Although this event typical manifests between 6 months and several years post-treatment, its subsequent onset is rare [4–7)]. Conversely, urinary tract adverse events remain a persistent clinical challenge. These complications can occur even 5 years after radiotherapy, with the reported incidence of grade 2 or higher toxicity ranging 13%–23% [4–7)]. To mitigate these urinary adverse events, an increasing number of facilities have implemented bladder filling protocols [8–10)]. Reports suggest that treatment should ideally be performed with a bladder volume of 100–250 mL [8–10)]. Consequently, the efficacy of bladder ultrasound diagnostic devices for verifying bladder volume has been well documented [11–17)]. Given this background, many institutions are currently utilizing bladder ultrasound to reproduce the specific bladder volume established during the treatment planning stage [11–17)].

Whereas various studies have evaluated the performance of bladder ultrasound [11–17)], to the best of our knowledge, there are no reports assessing the accuracy of this technique in relation to the operator's experience level. At our institution, radiological technologists perform bladder ultrasound examinations. Therefore, this study investigated and compared the differences in bladder volume measurements ob-

tained by experienced and inexperienced staff members using a bladder ultrasound diagnostic device.

1. Materials and Methods

1.1. Equipment

The BVI6100 bladder ultrasound system (Verathon Inc., Bothell, WA, USA) was used in this study (Fig. 1a). The measurement accuracy of this device has been previously validated [14–16]. BVI6100 acquires images in B-mode, and it is characterized by its ability to estimate the bladder volume by integrating bladder cross-sections. Bladder volume estimation is achieved by fanning the probe to create images in 12 directions at 15° intervals. Additionally, the device features an assistive function that displays arrows to indicate the bladder's location if it is not visible on the screen (Fig. 1b), allowing the staff to adjust the scan based on this information.

A standardized bladder volume measurement manual has been established at our institution. According to this protocol, the area near the superior border of the pubic symphysis is scanned three times, with the probe position adjusted according to the assistive function. The average of the three scans is then recorded as the final measurement. The measurement procedure is illustrated in Fig. 1c.

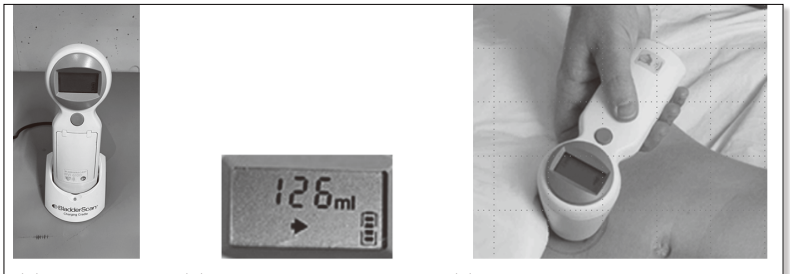

(a) BVI 6100 (b) Measurement screen (c) Bladder volume measurement

Fig. 1 Bladder ultrasound diagnostic imaging device and bladder volume measurement

(a) Bladder ultrasound diagnostic imaging device: BVI 6100
(b) Measurement screen
(c) Bladder volume measurement

1.2. Subjects

The study included 90 patients with prostate cancer (mean age: 74.5 ± 4.9 years) who underwent radiation therapy at our institution between January 2018 and December 2020 and provided informed consent. The operators were radiological technologists involved in radiotherapy clinical practice, consisting of four experienced (experienced group) and four inexperienced operators (inexperienced group).

This study was reviewed and approved by the Institutional Review Board of our institution (Approval No. 2018003).

1.3. Definition of the Bladder Region of Interest (ROI)

Immediately prior to treatment planning computed tomography (CT), the bladder volume was measured by ultrasound three times in the supine position, and the mean volume was calculated for each operator. Following the measurements, treatment planning CT images were acquired with a slice thickness of 3 mm and transferred to the Pinnacle^3 R10.0 treatment planning system (Koninklijke Philips N.V., Amsterdam, Netherlands).

Subsequently, the bladder ROI was defined to determine the bladder volume. To ensure reproducibility, the bladder inner walls were contoured by three radiological technologists with more than 5 years of experience in radiotherapy, and the contours were subsequently verified by a radiation oncologist [14]. A representative example of the bladder ROI is presented in Fig. 2.

The target bladder volume was set at 200 mL. Treatment planning CT was performed 30, 45, and 60 min after the intake of 500 mL of water, and additional scans were conducted if necessary. Bladder volume measurements were performed immediately before each scan.

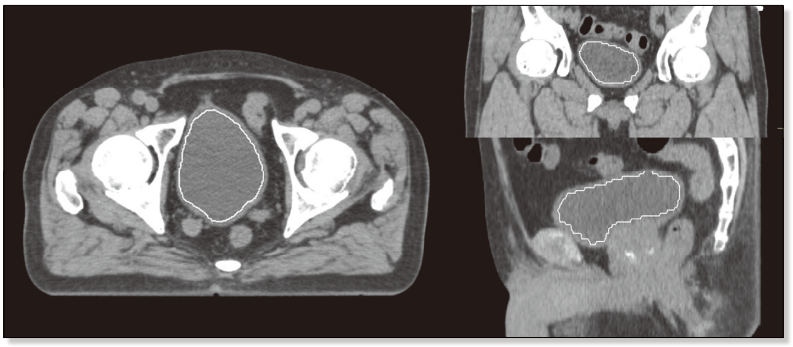

Fig. 2 Example of a bladder region of interest

For patients who could not tolerate bladder filling, the measurement process was discontinued at 45 min.

1.4. Statistical Analysis

The bladder volume (cm^3) calculated from the ROI on the treatment planning system was defined as the reference value, whereas the value measured by the bladder ultrasound diagnostic device (mL) was defined as the mean of three measurements. For both the experienced and inexperienced groups, the regression line, coefficient of determination (R^2), and correlation coefficient between the measured and reference values were analyzed [15].

Next, the measurement error was calculated by comparing the reference and measured values [15]. Letting M_{US} be the volume measured by the bladder ultrasound diagnostic device and M_{RTPS} be the volume calculated from the ROI on the treatment planning system, the absolute percentage error [$\varepsilon_{(Ab)}$ (%)] and percentage error [ε (%)] were calculated using equations (1) and (2), respectively, as follows:

$$\varepsilon_{(Ab)}\,\% = \frac{M_{US} - M_{RTP}}{M_{RTP}} \times 100 \quad \cdots\cdots (1)$$

$$\varepsilon\,\% = \frac{M_{US} - M_{RTP}}{M_{RTP}} \times 100 \quad \cdots\cdots (2)$$

$\varepsilon_{(Ab)}$ was used to assess the fixed error, whereas ε was used to identify potential bias. ε (relative error) was evaluated across different bladder volume categories [15]. Based on reports suggesting an optimal bladder volume of 100–250 mL for treatment planning [8, 9], we determined that measurement accuracy within this range is critical. Therefore, bladder volumes were categorized as follows: ≤99 mL, 100–149 mL, 150–199 mL, 200–249 mL, and ≥250 mL.

The Kruskal–Wallis test was employed to compare error rates. The correlation between the reference values from treatment planning CT and the measured values from ultrasound was analyzed using Spearman's rank correlation coefficient (ρ). All statistical analyses were performed using EZR (Easy R version 1.68; Saitama Medical Center, Jichi Medical University, Saitama, Japan) [18].

2. Results

2.1. Differences Relative to Reference Values

In total, 134 measurements were performed in the experienced group, and 133 measurements were performed in the inexperienced group. The correlation between the reference and measured values is presented in Fig. 3. The mean difference between the measured and reference values was −4.5 ± 31.4 mL for the experienced group, versus −19.9 ± 36.0 mL for the inexperienced group, reflecting a large underestimation in the inexperienced group.

The regression lines and R2 derived from the correlation plots were y = 0.92x + 12.70 (R^2 = 0.91) for the experienced group and y = 0.90x + 2.36 (R^2 = 0.88) for the inexperienced group. ρ was 0.956 ($p < 0.05$) for the experienced group and 0.943 ($p < 0.05$) for the inexperienced group, indicating strong positive correlations between the measured and reference values for both groups.

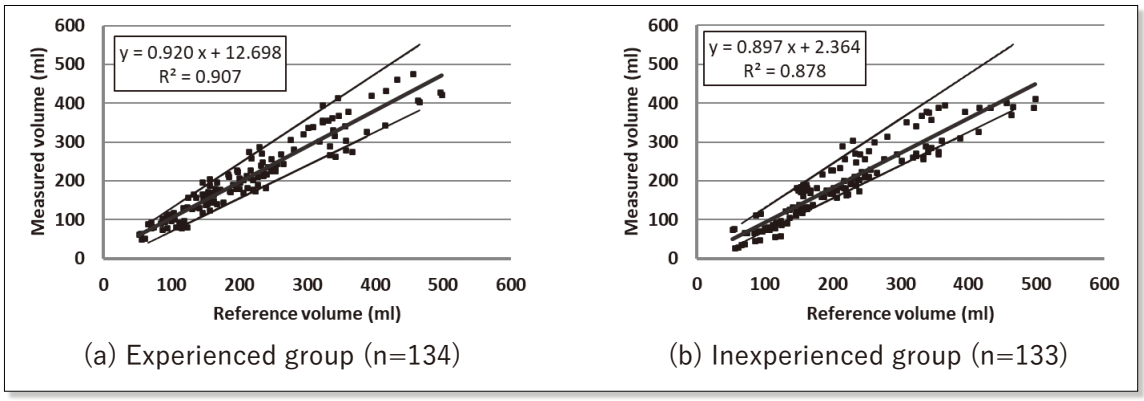

Fig. 3 Correlation diagram between the reference and measured values
(a) Experienced group (b) Inexperienced group

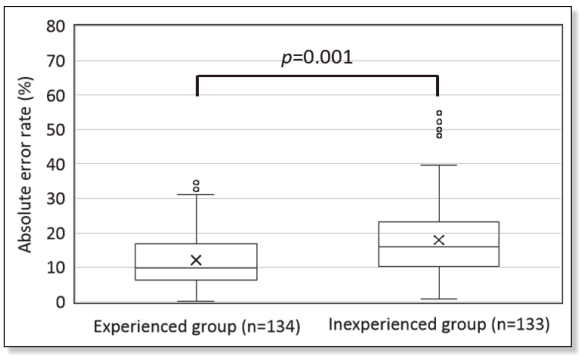

Fig. 4 Absolute error rate obtained from the reference and measured values

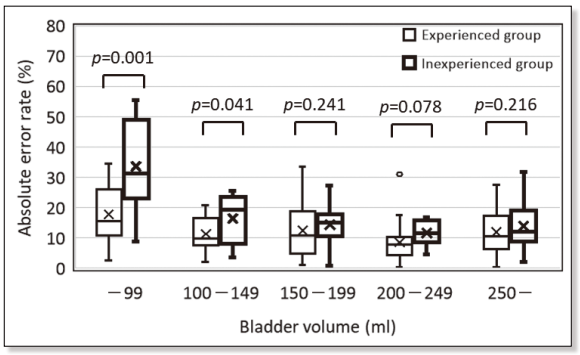

Fig. 5 Absolute error rate for each bladder volume

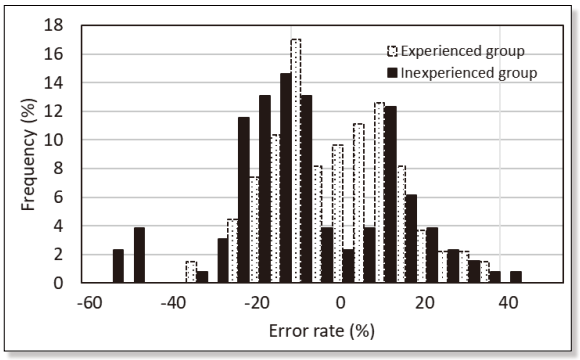

Fig. 6 Histogram of the error rate

2.2. Measurement Errors

$\varepsilon_{(Ab)}$ for all data is presented in Fig. 4. $\varepsilon_{(Ab)}$ categorized by bladder volume is presented in Fig. 5, and the histogram of ε is presented in Fig. 6. The numbers of data points for bladder volumes of ≤99, 100–149, 150–199, 200–249, and ≥250 mL were 19, 21, 29, 26, and 39, respectively, for the experienced group and 26, 18, 33, 16, and 40, respectively, for the inexperienced group.

Mean $\varepsilon_{(Ab)}$ was 12.2% ± 7.9% for the experienced group and 18.0% ± 11.5% for the inexperienced group ($p < 0.05$). Regarding the errors by bladder volume, mean $\varepsilon_{(Ab)}$ for volumes ≤ 99 mL was high in both groups (17.8% ± 9.9% for the experienced group and 33.7% ± 13.9% for the inexperienced group). However, for volumes ≥ 100 mL, both groups displayed more stable results than those at ≤99 mL. A comparison of mean ε between the two groups for each volume category revealed a significant difference ($p < 0.05$) for volumes ≤ 149 mL, whereas no significant difference was observed for volumes ≥ 150 mL.

The proportion of measurements within the manufacturer's specified accuracy range (±15% or ±15 mL) was 89.6% for the experienced group, compared with 83.5% for the inexperienced group. The histogram indicated that the inexperienced group had a lower frequency of accurate measurements and higher frequencies of overestimation and underestimation, exhib-

iting a non-normal distribution.

3. Discussion

Although several studies have evaluated the measurement accuracy of bladder ultrasound diagnostic devices in the context of radiotherapy [14–18], to our knowledge, no previous reports assessed the impact of the staff's ultrasound experience. This study evaluated the influence of experience in ultrasound examination on measurement accuracy using a dedicated device for bladder volume measurement.

Our results demonstrated a strong correlation between the reference and measured values regardless of the ultrasound experience of the operator. However, the reported values for the inexperienced group relative to the reference values were underestimated by an average of approximately 15 mL, and mean $\varepsilon_{(Ab)}$ was approximately 4% higher in this group than in the experienced group. Furthermore, a significant difference ($p < 0.05$) in the error rate was observed for bladder volumes ≤ 149 mL, whereas no such difference was found for volumes ≥ 150 mL. Although the reported optimal bladder volume for prostate cancer treatment is 100–250 mL, our findings suggest that although measurements are sensitive to the staff's experience within the 100–149-mL range, the impact of experience is negligible within the 150–250-mL range. We hypothesize that for bladder volumes exceeding a certain threshold, the device's bladder-positioning assist function facilitates reliable identification of the bladder, thereby eliminating significant differences between the two groups.

Conversely, the significant differences observed for volumes ≤ 149 mL, despite the assist function, might be attributable to several factors. First, as the manufacturer's specified accuracy is ±15% or ±15 mL, the relative device error becomes more pronounced at smaller bladder volumes. Second, measurement fluctuations might arise from differences in probe handling skills. Third, interference from intestinal gas might lead to errors even when the bladder location is partially identified. These factors are reflected in the distribution of $\varepsilon_{(Ab)}$. Specifically, the distribution was approximately normal in the experienced group but bimodal in the inexperienced group.

We believe that this bimodal distribution in the inexperienced group was primarily caused by unstable probe placement during measurement. Interviews with the staff revealed that the experienced group employed specific techniques: pre-identifying the optimal probe approach by reviewing prior images; ensuring the probe remained fixed and steady during the scan; and performing the measurement while the patient held their breath. Although the inexperienced group followed the standardized manual, they did not implement these additional measures. Pre-identifying the approach helps avoid signal attenuation from gas or bone and ensures accurate bladder identification. Stabilizing the probe prevents fluctuations during the approximately 5-s scan, leading to more consistent integrated volume values. Breath-holding further reduces respiration-induced motion artifacts. We conclude that the accumulation of these refined techniques in the experienced group significantly enhanced measurement accuracy. By incorporating these techniques into training, the mean differences and $\varepsilon_{(Ab)}$ in the inexperienced group, particularly for volumes ≤ 149 mL, are likely to improve. Future studies should evaluate the measurement accuracy of staff following such targeted education.

4. Conclusion

This study evaluated the impact of ultrasound examination experience on the accuracy of bladder volume measurement. Our findings demonstrated that although the measurement accuracy of the inexperienced group was inferior for bladder volumes of ≤149 mL, com-

parable accuracy was recorded between the groups for volumes of ≥150 mL.

Conflict of Interest (COI)

The first author and all co-authors have no conflicts of interest to disclose.

Previous Presentation

A part of this study was presented at the 38th Japan Association of Radiological Technologists (JART) Conference, Kobe, Hyogo, Japan.

References

1) National Cancer Center Japan, Cancer Information Service: Cancer Statistics in Japan. Available from: https://ganjoho.jp/reg_stat/statistics/stat/summary.html [Accessed 5th July 2024] (in Japanese).
2) Japanese Society for Radiation Oncology (Ed): JASTRO Guidelines 2020 for Radiotherapy Treatment Planning. 248–268, Kanehara & Co., Ltd.; 2020 (in Japanese).
3) Ohnishi H, et al.: Cancer and Radiation Therapy (Revised 8th Edition). 248–253, Gakken; 2023 (in Japanese).
4) NCCN Prostate Cancer Panel Members: Prostate Cancer, NCCN Clinical Practice Guidelines in Oncology; Version 3. 2022.
5) Aizawa R, et al.: Low incidence of late recurrence in patients with intermediate-risk prostate cancer treated by intensity-modulated radiation therapy plus short-term androgen deprivation therapy. Int J Clin Oncol, 25(4), 713–719, 2020.
6) Aizawa R, et al.: Ten-year outcomes of high-dose intensity-modulated radiation therapy for nonmetastatic prostate cancer with unfavorable risk: early initiation of salvage therapy may replace long-term adjuvant androgen deprivation. Int J Clin Oncol, 24(10), 1247–1255, 2019.
7) Tomita N, et al.: Favorable 10-year outcomes of image-guided intensity-modulated radiotherapy combined with long-term androgen deprivation for Japanese patients with nonmetastatic prostate cancer. Asia Pac J Clin Oncol, 15(1), 18–25, 2019.
8) Fujioka C, et al.: Optimal bladder volume at treatment planning for prostate cancer patients receiving volumetric modulated arc therapy. Pract Raiat Oncol, 6(6), 395–401, 2016.
9) Kawasaki Y, et al.: Optimal bladder volume in IMRT planning for prostate cancer. The journal of the Japanese Association of Radiological Technicians, 62(5), 22–26, 2015 (in Japanese).
10) Narita H, et al.: Radiation Therapy Planning. 147–153, Pillar Press, 2018 (in Japanese).
11) Ung KA, et al.: Comparison study of portable bladder scanner versus cone-beam CT scan for measuring bladder volumes in post-prostatectomy patients undergoing radiotherapy. J Med Imaging Radiat Oncol, 58(3), 377–383, 2014.
12) Stam MR, et al.: Bladder filling variation during radiation treatment of prostate cancer: can the use of a bladder ultrasound scanner and biofeedback optimize bladder filling? Int J Radiat Oncol Biol Phys, 65(2), 371–377, 2006.
13) Ohira S, et al.: Improvement in bladder volume reproducibility using A-mode portable ultrasound bladder scanner in moderate-hypofractionated volumetric modulated arc therapy for prostate cancer patients. J Appl Clin Med Phys, 23(4), e13546, 2022.
14) Kawasaki Y, et al.: Measurement Accuracy of the Bladder Volume in the Portable Ultrasound Scanning Device. Sysmex J, 36(1), 84–90, 2013 (in Japanese).
15) Saika T, et al.: Comparison of Bladder Volume Measurement Accuracy between Portable Ultrasound Diagnostic Equipment and CBCT for Pelvic Prostate Radiotherapy. Jpn J Radiol Technol, 80(7), 760–765, 2024 (in Japanese).
16) Mullaney L, et al.: A comparison of bladder volumes based on treatment planning CT and BladderScan® BVI 6100 ultrasound device in a prostate radiation therapy population. Br J Radiol, 91(1091), 20180160, 2018.
17) Shibata M, et al.: Usefulness of an Ultrasound System with Automatic Bladder Urine Volume Measurement Using Artificial Intelligence Technology in Radiotherapy. Jpn J Radiol Technol, 78(12), 1406–1414, 2022.
18) Y Kanda: Investigation of the freely available easy-to-use software 'EZR' for medical statistics. Bone Marrow Transplantation, 48, 452–458, 2013.

Received October 28, 2024; accepted April 19, 2025

Time-course temperature change of refrigerated phantoms during magnetic resonance imaging (MRI): Simulation for postmortem MRI setting

KOBAYASHI Tomoya[1, 2, 3)]*, SHIOTANI Seiji[4)], MURANAKA Hiroyuki[5)], NUMANO Tomokazu[2)], UEDA Takuya[6)], HAYAKAWA Hideyuki[7)], OKUDA Takahisa[3)]

1) Department of Diagnostic Imaging, Graduate School of Medicine, Tohoku University
2) Department of Radiological Sciences, Graduate School of Human Health Sciences, Tokyo Metropolitan University
3) Department of Legal Medicine, Nihon University School of Medicine
4) Department of Radiology, Seirei Fuji Hospital
5) Department of Health Sciences, School of Health Sciences, Nippon Bunri University
6) Department of Diagnostic Radiology, Graduate School of Medicine, Tohoku University
7) Department of Forensic Medicine, Tsukuba Medical Examiner's Office

* E-mail: t.kobayashi1001@gmail.com

Note: This paper is secondary publication, the first paper was published in the JART, vol. 72 no. 875: 25-34, 2025.

Key words: postmortem magnetic resonance imaging (MRI), phantom study, refrigerated corpse, radiofrequency heating, temperature

【Abstract】
Radiofrequency (RF) energy-induced heating effect of postmortem MRI is expected to be greater than that of clinical MRI, since physiological temperature control functions are absent in deceased bodies and total examination time tends to be longer. We used head and trunk phantoms kept in cold storage at 4℃ and a 1.5T MR scanner to simulate a refrigerated corpse being examined in a scan room where the ambient temperature is maintained at 23℃. Near surface temperature was measured at 4 points on the phantoms (the head and upper, middle, and lower parts of the trunk) every 5 minutes for 1 hour during scanning and 1 hour after scanning. Whole body average specific absorption rate (SAR) for 6 minutes was calculated in each applied sequence. At the baseline, the head phantom's temperature was lower than the trunk phantom. Though temperatures in all measured points were almost proportional to the time during measurement, the inclination on the temperature/time graph of the head phantom was greater than that of the trunk phantom. The coefficient of determination of the head phantom was 0.998. Meanwhile, the measured temperatures of the trunk phantom were higher than the linear function approximated using least squares method from 30 to 85 minutes after starting MRI. Mean whole body average SAR for 6 minutes was 1.34 ± 1.33 W/kg. RF energy-induced heating effect is expected to occur especially in the trunk of a refrigerated body due to high SAR and a long scanning time.

Introduction

Postmortem magnetic resonance imaging (PMMRI) has increasingly been utilized as a complementary diagnostic tool to postmortem computed tomography (PMCT) [1)], especially in cases where PMCT alone cannot adequately identify or diagnose specific conditions such as myocardial infarction, spinal cord injuries, and congenital abnormalities in pediatric cases [2-4)].

In magnetic resonance imaging (MRI) examinations, most of the radiofrequency (RF) energy is converted into heat within the patient and it is measured as the specific absorption rate (SAR), the power absorbed per mass of tissue (W/kg) [5)]. Rapidly alternating magnetic fields during RF exposure induce eddy currents within the patient's tissue according to Faraday's law of electromagnetic induction. This eddy current generates Joule heat which is proportional to the square of the current and the resistance. Due to the skin effect, eddy current density is highest near the surface, decreasing exponentially with greater depth [6,7)]. Consequently, RF energy-induced heating is more pronounced near the body surface, causing greater temperature elevations in superficial areas [8,9)]. Indeed, previous reports

have shown that RF exposure can increase surface temperatures of the living human body by an average of approximately 0.6℃, with increases of up to 2.1℃ in some cases [10].

RF energy-induced heating effect of PMMRI is expected to become stronger than that in clinical MRI, since physiological temperature control functions are absent in deceased bodies and the total time of whole-body PMMRI tends to be longer than that of MRI of a living patient in clinical settings. In fact, Kobayashi et al. reported that certain regions exhibited skin temperature increase of approximately 8℃ after whole body PMMRI of a refrigerated corpse [11]. This observation raises the possibility that even higher temperature elevations could occur during imaging, posing a risk of surface tissue damage.

A significant concern in PMMRI is thus the heating effect caused by RF exposure during the imaging process, as elevated tissue temperatures can potentially lead to surface tissue damage. To address these issues, it is necessary to capture and analyze temporal temperature changes occurring throughout the PMMRI procedure. Although prior studies have investigated temperature variations only before and after PMMRI of refrigerated cadavers [11], continuous temperature monitoring throughout the imaging process itself has not yet been reported.

The aim of this phantom study, therefore, was to simulate and evaluate the temporal temperature changes occurring during PMMRI of refrigerated cadavers, with a particular focus on assessing the potential risk of surface tissue damage. By providing a detailed analysis of these temperature variations, we aim to offer fundamental insights that will support safer implementation of PMMRI procedures.

Materials and Methods

Subjects

Referencing a trunk phantom of an American Society for Testing and Materials (ASTM), our experiments were performed using a self-made rectangular prism-shaped trunk phantom with dimensions of 308 mm (width: W) × 540 mm (length: L) × 200 mm (depth: D) surrounded by 12.5-mm-thick acrylic walls, and an oval-shaped head phantom including a nose in the center and a neck portion with dimensions of 178 mm (W) × 279 mm (L) × 265 mm (D) surrounded by a 3-mm-thick polypropylene wall (Fig. 1). The trunk phantom (26.6 kg) and the head phantom (5.6 kg) were securely adhered using a waterproof adhesive to ensure close contact. The phantoms were then filled with a sol which was prepared using 26.6 ℓ deionized water, 35.1 g of NaCl, and 266.1 g of polyacrylic acid (PAA). The prepared sol, which had a conductivity (σ) of 0.49 S/m and dielectric constant (ε) of 78 according to the procedures described in the ASTM standard [12], was infused into the head and trunk phantoms to a depth of 180 mm. Though we did not perform a degassing operation to eliminate air bubbles in the prepared sol, we visually confirmed the absence of air bubbles. In this study, we considered non-decomposed cadavers to have material

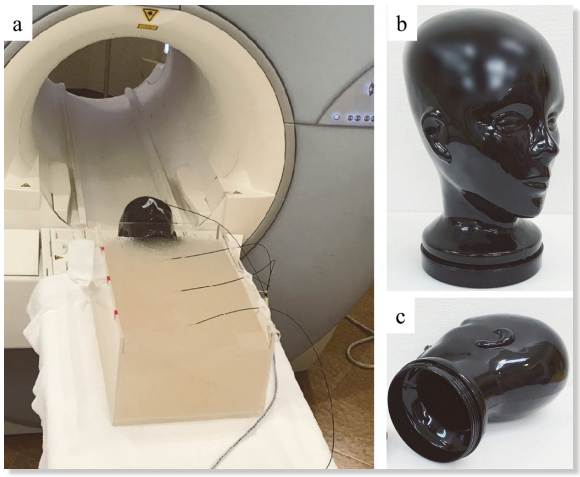

Fig. 1 Head and trunk phantoms and 4 fiber-optic thermometers

(a) Head and trunk phantoms placed in the MRI scanner, with 4 fiber-optic thermometers inserted into the trunk phantom for temperature measurement. (b,c) Close-up view of the black head phantom used in the study.

properties nearly equivalent to those of living bodies, as advanced decomposition is not typically observed in routine PMMRI. After having been kept in cold storage at 4℃ for 11 hours, a standard temperature widely used to maintain tissue flexibility and slow down tissue degradation in cadavers [13], MRI was performed on the head and trunk phantoms.

Measurement of temperature

We measured temperature of the phantoms using 4 fiber optic thermometers (FL2400-4ch, Anritsu Meter Co. Ltd., Tokyo, Japan) with an accuracy and resolution of 0.1℃. These thermometers were composed of optical fibers 10 meters in length and were not influenced by magnetic field or RF irradiation. The absolute values of the fiber optic temperature sensors were calibrated with a thermocouple thermometer. Temperatures at 4 points on the phantoms at a depth of 10 mm from the surface were measured to avoid the effects of evaporative heat loss (Figs. 1-3). This depth was chosen as it is sufficiently close to the surface to accurately reflect temperature changes influenced by RF energy, which are known to be greatest near the surface due to the skin effect, while simultaneously ensuring stable and consistent measurements. Exact locations of the 4 measured points were set as follows:

① Head phantom: At the central nose (a fiber optic thermometer was inserted into the prepared sol through a 10 mm-diameter hole created on the top of the surface).

② Upper part of the trunk phantom: At the point where the anterior midline of the phantom and the line at 150 mm caudal direction from the top of the phantom intersect.

③ Middle part of the trunk phantom: At the point where the anterior midline of the phantom and the line at 300 mm caudal direction from the top of the phantom intersect.

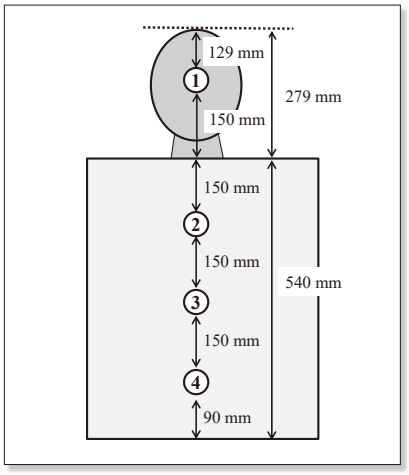

Fig. 2 Temperature measurement points on the phantoms

Four points set on the phantoms for near surface temperature measurement
① Head phantom
② Upper part of the trunk phantom
③ Middle part of the trunk phantom
④ Lower part of the trunk phantom

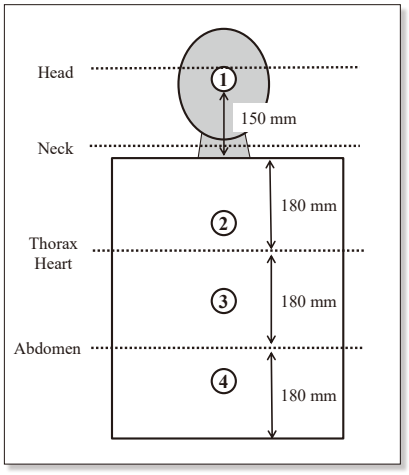

Fig. 3 Temperature measurement points and centers of the static magnetic field (B_0) for 4 scanned sites

Center of the static magnetic field for each part of the phantom
Head: One-third from the top of the head phantom excluding the neck
Neck: Middle of the neck
Thorax, Heart: One-third from the top of the trunk phantom
Abdomen: Two-thirds from the top of the trunk phantom
(①②③④ indicate the point of temperature measurement)

④ Lower part of the trunk phantom: At the point where the anterior midline of the phantom and the line at 450 mm caudal direction from the top of the phantom intersect.

In our study, the temperature measurement was conducted on the head and trunk phantoms without extremities (arms and legs) for the following reasons:

- The ASTM head and trunk phantom we referenced was designed without assuming its application for the extremities.
- Only four fiber optic temperature sensors were available for the experiment.
- Generally, lethal lesions exist in the head or trunk of a deceased body.

The temperature was measured every 5 minutes from immediately before starting the scan till 60 minutes after completion of scan to evaluate both the influence of the RF energy-induced heating effect and the ambient temperature.

Ambient conditions

The ambient temperatures of the magnetic bore and the scan room were maintained at 23.0℃ during the entire procedure. To measure near surface temperature distribution caused by RF energy-induced heating effect, the cooling fan of the MR unit was switched off.

MRI examination

MRI was performed using a 1.5T unit (Avanto, Siemens, Erlangen, Germany) with a built-in body coil. The phantoms were transported from the refrigerator to the MRI scanner within approximately 5 minutes, and scanning was initiated immediately. RF radiation from the transmission coil covered the area within an approximate 300 mm radius from the center of the static magnetic field (B_0). The scan table was positioned so that the center axis of the phantoms aligned with the center of the B_0 while scanning. For example, when scanning the head phantom, the scan table was adjusted so that the head phantom's center aligned with B_0. In our study, scanning was performed at 4 sites, where centers of B_0 were at one-third of the head, the center of the neck, one-third of the trunk, and two-thirds of the trunk (dotted lines in Fig. 3). The scan parameters we used are shown in Table 1 which were based on clinical parameters. These sequences are typically performed when conducting PMMRI in addition to postmortem CT at our institution, especially when performing whole-body MRI. The imaging was conducted in the order listed in Table 1, starting from the top. The controlled operating mode was used by setting the first-level controlled mode as the upper limit.

Measurement of whole-body average specific absorption rate (SAR)

Based on the information of DICOM (Digital Imaging and Communications in Medicine), the MRI system we used was capable of displaying "whole-body average SAR for 6 minutes" which was defined by the International Electrotechnical Commission (IEC) [14], and indicates how much energy is absorbed by the entire body during a 6-minute exposure period. With each MRI sequence we applied, whole-body average SAR was calculated by averaging the SAR for 6 minutes.

Statistical Analyses

On the graphs, temperatures (i.e. the dependent variable, y) at the 4 measured points on the phantoms were plotted at 5 minute-intervals during the 60-minute-scanning time and for 60 minutes after MRI (i.e. the independent variable, x). A linear regression of the relationship between temperature and time was calculated using the method of least squares [11]. The strength of the linear relationship between the two variables was quantified by calculating the correlation coefficient (r). SARs were shown as mean ± standard deviation. A repeated-measures analysis of variance (ANOVA) was performed to evaluate differences among the 4 measured points.

Table 1 Scan parameters of MRI used for head and trunk phantoms and their whole-body average SARs for 6 minutes

	Sequence	TR (ms)	TE (ms)	Thickness/ Gap (mm)	FOV (mm)	Time (min)	Whole-body average SAR for six minutes (W/Kg)
Head (axial)	T_2WI (TSE)	3200	88	6/1	220	1:47	0.23
	T_1WI (SE)	500	11	6/1	220	1:59	0.43
	PDWI (TSE)	2500	12	6/1	220	2:29	0.24
	T_2*WI (GE)	560	20	6/1	220	2:11	0.01
	Diffusion WI (EPI)	3300	106	6/1	220	1:04	0.05
	FLAIR (TSE)	9000	106	6/1	220	3:00	0.08
Neck (sagittal)	T_2WI (TSE)	3500	117	3/0.3	250	2:11	1.25
	T_1WI (TSE)	549	9.5	3/0.3	250	1:46	1.75
Heart (short axis)	Diffusion WI (EPI)	5000	117	4/0.4	220	3:47	0.51
	T_2WI (TSE)	5210	93	4/0.4	220	5:40	2.58
	T_2WI (3DTSE)	1200	100	1.2	200	6:09	0.20
Heart (4 chamber)	Diffusion WI (EPI)	5000	117	4/0.4	220	3:47	0.51
Thorax (coronal)	T_2WI (TSE)	3000	93	6/0.6	360	2:42	2.78
	T_1WI (GRE)	257	4.8	6/0.6	360	1:58	1.59
	STIR (TSE)	4970	65	6/0.6	360	2:29	3.86
Abdomen (coronal)	T_2WI (TSE)	3000	93	6/0.6	360	2:42	2.67
	T_1WI (GRE)	259	4.8	6/0.6	360	2:15	1.41
	STIR (TSE)	4970	65	6/0.6	360	2:29	4.00
						Total: 50:25	Average: 1.34

Abbreviations: 3D, 3-dimensional; EPI, echo planar imaging; FLAIR, fluid attenuated inversion recovery; FOV, field of view; GE, gradient echo; PD, proton density; SAR, specific absorption rate; SE, spin echo; STIR, short tau inversion recovery; TE, echo time; TR, repetition time; TSE, turbo spin echo; WI, weighted image

Statistical analysis was performed using Excel 2010 (Microsoft, Redmond, WA, USA) with the add-in software Statcel 2 (OMS publishing Inc, Tokorozawa, Saitama, Japan). A *p*-value of less than 0.05 was considered statistically significant. The correlation coefficient (*r*) was used to determine the strength of the correlation [15]: 0-0.19: very weak; 0.20-0.39: weak; 0.40-0.59: moderate; 0.60-0.79: strong; and 0.80-1.0: very strong.

Results

Setting the start time of MRI scan at 0 minutes, scanning of the head phantom (including the neck portion) finished at 26 minutes 22 seconds, the subsequent scanning of the trunk phantom started at 27 minutes 10 seconds, and finished at 61 minutes 34 seconds. The total MRI examination of 61 minutes 34 seconds contained the actual scanning time of 50 minutes 25 seconds, the time for positioning, and the time for tuning between each sequence (Table 1). Figs. 4-7 show temperature changes for 2 hours measured every 5 minutes from immediately before MRI, during MRI, and for 60 minutes after MRI.

The temporal temperature changes during postmortem MRI scans were observed to evaluate the effects of RF energy exposure. The graph presented below illustrates the following points:

- "Start of head scan (0 min)": This marks the initiation of RF energy exposure during the head scan.
- "Start of trunk scan (27 min 10 sec)": This indicates the transition from head scanning to trunk scanning.
- "End of all scans (61 min 34 sec)": This marks the conclusion of RF energy exposure at the end of all scans.

The repeated-measures ANOVA revealed statistically significant differences among the anatomical regions ($p < 0.0001$). Post-hoc examination indicated that the head phantom significantly differed from three trunk phantoms, showing distinctly lower measurement values. No significant differences were observed among the three trunk phantoms.

In the head phantom, the relationship between temperature and time was expressed with the following equation (Fig. 4):

$$Temp = 0.032\ Time + 10.13\ (r = 0.998;\ P = 2.172 \times 10^{-29}) \quad \cdots\cdots\cdots (1)$$

, where *Temp* stands for temperature and r stands for the coefficient of determination (the same applies to the following formulas).

The temperature of the head phantom was 10.1℃ immediately before MRI, and 13.9℃ (the highest during the measurement) at 120 minutes after the start of MRI.

In the upper part of the trunk phantom, the relationship between temperature and time was expressed with the following equation (Fig. 5):

$$Temp = 0.018\ Time + 15.84\ (r = 0.896;\ P = 1.447 \times 10^{-9}) \quad \cdots\cdots\cdots (2)$$

The temperature of the upper part of the trunk phantom was 15.5℃ immediately before MRI and 17.5℃ at 120 minutes after the start of MRI. The highest temperature during the 120-minute measurement was 17.6℃ at 115 minutes after the start of MRI. From 35 to 80 minutes after the start of MRI, the temperature of the upper trunk was higher than the approximated line created by the least squared method, with the maximum of 0.6℃ higher at 50 minutes.

In the middle part of the trunk phantom, the relationship between temperature and time was expressed with the following equation (Fig. 6):

$$Temp = 0.009\ Time + 16.24\ (r = 0.603;\ P = 1.411 \times 10^{-3}) \quad \cdots\cdots\cdots (3)$$

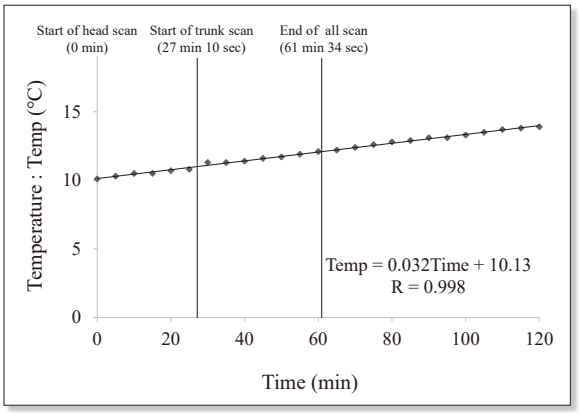

Fig. 4 Temperature of the head phantom measured at every 5 minutes

The solid line represents linear approximation.

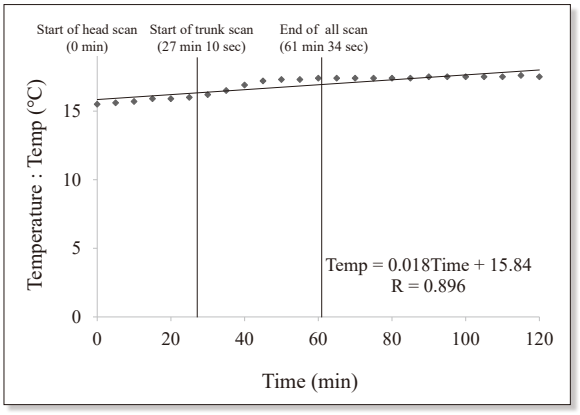

Fig. 5 Temperature of the upper trunk phantom measured at every 5 minutes

The solid line represents linear approximation.

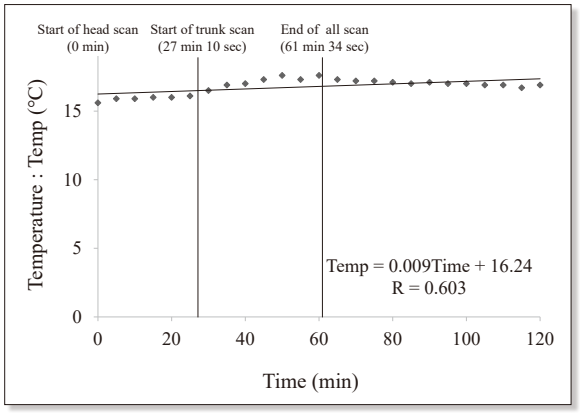

Fig. 6 Temperature of the middle trunk phantom measured at every 5 minutes

The solid line represents linear approximation.

The temperature of the middle part of the trunk phantom was 15.6℃ immediately before MRI, and 16.9℃ at 120 minutes after the start of MRI. The highest temperature during the120-minute measurement was 17.6℃ at 50 and 60 minutes after the start of MRI. From 30 to 80 minutes after the start of MRI, the temperature of the middle part of the trunk phantom was higher than the approximated line created by the least squared method, with the maximum of 0.9℃ higher at 50 minutes.

In the lower part of the trunk phantom, the relationship between temperature and time was expressed with the following equation (Fig. 7):

$$Temp = 0.014\ Time + 16.01\ (r = 0.809;\ P = 1.701 \times 10^{-6}) \quad \cdots\cdots\cdots (4)$$

The temperature of the lower part of the trunk phantom was 15.5℃ immediately before MRI, and 17.2℃ at 120 minutes after the start of MRI. The highest temperature during the 120-minute measurement was 17.4℃ at 55, 65, 70, and 75 minutes after the start of MRI. From 35 to 85 minutes after the start of MRI, the temperature of the lower portion of the trunk was higher than the approximated line created by the least squared method, with the maximum of 0.6℃ higher at 55 minutes.

Whole body average SAR for 6 minutes ranged from 0.01 to 4.00 (1.34 ± 1.33) W/kg depending on the scanned part of the phantoms (Table 1).

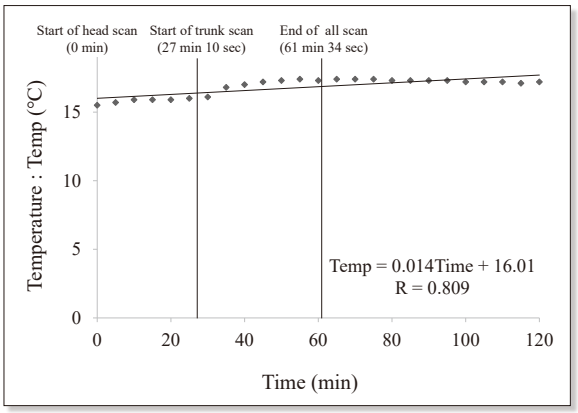

Fig. 7 Temperature of the lower trunk phantom measured at every 5 minutes
The solid line represents linear approximation.

Discussion

In our study, near surface temperatures in all measured points in the phantoms were almost proportional to the time throughout the measurement. However, the following 4 differences were noted between the results of the head phantom and the trunk phantom:

1) Immediately before MRI, the temperature of the head phantom (10.1℃) was lower than that of the trunk phantom's upper (15.5℃), middle (15.6℃), and lower (15.5℃) parts.
2) Inclination of the linear graph of the head phantom (0.032) was greater than that of the trunk phantom's upper (0.018), middle (0.009), and lower (0.014) parts.
3) The coefficient of determination (r) of the trunk phantom's upper (0.896), middle (0.603), and lower (0.809) parts was less than that of the head phantom (0.998).
4) The temperature of the trunk phantom was slightly higher than the line approximated by the least square method from 30 to 85 minutes after the start of MRI.

The phenomenon of the above-mentioned 1) and 2) can be explained by the surface-to-volume ratio (= the amount of surface area per unit volume). The larger the surface-to-volume ratio of an object, the more heat gain and loss occurs through the surface area. Generally, if the volume of an object is small, the surface-to-volume ratio increases; thus, it is easily affected by ambient temperature [16]. Since the volume of the head phantom was smaller than that of the trunk phantom, the head phantom was considered more susceptible to ambient temperature. Therefore, after keeping the phantoms in cold storage at 4℃ for 11 hours, the temperature of the head phantom before MRI was lower than that of the trunk phantom, and the subsequent

temperature increase after having been moved out of the cold storage was considered greater. Similarly, Barton et al. measured surface temperature change of a corpse in the head, chest, and abdomen after taking the corpse out of refrigerated storage at 4℃, and reported that the head portion was more susceptible to ambient temperature change [17]. Additionally, in this study, the head phantom is surrounded by a 3 mm thick polypropylene wall, while the trunk phantom has a 12.5 mm thick acryl wall. This difference in thickness and material of the wall may have resulted in the head phantom having a higher thermal conductivity and experiencing more rapid temperature changes. Moreover, although the baseline temperature of both head and trunk phantoms did not exactly reach 4℃ despite the extended refrigeration period, the trunk phantom demonstrated nearly identical start temperatures and consistent temporal temperature changes across different measurement points. This indicates minimal inconsistencies in refrigeration conditions, suggesting that any potential non-uniformity in thermal equilibrium within the phantoms likely had negligible effects on the study outcomes.

The phenomenon of the above-mentioned 3) and 4) can be explained by SAR. In this study, the mean whole body average SAR of the phantoms was 1.34 W/kg and SAR of the head phantom was lower than the mean in each applied sequence. Furthermore, RF irradiation was considered not to have affected the head phantom during imaging of the trunk, because the distance from the measured point on the head phantom (① on Fig. 2) to the center of B_0 for the thorax and the heart site (Fig. 3) was 330 mm (150 + 180 mm), exceeding the RF radiation range (300 mm radius from the B_0 center). Consequently, the head phantom's temperature consistently increased at a stable rate due to ambient room temperature. In contrast, temperature increases observed in regions exposed to RF radiation were distinctly different during the respective imaging times. These differences in temperature behavior support the conclusion that observed temperature variations during imaging periods are primarily attributable to RF radiation exposure. Whereas, for the trunk phantom, 7 SARs of 10 imaging sequences were higher than the mean, and the examination time for the trunk phantom (33 minutes 58 seconds) was longer than for the head phantom (16 minutes 27 seconds). This difference can be attributed to the larger size of the trunk phantom, which affects the specific absorption rate (SAR). According to the equation $SAR = C\sigma r^2 Bo^2 \alpha^2 D$ (where C is a proportional constant, σ is the electrical conductivity, r is the effective radius, Bo is the magnetic field strength, α is the flip angle, and D is the duty cycle), SAR increases proportionally to the square of the radius (r^2) [18]. The larger size of the trunk phantom results in higher SAR values due to its greater interaction with the RF field. The temperature observed in the trunk phantom between the "Start of trunk scan" and the "End of all scan" was slightly higher temperatures than the graph line approximated by the least squared method (Fig. 5-7), which was different from linearly increased head phantom's temperature (Fig. 4). This suggests that the trunk phantom's temperature increase was affected not only by the temperature of the room but also by SAR, or the RF energy emitted during the imaging process, as it showed a similar trend at all three measurement points in the trunk phantom. Sustained RF exposure was confirmed to cause significant and consistent temperature increases. In contrast, if the phantoms were kept at room temperature without RF exposure, no transient or pronounced temperature changes would be expected.

Our study has three limitations. First, we did not measure control data without RF irradiation. To accurately assess this effect, the phantom should be cooled again with its

temperature measured in the MR room over the same time period, but without initiating an MRI scan. This experiment was not conducted due to the necessity of minimizing the time the equipment was occupied for clinical patient imaging, a limitation further exacerbated by institutional policies related to COVID-19. The original experiment was conducted in approximately 2020, during which the impact of COVID-19 precluded the possibility of performing control experiments. At present, relocation to a new facility has rendered the reproduction of the original experimental conditions impractical, further constraining our ability to conduct control experiments. Thus, we could not verify the extent of temperature increase due to the temperature of the room alone. Second, the phantom used in this study is homogeneous, which does not fully replicate the heterogeneous conditions of a human body. Therefore, the exact phenomena observed in this study may not be entirely reproducible in a real human body. Third, temperature measurements in this study were conducted at a depth of 1 cm to minimize evaporative cooling effects and ensure measurement stability. However, temperature changes at both surface and deeper tissue regions should also be evaluated to fully understand RF-induced heating effects. Additionally, the trunk phantom thickness used (180 mm) was thinner than typical human torso thicknesses (approximately 200–300 mm) due to structural constraints of the phantom container. Previous studies have reported postmortem changes in dielectric and conductivity properties, potentially increasing SAR by about 10% [19-21], which cannot be replicated in phantoms. Future studies should address these limitations by measuring temperatures at multiple depths, using phantoms more representative of actual human anatomy, and considering postmortem tissue property changes.

In conclusion, the RF energy-induced heating during PMMRI primarily affected superficial regions, consistent with known RF absorption patterns. The magnitude of temperature rise observed was modest. Consequently, the potential risk of surface tissue damage due to RF heating appears minimal. Nonetheless, considering the inherent differences between the phantom and actual postmortem conditions, these results should be interpreted with caution, and further in-vivo investigations may still be warranted to confirm the clinical safety implications of RF-induced temperature variations during PMMRI.

Conflict of interest

The authors declare no conflict of interest.

References

1) Horsfall I., et al.: Forensic imaging: Developing applications of computed tomography and magnetic resonance imaging. Forensic Sci Med Pathol, 16(3), 477-489, 2020.
2) Jackowski C., et al.: Virtopsy: postmortem imaging of the human heart in situ using MSCT and MRI. Forensic Sci Int, 149(1), 11-23, 2005.
3) Okuda T., et al.: A case of fatal cervical discoligamentous hyperextension injury without fracture: Correlation of postmortem imaging and autopsy findings. Forensic Sci. Int, 225(1-3), 71-74, 2013.
4) Thayyil S., et al.: Post-mortem MRI versus conventional autopsy in fetuses and children: a prospective validation study. The Lancet, 382(9888), 223-233, 2013.
5) Brix G., et al.: Sampling and evaluation of specific absorption rates during patient examinations performed on 1.5-Tesla MR systems. Magnetic resonance imaging, 19, 6, 769-79, 2001.
6) Shellock, F.G., et al.: Thermal effects of high-field (1.5 tesla) magnetic resonance imaging of the spine. Clinical experience above a specific absorption rate of 0.4 W/kg. Acta radiologica Supplementum, 369, 514-6, 1986.
7) Shellock, F.G.: Radiofrequency energy-induced heating during MR procedures: a review. J Magn Reson Imaging, 12(1), 30-6, 2000.
8) Shellock, F.G., et al.: Temperature, heart rate, and blood pressure changes associated with clinical MR imaging at 1.5 T. Radiology, 163, 259-262, 1987.

9) Tang, M., et al.: Progress in understanding radiofrequency heating and burn injuries for safer MR imaging. Magn Reson Med Sci, 22, 7-25, 2023.
10) Shellock, F.G., et al.: Temperature changes caused by MRI of the brain with a head coil. AJNR, 9, 287-291, 1988.
11) Kobayashi, T., et al.: Skin temperature increase after whole body postmortem magnetic resonance imaging. Forensic Imaging, 200405, 2020.
12) ASTM F2182-09: Standard test method for measurement of radio frequency induced heating on or near passive implants during magnetic resonance imaging. West Conshohocken, PA: ASTM International, 2009.
13) Zhang, J., et al.: Effects of tissue preservation temperature on high strain-rate material properties of brain. J Biomech, 44(3), 391-396, 2011.
14) International Electrotechnical Commission (IEC): Medical electrical equipment, part 2: particular requirements for the basic safety and essential performance of magnetic resonance equipment for medical diagnosis. IEC, 60601-2-33, 2010.
15) Sedgwick, P.: Pearson's correlation coefficient. British Medical Journal, 345, 41-56, 2012.
16) Planinsic, G., et al.: The surface-to-volume ratio in thermal physics: from cheese cube physics to animal metabolism. Eur J Phys, 29, 369-384, 2008.
17) Barton, P.S., et al.: Temperature dynamics in different body regions of decomposing vertebrate remains. Forensic Sci Int, 110900, 2021.
18) Röschmann, P.: Radiofrequency Penetration and Absorption in the Human Body: Limitations to High-Field Whole-Body Nuclear Magnetic Resonance Imaging. Medical Physics, 14(6), 922-931, 1987.
19) WANG, Lei., et al.: Dielectric properties of human active liver, kidney and spleen compared to those of respective inactive tissues, porcine tissues and the data provided by a database in the frequency range of 10 Hz to 100 MHz. IEEE trans biomed eng, 68(10), 3098-3109, 2021.
20) CANTÜRK, Ismail., et al.: An experimental evaluation of electrical skin conductivity changes in postmortem interval and its assessment for time of death estimation. Comput Biol Med, 69, 92-96, 2016.
21) Schmid, G., et al.: Dielectric properties of human brain tissue measured less than 10 h postmortem at frequencies from 800 to 2450 MHz. Bioelectromagnetics, 24(6), 423-30, 2003.

Received September 30, 2024; accepted June 17, 2025

Perceptions of Radiological Technologists on Their Interaction with Children: Preliminary Research for a Preparation Program

MORINO Tomomi[1)]*, SAWA Moena[1)], OHASHI Miku[2)], SHIROSAKI Nobuyuki[1)]

1) Department of Radiology, Toyama University Hospital
2) Pediatrics, Toyama University Hospital

* E-mail: maiwa910@med.u-toyama.ac.jp

Note: This paper is secondary publication, the first paper was published in the JART, vol. 72 no. 878: 28-36, 2025.

Key words: preparation, children, radiological technologist, questionnaire, child life specialist

【Abstract】
Purpose: This preliminary study investigated radiological technologists' perceptions of their interactions with children undergoing radiological examinations and treatments to identify current problems and potential challenges.
Methods: The study included 40 radiological technologists at our hospital who were involved in pediatric examinations and treatments. Data were collected through a questionnaire survey and analyzed.
Results: More than half of the respondents reported a lack of confidence in interacting with children. The findings indicated that technologists at our hospital lack sufficient knowledge and skills related to pediatric care.
Conclusion: Improving pediatric care requires the implementation of training programs that enable staff to acquire the necessary knowledge and skills. Furthermore, organizational efforts to establish a supportive environment for preparation within each modality are needed to facilitate the delivery of higher-quality radiological examinations and treatments for children and their families.

Introduction

Radiological examinations and treatments are indispensable for the diagnosis and management of diseases. However, in pediatric medical settings, some procedures cannot be performed because of children's heightened anxiety, or re-examinations are required when images are difficult to interpret.

In recent years, "preparation" has been introduced and is rapidly expanding in pediatric medicine. Preparation refers to the practice of providing children with information about upcoming medical events in a developmentally appropriate and easily understandable manner, thereby supporting their psychological readiness [1)].

The number of facilities implementing preparation for radiological examinations and treatments is increasing. Using teaching materials such as models, dolls, and pamphlets to help children visualize the procedure, or allowing them to visit the examination room in advance, helps children to develop coping strategies that suit them and undergo examinations more smoothly with a positive outlook [1-4)]. Furthermore, environmental modifications—such as the use of music or video projections to distract children—have been effective [5, 6)]. In radiotherapy (RT), multidisciplinary efforts to create child-friendly treatment environments have also been described, including the use of immobilization devices for dolls and simulated treatment experiences tailored to individual children [7, 8)].

Preparation serves multiple roles and yields various benefits. Psychologically, it can reduce fear and distress, prevent traumatic experiences, and support healthy mental development by enhancing children's sense of accomplishment and self-esteem through supportive interactions [2)]. From a safety perspective, prepara-

tion may help prevent falls and enable examinations without sedation, thereby reducing unnecessary sedative use and the risk of associated side effects. It may also shorten examination time required and decrease radiation exposure resulting from repeat imaging [9-12]. Furthermore, the involvement of child life specialists (CLS) or hospital play specialists has been reported to reduce the number of children requiring sedation [13]. A key characteristic of diagnostic imaging is that it typically does not involve significant pain; therefore, many children can successfully undergo procedures when appropriate preparation and supportive environments are provided [8].

Currently, research on preparation methods conducted by nurses and CLS is active, but relatively few studies have focused on preparation for radiological examinations and treatments [2]. Although one study examined radiological technologists' perceptions of preparation through semi-structured interviews with five radiological technologists, conducted to understand multidisciplinary collaboration from a nursing perspective [14], the current challenges and intervention techniques (non-technical skills) required for radiological technologists to actively implement preparation in clinical settings—particularly through collaboration with CLS—have not been sufficiently clarified. Consequently, there remains room to improve how radiological technologists support pediatric patients.

At our hospital, a CLS has been assigned to the pediatrics department since 2007. The CLS is a professional who provides psychosocial support to children and families in medical settings. Drawing on knowledge of child developmental psychology and the impact of medical care on children and families, the CLS uses various methods, including preparation, to help children take an active role in their medical experiences. Through collaboration between radiological technologists—who interact directly with children during procedures—and the CLS, it is possible to develop support strategies from a child-centered perspective and establish a more effective system for pediatric radiological examinations and treatments.

In this study we aimed to investigate the current status of radiological technologists' knowledge of preparation and their interactions with children undergoing radiological examinations and treatments to clarify current issues and identify future challenges in implementing preparation within the radiology department of our hospital in collaboration with the CLS.

Definition of Preparation

In this study, preparation was defined as reducing the fear and anxiety experienced by children undergoing examinations or treatments. It refers to supporting children's psychological readiness by explaining, in a developmentally appropriate and easy-to-understand manner, what they will experience and by creating an environment that promotes the child's coping abilities. Preparation is also regarded as a form of care that protects children's rights from the child's perspective [1, 2].

1. Methods

1-1 Survey Method

The study participants were 40 radiological technologists at our hospital who were involved in pediatric radiology examinations and treatments. A web-based questionnaire survey was conducted using Google Forms. The questionnaire included both multiple-choice and open-ended questions. The survey period was from July 1 to August 31, 2023.

1-2 Survey Contents

1-2-1 Participant Characteristics

The questionnaire collected information on participant characteristics, including gender, parenting experience, years of clinical experience, and clinical departments in which par-

ticipants had experience interacting with children.

1-2-2 Interaction with Children

Q1. How confident do you feel about interacting with children during examinations and treatments?
Choices: Not confident at all / Not very confident / Neutral / Fairly confident / Very confident

Q2. Have you ever experienced difficulty interacting with children during examinations and treatments?
Choices: Yes / No

Q3. At which developmental stages do you find it difficult to interact with children during examinations and treatments? (Multiple answers allowed)
Choices: Infancy (0 to < 1 year) / Toddlerhood and Preschool age (1 year to before elementary school, approximately 6 years) / School age (elementary school, up to 6th grade; approximately 12 years) / Adolescence (junior high school to approximately 18 years)

Q4. What types of difficulties did you experience at the developmental stages where interaction was difficult? Please select all applicable factors. (Multiple answers allowed)
Choices: Movement / Crying / Lack of Communication / Family Interaction / Other

Q5. What type of difficulties did you experience in each imaging modality? Please select all applicable factors. (Multiple answers allowed)
Choices: Movement / Crying / Lack of Communication / Family Interaction / Other

Q6. How did you cope with the difficulties encountered in each modality? Please select the coping strategies used. (Multiple answers allowed)
Choices: Sedation / Restraint / Obtaining cooperation from family members / Adjusting to the child's timing / Distraction / Providing thorough explanations to the child / Listening to the child's wishes / Other

1-2-3 Knowledge and Interest in Preparation

Q7. Are you familiar with the term "preparation?"
Choices: Yes / No

Q8. After reading the definition of preparation, do you think preparation is necessary for examinations and treatments in the radiology department?
Choices: Necessary / Somewhat necessary / Neither / Not very necessary / Not necessary at all

Q9. Do you think that the environment for pediatric examinations and treatments would be improved by understanding pediatric psychology and examination responses at each developmental stage through training sessions, and by implementing preparation?
Choices: Improved / Somewhat improved / Neither / Somewhat worsened / Worsened

Q10. If training sessions on preparation are offered, would you like to participate?
Choices: I want to participate / I don't want to participate

1-3 Statistical Analysis

Statistical analysis was performed using EZR version 1.68. To examine the relationship between confidence in interacting with children (measured on a 5-point scale: 1 = "Not confident at all" to 5 = "Very confident") and participant characteristics (gender, parenting experience, and years of clinical experience), cross-tabulation analysis was performed. Data are presented as mean ± standard deviation (SD). The Mann–Whitney *U* test was used to compare gender and parenting experience, while the Kruskal–Wallis test and Spearman's rank

correlation coefficient were used to analyze years of clinical experience. A p-value of <0.05 was considered statistically significant.

1-4 Ethical Considerations

Participation in the survey was voluntary, and participants were assured that they would not experience any disadvantage by choosing not to participate. The questionnaire was anonymous, and to protect personal information, all data were statistically processed to ensure that no individuals could be identified. Participants were informed that the data would be used solely for this study. Informed consent was obtained through a consent field in the questionnaire, where participants indicated their willingness to participate. This study was approved by the Clinical Research and Ethics Center of our hospital (Approval No. R2023080).

2. Results

2-1 Participants Characteristics

Table 1 summarizes participants' characteristics. Of the 40 radiological technologists targeted for the study at our hospital, 35 responded (response rate: 87.5%). Of these, 25 were male (71.4%), and 10 were female (28.6%). Regarding parenting experience, 19 respondents (54.3%) had no parenting experience, whereas 16 (45.7%) had parenting experience.

Regarding years of clinical experience, four respondents (11.4%) had < 3 years of clinical experience, six (17.1%) had 3–5 years, four (11.4%) had 6–9 years, 13 (37.1%) had 10–14 years, four (11.4%) had 15–19 years, and four (11.4%) had ≥ 20 years. Overall, 77.0% of respondents had < 15 years of clinical experience. The clinical departments (modalities) where the respondents had experience interacting with children were as follows: radiography (33 respondents, 94.3%), computed tomography (CT; 30, 85.7%), magnetic resonance imaging (MRI; 14, 40.0%), radioisotope imaging (RI; 7, 20.0%), radiotherapy (RT; 14, 40.0%), and interventional radiology (IVR; 12, 34.3%).

2-2 Interaction with Children during Examinations and Treatments

Fig. 1 shows the responses to Q1 regarding

Table 1 Characteristics of the study participants.

n = 35

Subject Attributes	Choices	Number of people	Ratio (%)
Occupation	Radiological technologist	35	100.0
Gender	Male	25	71.4
	Female	10	28.6
Parenting experience	No	19	54.3
	Yes	16	45.7
Years of clinical experience	< 3 years	4	11.4
	3-5 years	6	17.1
	6-9 years	4	11.4
	10-14 years	13	37.1
	15-19 years	4	11.4
	≥20 years	4	11.4
Department of experience	Radiography	33	94.3
	CT	30	85.7
	MRI	14	40.0
	Radioisotope	7	20.0
	Radiotherapy	14	40.0
	Interventional radiology	12	34.3

the impressions of interacting with children during examinations and treatments. Among the respondents, 51.5% (n = 18) reported being "Not confident at all" or "Not very confident," 40% (n = 14) reported "Neutral," and 8.6% (n = 3) reported being "Fairly confident" or "Very confident." These findings indicate that more than half of the radiological technologists reported difficulty in interacting with children.

Figs. 2a–f present the relationships between impressions of interacting with children and participants' characteristics (gender, parenting experience, and years of clinical experience). Statistical analysis revealed no significant differences based on gender or parenting experience (p = 0.160 and 0.903, respectively). Similarly, no significant correlation was observed between impressions and years of clinical experience (p = 0.168, r = 0.248). The mean ± SD impression score for all respondents was 2.37 ± 1.01, which was below the median value of 3 on the evaluation scale. Table 2 presents the detailed results.

Fig. 3 shows the responses to Q2 regarding whether respondents had experienced difficulties when interacting with children during examinations and treatments. The results indicated that 94.2% (n = 33) had experienced such difficulties.

Fig. 4a presents the developmental stages at which respondents perceived interactions with children to be difficult (Q3). The proportions were 77.1% (n = 27) for infancy, 88.6% (n = 31) for the toddler/preschool stage, 45.7% (n = 16) for school age, and 5.7% (n = 2) for adolescence. These findings suggest that interactions were perceived as particularly challenging during infancy and the toddler/preschool stage.

Fig. 4b shows the factors contributing to interaction difficulties at each developmental stage (Q4). "Movement" was the most frequently reported factor across all developmental stages. For infancy and the toddler/preschool stage, the factors generally decreased in the following order: "Movement," "Crying," "Lack of Communication," and "Family Interaction." In the school-age stage, although "Crying" was less frequently reported, the overall pattern of factors was similar to that observed in infancy and toddlerhood.

Fig. 5a presents the factors contributing to difficulties categorized by modality (Q5). "Movement" was the most frequently reported factor across all modalities except for IVR. Other factors decreased in the following order: "Crying," "Lack of Communication," and "Family Interaction."

Fig. 5b illustrates the coping strategies used to address these difficulties, categorized by modality (Q6). In modalities with relatively long examination times (MRI, RI, RT, and IVR), "Sedation" was the most common strategy, reported in more than 80% of responses. In contrast, in modalities with shorter examination times (general radiography and CT), the use of "Sedation" was lower, whereas "Restraint" was used in over 80% of cases. Specifically, in general radiography, "Sedation" accounted for fewer than 10%, whereas "Family Cooperation" was the most common strategy (>90%), followed by "Child's Timing" (~70%). In CT examinations, both "Child's Timing" and "Sedation" were reported in approximately 50% of cases. Across all modalities, the use of "Distraction," "Explanation to children," and "Child's Wishes" remained relatively low.

2-3 Knowledge of and Interest in Preparation

Fig. 6a shows respondents' awareness of the term "preparation" (Q7). The results indicated that 37.1% (n = 13) were familiar with the term, whereas 62.9% (n = 22) were not.

Fig. 6b illustrates the perceived necessity of preparation after its definition was provided (Q8). All respondents (100%) selected either "necessary" or "somewhat necessary," indicating recognition of the importance of preparation.

Fig. 6c presents respondents' views on environmental improvement through the imple-

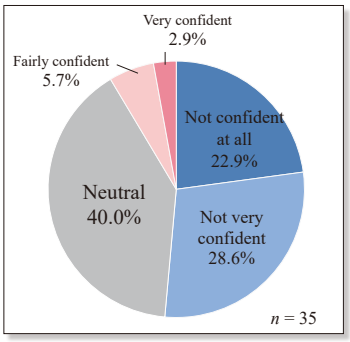

Fig. 1 Impressions of interacting with children during examinations and treatments.

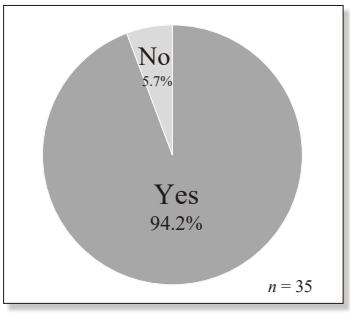

Fig. 3 Experience of difficulties when interacting with children during examinations and treatments.

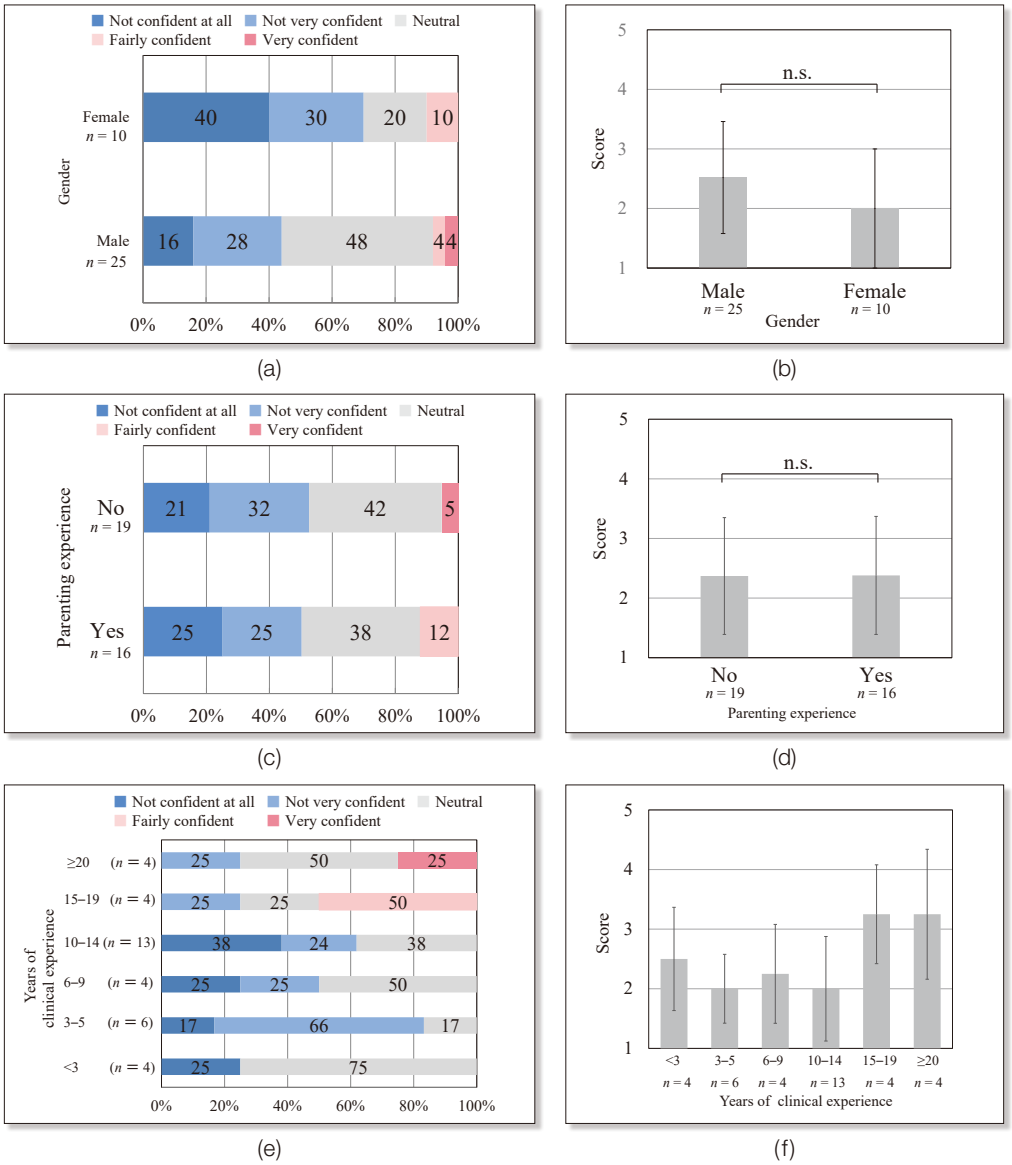

Fig. 2 Relationship between confidence levels and participant characteristics.

(a) Response proportions by gender.
(b) Relationship between average confidence score and gender.
(c) Response proportions by parenting experience.
(d) Relationship between average confidence score and parenting experience.
(e) Response proportions by years of clinical experience.
(f) Relationship between average confidence score and years of clinical experience.
* For (b), (d), and (f), responses to Question 1 on a five-point scale (1: not confident at all, 2: not very confident, 3: neutral, 4: fairly confident, 5: very confident) was converted into numerical values (1–5) and compared using statistical tests (significance level: $p < 0.05$).

Table 2 Analysis of the relationship between perceived difficulties and participant characteristics.

n = 35

Demographics	Choices	Average	Standard deviation	P-valus	Correlation coefficient
Occupation	Radiological technologist	2.37	1.01	–	–
Gender	Male	2.52	0.94	0.160	–
	Female	2.00	1.00		
Parenting experience	No	2.37	0.98	0.903	–
	Yes	2.38	0.99		
Years of clinical experience	< 3 years	2.50	0.87	0.168	0.248
	3-5 years	2.00	0.57		
	6-9 years	2.25	0.83		
	10-14 years	2.00	0.88		
	15-19 years	3.25	0.83		
	≥20 years	3.25	1.09		

Statistical significance: p<0.05.

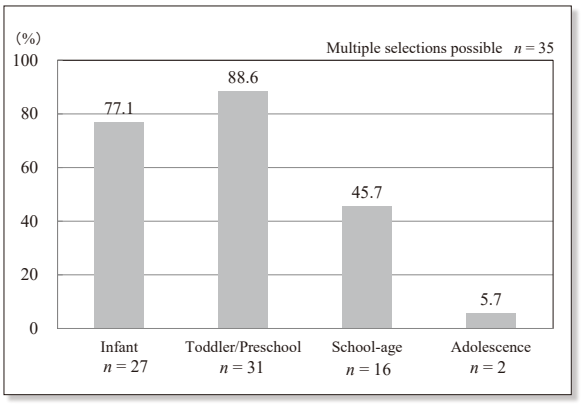

(a)

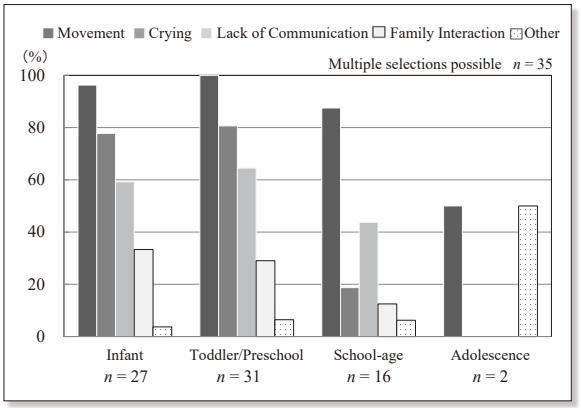

(b)

Fig. 4 Relationship between perceived difficulty and child developmental stages.

(a) Developmental stages perceived as difficult to interact with.
(b) Factors contributing to perceived difficulty by developmental stage.

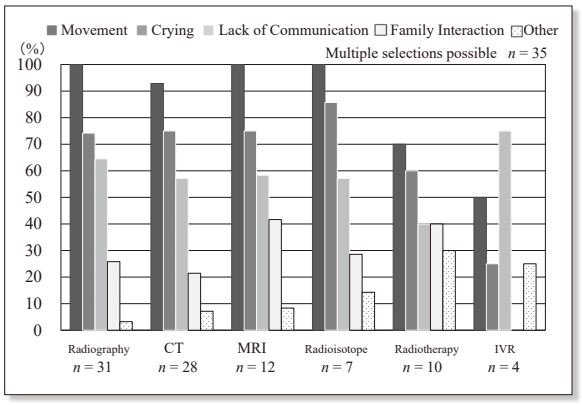

(a)

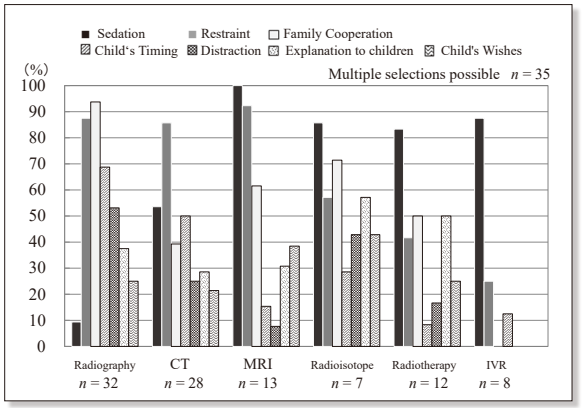

(b)

Fig. 5 Relationship between perceived difficulty and modality.

(a) Factors contributing to difficulty by modality.
(b) Coping strategies for these factors by modality.

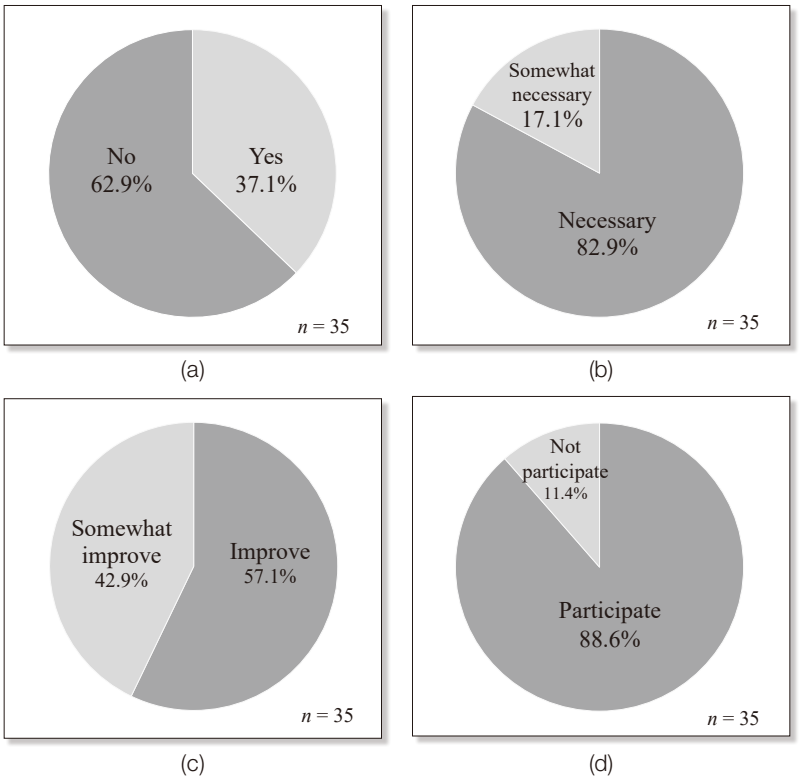

Fig. 6 Knowledge of and interest in preparation.

(a) Level of awareness.
(b) Perceived necessity (after providing the definition of preparation).
(c) Perceptions of environmental improvement following the implementation of preparation.
(d) Willingness to participate in training sessions.

mentation of preparation (Q9). All respondents selected either "improved" or "somewhat improved," suggesting a consensus that introducing preparation would contribute to improving the pediatric examination environment.

Fig. 6d shows willingness to participate in training sessions related to preparation (Q10). A total of 88.6% (n = 31) indicated that they would like to participate, whereas 11.4% (n = 4) indicated that they would not.

3. Discussion

3-1 Interaction with Children during Examinations and Treatments

More than half of the radiological technologists reported low confidence ("not confident at all" or "not very confident") in interacting with children. The mean confidence score (2.37 ± 1.01) was below the median value of 3, indicating an overall tendency toward low confidence. This lack of confidence was observed regardless of participant characteristics such as gender, parenting experience, or years of clinical experience. As reported by Takemoto et al. [15], this may be attributable to the fact that developmental and infant psychology are not mandatory components of radiological technologist training curriculum. Although there are numerous opportunities to learn technical skills related to examinations and treatments, opportunities to acquire non-technical skills—such as effective communication with children—are limited. This lack of educational opportunities during foundational training is likely a major contributor to the perceived difficulty and lack of confidence. At our hospital, patient information is shared among technologists during examinations; however, opportunities to discuss effective interaction

strategies are limited. As suggested by Kato et al. [14], this situation indicates that the quality of interactions largely depends on individual awareness and personal experience.

Regarding difficulties, over 90% of respondents reported having encountered challenges when interacting with children. In addition to the aforementioned lack of confidence and training, environmental factors in examination rooms likely contribute substantially. Children's anxiety often arises from the "fear of unfamiliar and tense environments" and the "fear of the unknown." Environments characterized by large machines in dark rooms, separation from parents for radiation protection, and the requirement to remain still can impose considerable anxiety and fear on children [15]. Consequently, radiological technologists frequently encounter resistance or confusion from pediatric patients, which contributes to the high prevalence of reported difficulties.

Difficulties were most pronounced during infancy and the toddler/preschool stages (over 70%), with "Movement" and "Crying" identified as the primary factors (over 70%). Furthermore, "Lack of Communication" was reported by over 50% of respondents. Since infants, toddlers, and preschoolers have difficulty understanding procedures and cooperating with instructions, the resulting "Movement" becomes a significant hurdle for technologists. Given that children's abilities and needs vary by developmental stage, learning age-appropriate interaction strategies is essential.

Factor trends by modality were generally consistent with those observed across developmental stage (except for IVR), with "Movement," "Crying," "Lack of Communication," and "Family Interaction" appearing in descending order. These findings suggest that "Movement" is the primary factor affecting the quality of pediatric radiological diagnosis and treatment. In diagnostic imaging, movement can cause motion artifacts or inadequate breath-holding, thereby reducing diagnostic accuracy. In RT, patient movement reduces positioning accuracy and may contribute to late complications that affect long-term quality of life [16]. The unique trend observed in IVR may reflect its specialized environment, where a multidisciplinary team (including physicians, nurses, and technologists) works collaboratively and frequently utilizes sedation to ensure procedural success.

Coping strategies varied by modality. In modalities with longer examination times (MRI, RI, RT, and IVR), sedation was used in more than 80% of cases because prolonged immobilization is required. In contrast, sedation rates were low in shorter procedures (radiography and CT), whereas "Restraint" and "Child's Timing" were frequently used. This likely reflects the use of pediatric immobilization devices or the practice of performing scans during moments when the child is naturally still. The relatively high use of "Family Cooperation" in general radiography suggests that family involvement is considered a simple and effective strategy. In CT, "Child's Timing" and "Sedation" were each reported in approximately 50% of cases, indicating that the chosen approach often depends on the patient's condition and the potential use of contrast media. Notably, "Distraction," "Explanation to children," and "Child's Wishes" were reported at low rates across all modalities. This likely reflects limited confidence and skills related to developmental-stage–appropriate communication. Because sedation is invasive and requires strict safety monitoring [9], preparation—reported to increase the success rate of non-sedated examinations—is expected to be an effective alternative [9-12]. Furthermore, reducing repeat scans is particularly important for children, who are more sensitive to radiation. Developing effective interaction skills can therefore contribute to safer examinations. Thus, to implement preparation effectively, it is necessary to adjust the environment and intervention strategies according to the characteristics of each imaging

modality.

3-2 Knowledge of and Interest in Preparation

Awareness of preparation among technologists in our department was low (below 40%). However, after being presented with a definition of preparation, all respondents recognized its necessity and its potential usefulness in improving the pediatric examination environment. Furthermore, approximately 90% expressed interest in attending training sessions, indicating a high level of motivation to learn. These findings suggest that many technologists believe that acquiring basic knowledge and skills related to pediatric care would improve the clinical environment. Because children cannot be managed using a uniform approach, there is strong support for creating an environment that facilitates cooperation through communication appropriate to each child's level of understanding. Radiological examinations are generally painless, and previous reports indicate that most children can complete them successfully when both preparation and the examination environment are properly managed [8].

Overall, these findings suggest that implementing preparation and optimizing the examination environment in our radiology department may enable us to provide higher-quality care for children and their families.

4. Conclusion

This survey revealed limited confidence and skills in pediatric care among radiological technologists at our hospital. It also indicated that examinations and treatments are currently conducted primarily healthcare-provider-centered manner. At the same time, respondents demonstrated strong awareness of the need for preparation and expressed high motivation to improve the clinical environment. These findings suggest that introducing structured preparation is essential to provide higher-quality radiological examinations and treatments for children and their families.

Future challenges include organizing staff training through collaboration with CLS, establishing systems and environments that enable preparation practices in each imaging modality, and evaluating the impact of these interventions on the awareness and practices of radiological technologists. Through these organizational efforts, it should be possible to create an environment in which children can undergo examinations and treatments with greater reassurance and participate more actively in their healthcare experience.

Conflict of Interest

The authors declare that they have no conflicts of interest related to this manuscript.

Acknowledgments

The authors thank the radiological technologists in the Department of Radiology at Toyama University Hospital for their cooperation in this study. Additionally, a portion of this research was presented at the 15th Chubu Radiological Technology Academic Congress (Fukui, 2023).

References

1) Hanada A, et al.: Reducing anxiety in pediatric imaging—from the perspective of a CLS. Pediatr Med, 53(9), 1351-5, 2021. (in Japanese)
2) Narakino H: Preparation for CT and MRI examinations. EB NURSING, 9(1), 8-14, 2009. (in Japanese)
3) Warita Y, et al.: Supporting children by believing in their strengths—Multidisciplinary pediatric imaging preparation. J Child Health, 78(6), 565-70, 2019. (in Japanese)
4) Harada K, et al.: How to interact and support children in pediatric care from their perspective. Gakken, 58-61, 2023. (in Japanese)
5) Wakimoto S: Support for infants undergoing examinations/procedures requiring rest—Interactions without sleep induction. Jpn J Nurs Soc: Pediatr Nurs, 34, 17-9, 2003. (in Japanese)
6) Hashizume K, et al.: Development of an animation projection system for pediatric head CT. Jpn J Radiol Technol, 74(12), 1428-33, 2018. (in Japanese)
7) Ishikawa Y: Preparation for pediatric patients undergoing radiotherapy. The Japanese Journal of Oncology Nursing, 4(3), 324-8, 2014. (in Japanese)
8) Harada K, et al.: Effective ways to interact with children receiving medical care, 2nd ed. Japanese Nursing Association Publishing, 28-197, 2020. (in Japanese)
9) Japan Pediatric Society, et al.: Joint recommendations regarding sedation during MRI examinations. J Jpn Pediatr Soc, 124(4), 771-805, 2020. (in Japanese)
10) Hirata M: Challenging drug-free MRI for children—From a child-centered perspective. J Pediatr Pract, 12, 107-12, 2020. (in Japanese)
11) Naama Barnea-Goraly, et al.: High success rates of sedation-free brain MRI scanning in young children using simple subject preparation protocols with and without a commercial mock scanner–the Diabetes Research in Children Network (DirecNet) experience. Pediatr Radiol, 44, 181-6, 2014.
12) Jaimes C, et al.: Strategies to minimize sedation in pediatric body magnetic resonance imaging. Pediatr Radiol, 46, 916-27, 2016.
13) Khan JJ, et al.: A program to decrease the need for pediatric sedation for CT and MRI. Appl Radiol, 36, 30-3, 2007.
14) Kato M, et al.: Perceptions of radiological technologists regarding preparation. Jpn J Nurs Soc: Pediatr Nurs, 166-169, 2014. (in Japanese)
15) Takemoto K, et al.: Investigation of the Care-Givers' Situation for Children Having Treatment or Examination. Mem Fac Med Shimane Univ, 34, 35-42, 2011. (in Japanese)
16) Ohnishi H, et al.: Cancer/Radiotherapy 2017, 7th ed. Shujunsha, 1125-1166, 2017. (in Japanese)

Received April 27, 2025; accepted June 25, 2025

The effect of workflow chart granularity on patient safety

KAWASAKI Yoshiyuki[1)]*, YOSHIDA Tatsuya[2)]

1) Department of Radiology, Okinawa Central Hospital
2) Department of central Radiology, Tatebayashi Kosei General Hospital

* E-mail: zenkou0226@gmail.com

Note: This paper is secondary publication, the first paper was published in the JART, vol. 72 no. 879: 31-38, 2025.

Key words: Patient safety, Workflow chart, Radiology operations, Root cause analysis (RCA)

【Summary】
Purpose: Workflow charts were established at our facility, but their granularity was coarse, leading to frequent incidents despite countermeasures. Therefore, we developed a more detailed workflow chart, in which each step was defined by a subject-verb-object format centered on individual actions. This study examined the impact of workflow chart granularity on patient safety.
Methods: We investigated the number of incidents, the recurrence rate of cases analyzed using root cause analysis (RCA), and the time required for RCA before and after the implementation of highly granular workflow charts.
Results: The detailed workflow charts contributed to a lower incident recurrence rate, a shorter RCA time, and increased awareness of patient safety.
Conclusion: A high-resolution workflow chart is essential for ensuring patient safety.

Introduction

According to the World Health Organization (WHO) technical report and guidance titled, "Patient Safety Incident Reporting and Learning Systems" (2020), an incident is defined as "any deviation from usual medical care that causes injury to the patient or poses a risk of harm. This includes errors, preventable adverse events, and hazards" [1)]. Furthermore, Heinrich stated that for every major accident, there are 29 minor accidents and 300 incidents [2)]; thus, reducing the number of incidents can lead to a reduction in major accidents. Representative methods for reducing incidents include root cause analysis (RCA), fault tree analysis, and failure mode and effects analysis. WHO describes RCA as a systematic method for analyzing all factors that could potentially cause or prevent errors and highlighted its efficacy in formulating recurrence prevention measures [3)]. The Royal College of Radiologists also recommends disseminating countermeasures obtained through RCA to prevent the recurrence of incidents [4)].

Regarding the practical application of RCA, Yanagawa and Yoshida recommended formulating countermeasures by making comprehensive judgments based on the creation of a timeline of events, an analysis of causes, and a causal diagram [5, 6)]. Additionally, the "Guidelines for the Medical Accident Investigation System" by the All Japan Hospital Association recommends visualizing operations using a workflow chart and formulating recurrence prevention measures through RCA based on these charts [7)]. Briefly, it is crucial to conduct RCA based on a workflow chart. However, in many cases, optimal prevention measures are not formulated because workflow charts are not appropriately created [8)], making the development of proper workflow charts indispensable.

Workflow charts have been established in the Radiology Department of our facility to standardize and visualize radiological technology operations. However, the granularity was coarse, consisting only of descriptions such as "register the patient," "perform imaging," "veri-

fy images," and "guide the patient," which made it difficult to review intermediate work processes. Consequently, during RCA, perceptions of work processes differed among staff members, and creating the timeline of events for RCA required an extensive amount of time. Despite implementing countermeasures derived from the analysis of causes, recurrence remained prominent, such as patient information entry errors in general radiography. Therefore, we developed high-resolution workflow charts to standardize and visualize operations and examined the resulting effects. This study aimed to investigate and clarify the impact of establishing high-resolution workflow charts on patient safety.

1. Methods

1-1. Creation of Workflow Charts

We developed high-resolution workflow charts based on "Basic Knowledge and Application Examples of Creating Operational Workflow Charts" published by the Japanese Standards Association [8]. For these high-granularity workflow charts, each step was defined as a single action in the first-person singular to ensure that the sequence of actions for the staff involved in the work processes was clear. Five members of the Radiological Technology Department created these charts between April and June 2019, and the period through March 2020 comprised a transition phase. Microsoft Word (Microsoft, Redmond, WA, USA) was utilized for the creation of the workflow charts.

Our facility is equipped with general radiography systems, computed tomography, magnetic resonance imaging, X-ray fluoroscopy systems, mobile X-ray units, Gamma Knife, and a picture archiving and communication system (PACS). We created workflow charts for all operations involving this equipment.

1-2. Trends in Incidents and Accidents

In establishing the workflow charts, we investigated the numbers of incidents and accidents, their occurrence rates, and the characteristics of their content. The study period was divided into two phases: the "pre-implementation" period from April 2017 to March 2019, during which the conventional workflow charts were used; and the "post-implementation" period spanning April 2020 to March 2023, during which the high-granularity workflow charts were utilized. The transition period from April 2019 to March 2020 was excluded from the analysis.

In aggregating the data for this study, "incidents" were defined as cases that did not affect the patient (near-misses), and "accidents" were defined as cases in which the event affected the patient.

1-3. RCA Implementation

For frequently occurring accidents, we conducted RCA based on "Basic Knowledge and Application Examples of RCA" published by the Japanese Standards Association [9]. Regarding the RCA process, for each occurring case, a timeline of events was created according to the established workflow chart. In this process, care was taken to clearly identify deviations by using different colors for the deviant steps. Next, an analysis of causes was conducted to assess these deviations. During this analysis, we endeavored to identify the true root factors by repeating the "why-why" analysis at least three times. Finally, a causal diagram was created by tracing back from the analysis of causes to ensure there were no inconsistencies in the analysis, after which the details and timing of countermeasures were determined.

RCA was performed by five members of the Radiological Technology Department, with final validation conducted in collaboration with the facility's medical safety department. Following RCA implementation, the workflow charts were revised, and meetings were held within the department to share information and ensure consensus.

1-4. Investigation of the Recurrence Rate and RCA Time

For cases in which RCA was implemented, we investigated the recurrence rate and the time required for analysis. The recurrence rate was calculated by dividing the number of occurrences before and after establishment of the workflow charts by the total number of corresponding examinations. We additionally compared the time required for analysis between the periods before and after workflow chart creation.

Statistical significance was denoted by $p < 0.05$. The chi-squared test was used to analyze the recurrence rate, and the Mann-Whitney U test was used to compare the analysis time. All statistical analyses were performed using EZR (Easy R version 1.68; https://www.jichi.ac.jp/saitama-sct/SaitamaHP.files/statmed.html) [10].

1-5. Awareness Survey

An awareness survey regarding medical safety was conducted among the five members of the Radiological Technology Department before and after workflow chart creation. The survey evaluated three key areas: "knowledge regarding medical safety," "importance of operational workflow charts and manuals," and "communication and information sharing among staff members." Each item was rated on a 5-point scale from 1 (lowest/weakest) to 5 (highest/strongest). The questionnaire is presented in Fig. 1.

Medical Safety Awareness Survey

At Okinawa Central Hospital, we are actively engaged in medical safety initiatives, including the development of operational workflow charts, the aggregation of incident/accident reports, and the performance of root cause analysis.

We are conducting this survey to periodically assess and monitor changes in staff awareness. Your cooperation in completing this questionnaire is greatly appreciated.

Instructions

Rate each item on a 5-point scale, where **5 is the highest (strongest/most), 3 is the standard, and 1 is the lowest (weakest/least)**.

1. Do you feel you have sufficient knowledge regarding medical safety?

5: Highly sufficient
4: More than average
3: Average
2: Some knowledge
1: Minimal to none

2. How important do you think operational workflow charts and manuals are?

5: Critically important
4: Necessary
3: Beneficial to have
2: Not very necessary
1: Not necessary at all

3. How important do you think communication and information sharing among staff members are?

5: Critically important
4: Necessary
3: Beneficial to have
2: Not very necessary
1: Not necessary at all

Thank you for your cooperation.

Medical Safety Management Office Okinawa Central Hospital

Fig. 1 Contents of the questionnaire survey

1-6. Ethical Considerations

This study did not require approval by the institutional ethics committee of our facility.

2. Results

2-1. Creation of Workflow Charts

High-granularity workflow charts were created for all modalities. As an example, the workflow charts for general radiography, the modality with the highest volume of cases, are presented in Figs. 2 (conventional) and 3 (newly established). The conventional chart

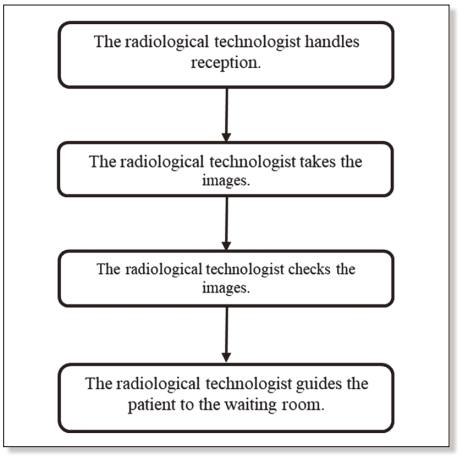

Fig. 2 Conventional workflow chart

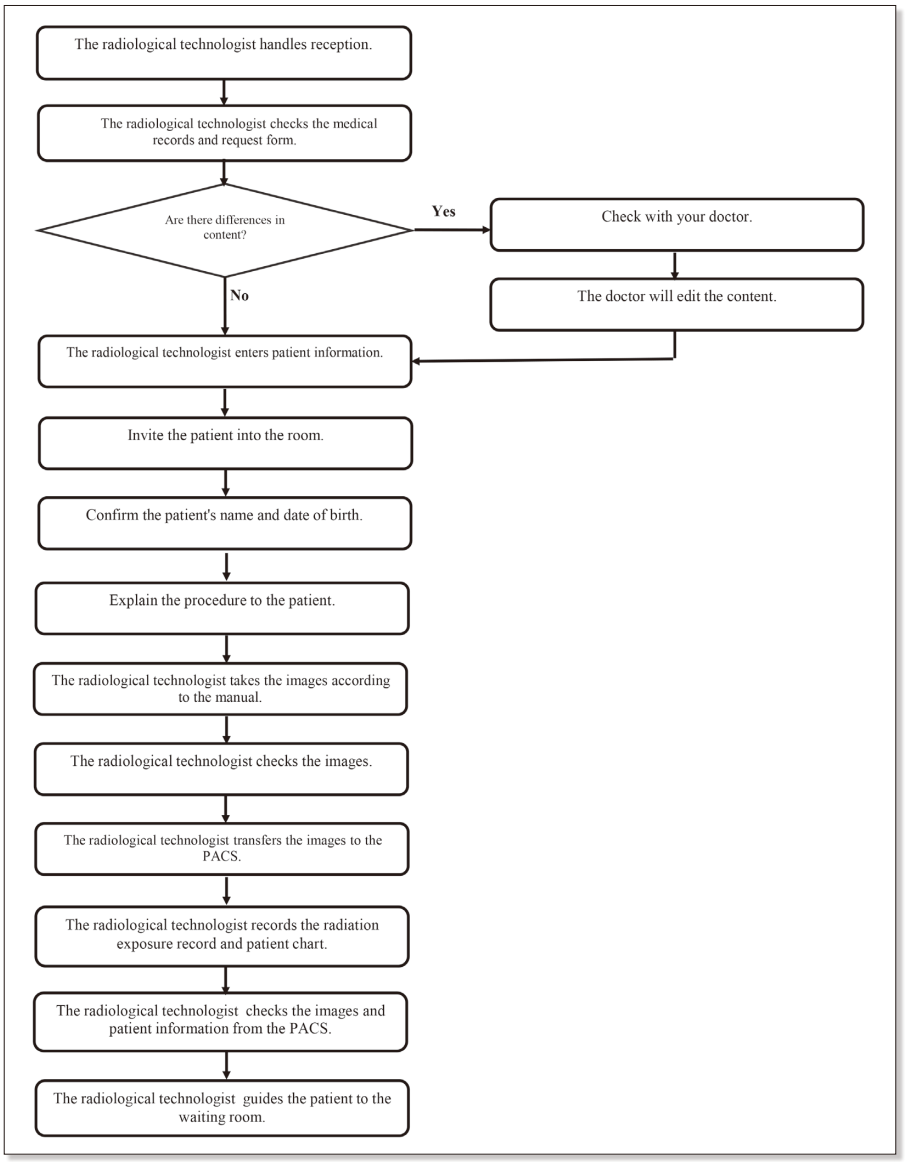

Fig. 3 Granular workflow chart

had coarse work processes, making it difficult to review the steps. Contrarily, the newly established workflow chart was created with each step defined as a single action in the first-person singular, thereby clarifying the work processes and making operational content and flow easier to understand.

2-2. Trends in Incidents and Accidents

The trends in the number of incidents and accidents are presented in Table 1, whereas the breakdowns of incidents and accidents are presented in Figs. 4 and 5, respectively. Although there were no incident reports at before the new workflow charts were established, the number of reports increased after implementation, and the occurrence rates of both incidents and accidents declined. In total, "imaging parameter setting errors," "patient information entry errors in general radiography," and "wrong side/site errors" accounted for 80.5% of all incidents and 76.3% of all accidents.

Table 1 Trends in the number of incidents and accidents and occurrence rate

	2017	2018	2020	2021	2022
Incident number	0	0	77	43	37
Accident number	43	38	33	18	13
Occurrence rate (%)	0.52	0.45	1.37	0.74	0.60

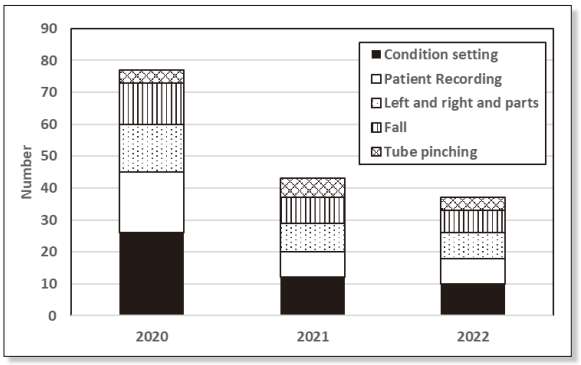

Fig. 4　Breakdown of incidents

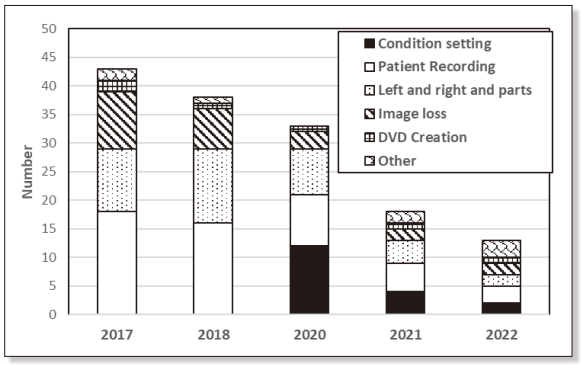

Fig. 5　Breakdown of accidents

2-3. RCA Implementation

RCA was conducted for frequently occurring accidents. RCA was specifically conducted for 24 cases, including 11 cases before and 13 cases after high-resolution workflow chart establishment.

A representative case involved a patient information entry error in general radiography, in which incorrect patient information was entered into the imaging device. The error was identified only after a physician noted that the captured images were missing from the PACS. The timeline of events is presented in Fig. 6, the analysis of causes is presented in Fig. 7, and the causal diagram and countermeasures is presented in Fig. 8. The timeline of events documented each step of the workflow chart (Fig. 3), with measures taken to clearly identify deviant items. Deviations occurred at steps 3, 8, and 9 of the timeline of events, indicating a failure to verify patient information during entry, image verification, and image transfer.

Based on the analysis of causes conducted for steps 3, 8, and 9, the root factors were a failure to describe the steps in the workflow chart, failure to verify patient information, and

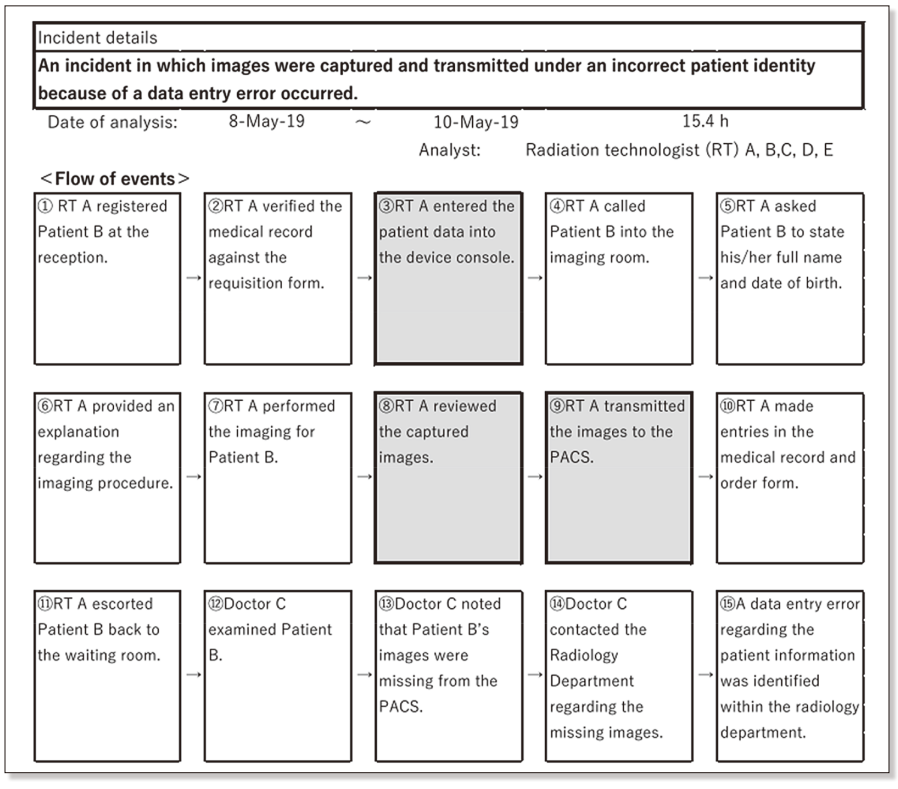

Fig. 6　Timeline of events involving a patient information entry error in general radiography

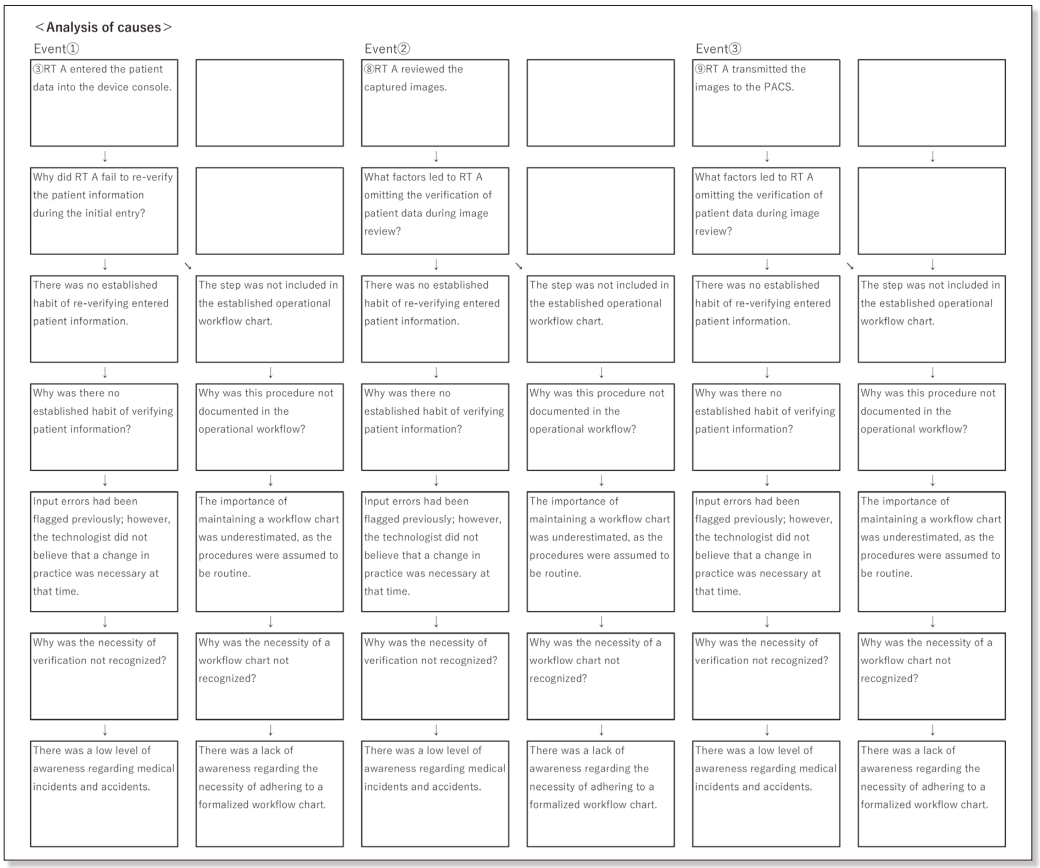

Fig. 7　Analysis of the causes of patient information entry errors in general radiography

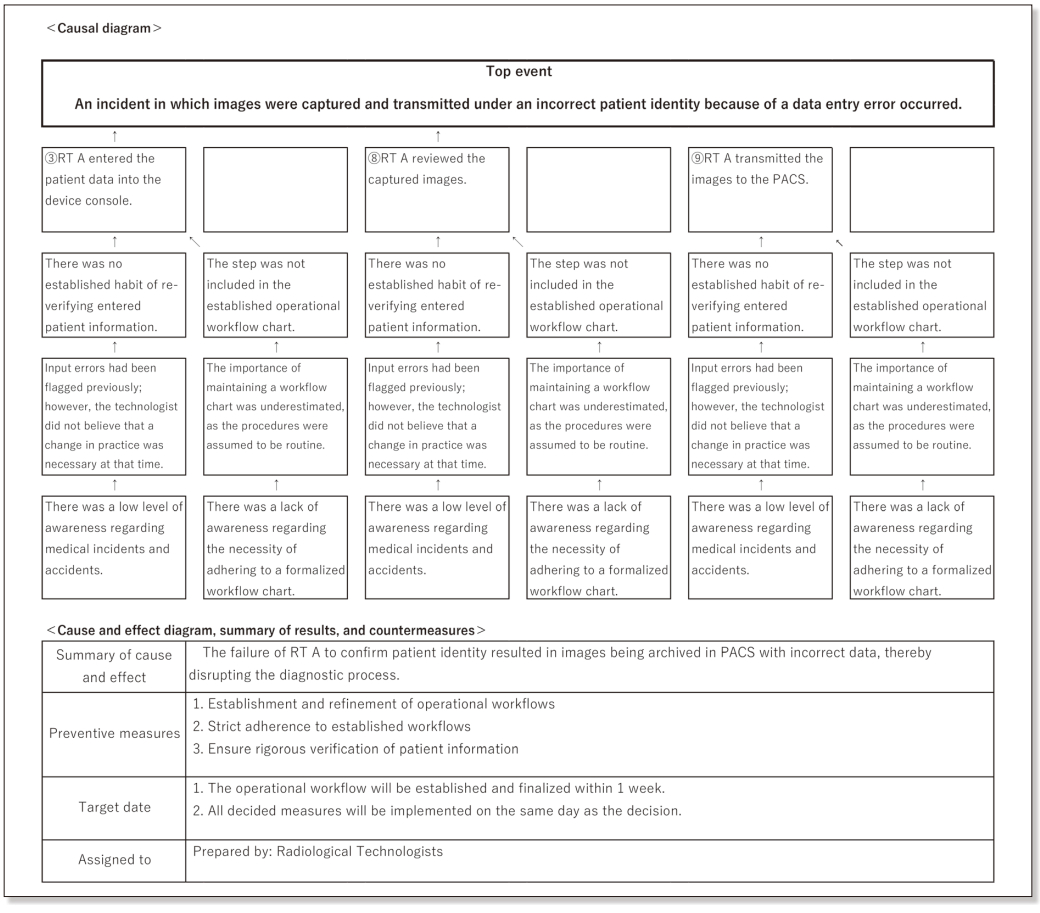

Fig. 8　Causal diagram for patient information entry errors in general radiography

low awareness regarding medical accidents. Subsequently, a causal diagram was created by tracing back these factors to consider countermeasures. The establishment of granular workflow charts (standardization), the necessity of medical safety education, and strict adherence to the workflow charts were deemed essential. The revised workflow chart based on these results is presented in Fig. 9, with enlarged views of the revisions presented in Fig. 10 (a) and (b). Specifically, steps were added for the operator to verify information during patient registration and for another staff member to verify both patient information and images upon transfer to the PACS.

The RCA results revealed that the main causes of deviations were non-adherence to the workflow chart and the immaturity of the workflow chart itself. The rates of these factors changed significantly after the

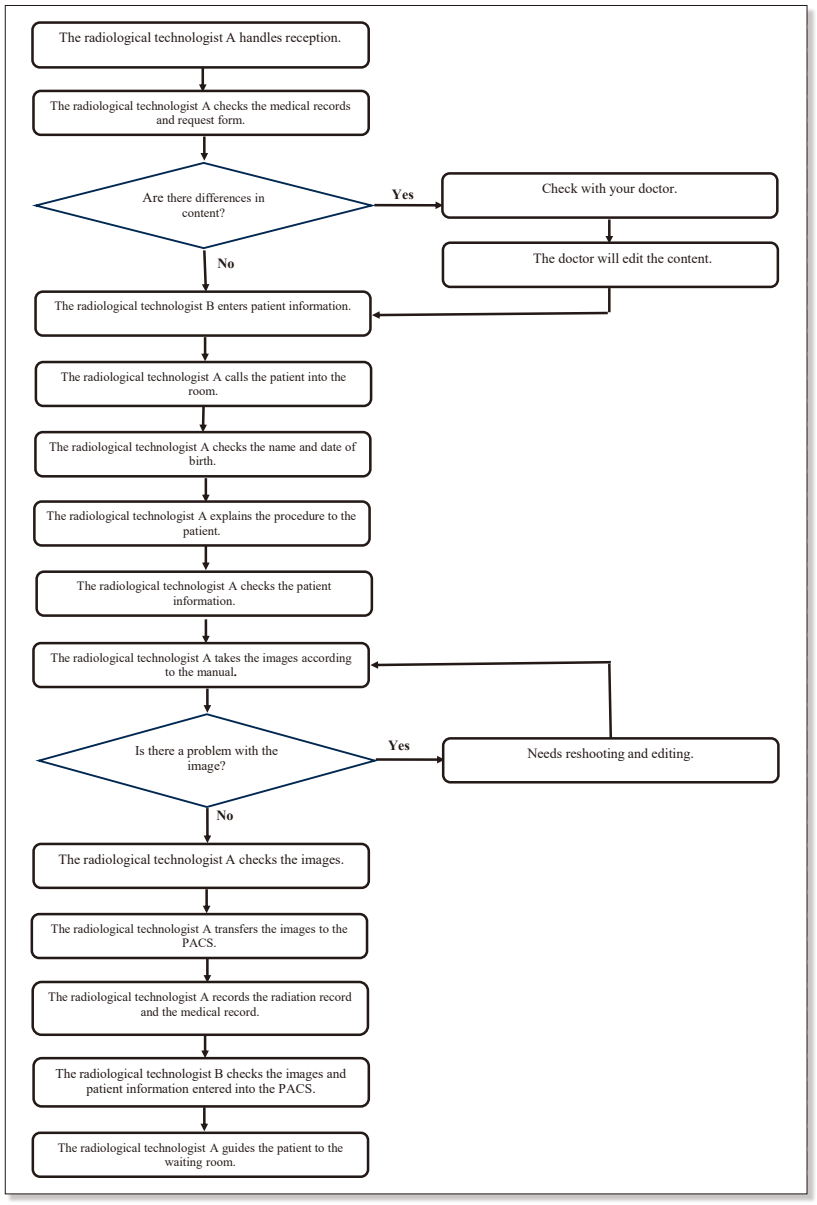

Fig. 9 Revised workflow chart

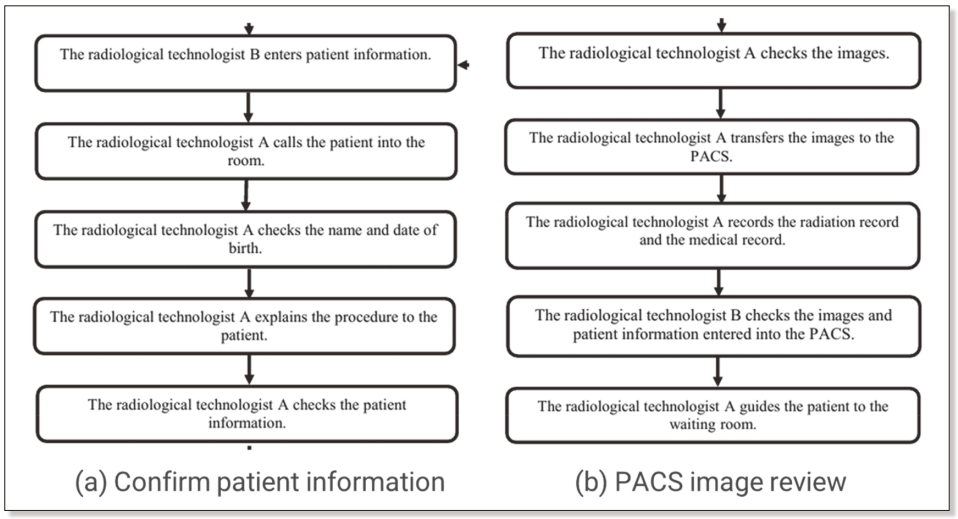

Fig. 10 Excerpt from the revised workflow chart
(a) Confirm patient information (b) PACS image review

high-resolution workflow charts were established. Specifically, the rate of "immaturity of the workflow chart" decreased from 81.8% before implementation to 17.6% after implementation.

2-4. Investigation of the Recurrence Rate and RCA Analysis

Comparing the periods before and after implementation, the recurrence rates decreased significantly after implementation ($p < 0.05$). Specifically, the rate of patient information entry errors decreased from 0.21% to 0.07% the rate of wrong side/site errors declined from 0.15% to 0.06%, and DVD registration errors for patients referred from other hospitals fell from 0.99% to 0.67% after implementation.

Next, we investigated the time required for RCA before and after the implementation. The analysis time was significantly shortened ($p < 0.05$) from 22.4 ± 8.0 h before implementation to 4.5 ± 2.0 h after implementation.

2-5. Awareness Survey

The awareness survey regarding "knowledge regarding medical safety," "importance of operational workflow charts and manuals," and "communication and information sharing" was conducted using a 5-point scale. The scores for "knowledge regarding medical safety," "importance of operational workflow charts and manuals," and "communication and information sharing" improved from 2.0, 3.0, and 2.6, respectively, before implementation to 3.8, 4.2, and 4.0, respectively after implementation. These results indicate increases in knowledge and awareness of medical safety and greater recognition of the necessity of workflow charts and manuals, as well as the importance of information sharing and communication skills.

3. Discussion

In this study, we evaluated the effects of establishing highly granular workflow charts on patient safety. Comparing the findings before and after implementation, the number of incident reports increased after the charts were established, whereas none was reported before establishment. This lack of reporting prior to implementation is likely attributable to the coarse nature of the previous workflow charts, which prompted individuals to perform tasks based on their own judgment for steps without explicit documentation, making it difficult to distinguish whether a task deviated from the standard. Furthermore, a lack of awareness regarding medical safety might have contributed to the absence of reports. Conversely, after implementation, the definition of each step as a single action in the first-person singular by the entire Radiological Technology Department facilitated the visualization and standardization of work processes. We believe that this clarification of work steps made it easier for both the staff in charge and support staff to identify and highlighting deviations.

Furthermore, the recurrence rate of cases analyzed through RCA was high before workflow chart implementation. We consider this attributable to the fact that the coarse workflow charts lacked detailed content between work steps, leading to significant variations in tasks and procedures among staff. Consequently, the RCA results did not effectively benefit all staff members. After implementation, we believe that the recurrence rate decreased significantly because of the refinement of operations through revised workflow charts and increased awareness of adherence to these charts. This improvement is attributable to the transition from workflow charts managed by a single individual to a system in which multiple staff members were involved, allowing them to support each other.

The time required for RCA was also shortened after workflow chart implementation. This can be attributed to the accumulation of experience in RCA, as well as the maturation of the workflow charts through repeated revi-

sions, which facilitated the RCA process. These findings are supported by the results of the awareness survey, which confirmed improvements in medical safety awareness, the perceived necessity of workflow charts and manuals, and information sharing and communication skills. We believe these effects were achieved through the PDCA cycle, involving systematic participation by all department staff, high-granularity workflow chart establishment, aggregation and reporting of incidents/accidents, and the implementation of RCA followed by workflow chart revisions.

In this study, the establishment of granular workflow charts provided several positive effects, including improved awareness of medical safety, visualization and standardization of operations, a reduction in the accident recurrence rate, and a decrease in the RCA time. Although it is difficult to conclude that all of these effects resulted solely from the establishment of new workflow charts, workflow charts were confirmed to play a critically important role in building a medical safety management system.

4. Conclusion

The establishment of highly granular workflow charts, in which each step is defined as a single action in the first-person singular, improved medical safety awareness and communication skills. For instances of deviation, the implementation of RCA and subsequent revision of the workflow charts led to a lower recurrence rate and shorter RCA time.

Highly granular workflow charts are expected to improve medical quality, safety, and operational efficiency. Moving forward, we intend to continue these activities and further mature the workflow charts to ensure their effectiveness in emergency situations.

Conflict of Interest (COI)

The first author and all co-authors have no conflicts of interest to disclose.

Previous Presentation

A portion of this study was presented at the 19th Congress of the Japanese Society for Quality and Safety in Healthcare (Yokohama, Kanagawa, Japan).

References

1) World Health Organization: Patient Safety Incident Reporting and Learning Systems: Technical report and guidance, 2020. Available from: https://www.who.int/publications/i/item/9789240010338 [Accessed 10th September 2024]
2) Heinrich HW: Industrial Accident Prevention; A Scientific Approach. 1-488, McGraw-hill Book Company, 1941.
3) World Health Organization: Patient Safety Workshop: Learning from Error. 1-28, WHO, 2010.
4) The Royal College of Radiologists, et al: Towards Safer Radiotherapy. 1-84, British institute of Radiology, 2008.
5) Yanagawa T: Practice Method of RCA and FMEA. Journal of Japan Society for Safety Engineering. 56(5), 330-334, 2017 (in Japanese).
6) Yoshida T, et al.: Implementation and Effectiveness of Measures to Prevent Recurrence of Incidents Developed through Root Cause Analysis Using Work Flowchart. Jpn J Radiol Technol. 80(3), 304-310, 2024 (in Japanese).
7) All Japan Hospital Association: Guidelines for the Medical Accident Investigation System. All Japan Hospital Association; 2015 (in Japanese).
8) Iida S, et al.: Basic Knowledge and Application Examples of Creating Operational Workflow Charts. Japanese Standards Association, 2nd Edition; 2021 (in Japanese).
9) Iida S, et al.: Basic Knowledge and Application Examples of RCA. Japanese Standards Association, 2nd Edition; 2006 (in Japanese).
10) Y Kanda: Investigation of the freely available easy-to-use software 'EZR' for medical statistics. Bone Marrow Transplantation, 48, 452-458, 2013.

Regulations and Requirements for Submissions to the Journal of the Japan Association of Radiological Technologists

Submission Regulations

Revised: April 1, 2013
October 30, 2013
February 20, 2016
April 20, 2019
October 3, 2020
July 9, 2022
December 3, 2022

Objective

Article 1. These regulations are based on the operations defined in Article 4 of the articles on the incorporation of the Japan Association of Radiological Technologists (hereafter "the Association"). They stipulate the criteria for submissions to the Journal and informational magazines published by the Association (hereafter "the Journal, etc.").

Eligibility

Article 2.

2-1. Only members of this association are allowed to submit articles to the association's journal, etc.

2-2. However, the following requirements must be met in order to submit articles:

(1) Students of radiologic technology schools who have a member of this association as a co-author.

(2) Individuals with a foreign nationality who hold a radiologic technologist license.

(3) Non-members other than the above may submit articles by paying half of the association membership fee per article as a submission fee.

2-3. The submission fee stated in the preceding paragraph 3 will not be refunded regardless of whether the article is accepted or not.

2-4. Co-authors do not need to pay the submission fee.

Copyright

Article 3. The copyright of the published manuscript is based on rules regarding the management of the works of the Society.

Obligations

Article 4.

4-1. The topic of submitted manuscripts must belong to a relevant domain to technologies for prevention, diagnosis, and treatment related to radiation therapy, and manuscripts must be unpublished.

4-2. Submitted papers, whether for fundamental or applied research, must sufficiently consider bioethics, and authors must bear the ultimate responsibility for their content.

4-3. Fabrication, forgery, plagiarism, violation of the law, and other forms of wrongdoing are not allowed in submissions.

4-4. If the author has already reported similar content to that of the published manuscript or submitted it to another journal, the author is required to explain the difference from the manuscript in a separate document.

4-5. The author must disclose all information regarding conflicts of interest.

4-6. The author shall be held accountable for any misconduct regarding the content of the publication, and the Society shall not be involved at all.

Submissions

Article 5. The types of accepted submissions are categorized as follows:

(1) Original articles
Highly original research papers with clear objectives and conclusions.

(2) Review articles
Articles systematically summarizing a specific research domain from a particular perspective.

(3) Rapid communications
Reports of original research that must be published rapidly.

(4) Reports
Surveys of significance to the study of radiological technology or reports of interesting and

important cases.

(5) Notes

Articles on the development or evaluation of new equipment, techniques, products, etc.

(6) Technical material

Compilations of survey data or technical aspects, or anything that can serve as a reference for research and technology.

(7) Overview articles

A compilation of technologies, principles, or basic elements with reference to the literature. However, what was explained in the development and use of equipment and software constitutes a technical explanation.

(8) Miscellaneous

Other items approved by the editorial committee for publication, such as lecture transcripts, courses published as journal articles, and newspaper/magazine articles that were not published in Issues 1–7.

How to submit

Article 6.

6-1. Use the online posting system.

6-2. The author shall save the duplicate data of the submitted manuscript until the publication decision.

Formatting

Article 7. The explanation of the manuscript shall be provided according to the submission procedure specified separately.

Reception of submissions

Article 8. The reception date shall be the date on which the editorial board has determined to comply with this regulation.

Review

Article 9.

9-1. Received manuscripts will be reviewed carefully and impartially by peer-reviewers selected by the editorial committee.

9-2. Peer reviews are limited to two times. However, in the case of Article 5, items 7 and 8, in principle, peer review is not performed.

9-3. The acceptance or rejection of the manuscript will be decided by the editorial committee in consideration of the opinions of the reviewers, and the date will be the final acceptance date.

Corrections

Article 10.

10-1. In principle, the author must proofread the manuscript up to twice and return it by the designated date. If the deadline is breached, the school will be completed with the proofreading of the editorial board.

10-2. The correction of words and plates that were not included in the manuscript is not allowed.

Printing

Article 11.

11-1. 20 copies of the papers published in the Journal, etc., will be presented to their authors as an offprint.

11-2. The authors must bear the expenses of any additional offprints. If additional offprints are required, they must be requested by the time corrections are submitted.

Revision or repeal of regulations

Article 12.

12-1. This regulation will come into effect on April 1, 2012.

12-2. This regulation will come into effect on April 1, 2016.

12-3. This regulation will come into effect on April 20, 2019.

12-4. This regulation will come into effect on October 3, 2020.

12-5. This regulation will come into effect on July 9, 2022.

12-6. This regulation will come into effect on December 3, 2022.

Requirements for Submissions to the Journal of the Japan Association of Radiological Technologists

Revised: February 20, 2016
April 20, 2019
October 3, 2020
July 19, 2023

Based on Article 7 of the Submission Regulations of the Japan Association of Radiological Technologists, the following guidelines must be followed for manuscript submission:

1. How to write original articles, reviews, breaking news, reports, notes, materials, and explanations

1) Title and abstract

Enter the following items in the online posting system.

①List the author's name, institution, affiliation and occupation, and contact information, and select the field of expertise. The author's qualifications should be as specified in the submission guidelines.

②Select the type of post.

③Provide the title in both Japanese and English, and include information about the co-authors. List the co-authors in the order of authorship. If a co-author is not a radiological technologist, their qualifications should be as specified in the submission guidelines.

④Summarize the abstract in Japanese and English within 300 characters (words).

⑤Enter the keywords in English. Keywords should be in noun forms and should be limited to five.

2) Text and figures/tables

Create the main text, including figures and tables, in a single file. Additionally, prepare figures and tables as separate files and submit them.

①The manuscript should be in Japanese or English.

Create the document using Word with A4 paper size. Use Mincho font for Japanese text and Times font for English text, both at 12 points. Set the line spacing to 18 points. Leave a margin of at least 2 cm on all sides (top, bottom, left, and right).

②The specified number of pages and excess page costs of the manuscript are as shown in the following table.

Type of submission	Number of pages (as published)	Fee for additional pages
Original articles	8	¥10,000 per page
Review articles	8	
Rapid communications	3	
Reports	3	
Notes	8	
Technical material	8	
Overview articles	8	
Technical overview articles	4–6	None
Miscellaneous	2 (strictly enforced)	

③As a general rule, academic terms should conform to Cabinet Notification No. 2 and JIS.

④The unit of quantity is the International System of Units (SI).

⑤Include page numbers and line numbers in the main text.

⑥Use ", " and ". " for punctuation.

⑦Use full-width characters for Katakana and half-width characters for English letters and numbers.

⑧The main text should be structured with headings such as Introduction, Methods, Results, Discussion, Conclusion, and References.

⑨For equipment, include the generic name, model, manufacturer, city, and country.

⑩Number the equations.

⑪The figures and tables created as separate files from the main text are of higher resolution and can be subjected to secondary processing in production.

⑫Number the figures and tables.

⑬Ensure that all figure and table numbers are referenced in the main text.

⑭For academic papers, write the titles of figures and tables, as well as the text within the tables, in English.

⑮Provide Japanese explanations for figures and tables.

⑯When reproducing figures and tables, clearly indicate the source and ensure that the author has obtained permission from the original source.

3) References

References should be listed in the order in which they appear, with the numbers in parentheses at the end of the referenced text.

The notation format is as follows.

①For magazines

Author names: Title (article title) Magazine name (abbreviation), volume, first-last page, year of publication.

②For a book

Author names: Book title, First-last page, publisher, year of publication.

③If there are two or more authors, enter only the first author and enter “other” and “et al.”

4) Trademark name

If a trademark name is required, write the trademark name in both parentheses after the common name and add ®.

5) Acknowledgments

Create a separate file from the main text for the acknowledgments.

2. Submission of copyright transfer agreement

(1) The first author and co-authors must agree to the contents of the copyright transfer agreement as specified in the copyright regulations.
(2) The copyright transfer agreement should be as specified in the copyright regulations, and the designated form available on the society's website must be used.
(3) The copyright transfer agreement must be signed by the first author and co-authors, and provided when the manuscript is submitted.

3. About secondary publication

(1) Obtain approval from the editorial departments of both the first and second journals.
(2) The period until the secondary publication should be decided through discussions between the editorial departments of both parties and the author.
(3) Secondary publications of treatises are intended for different types of readerships.
(4) The secondary publication of a treatise should faithfully reflect the content of the first treatise.
(5) Specify the source of the original treatise.
(6) Specify in the title that it is a secondary publication.

4. About technical commentary requested by the editorial board

The structure of the document should generally follow the sections (1) to (9) below.

(1) Abstract (100-150 words in Japanese and English)
(2) Keywords (3 words)
(3) Introduction:
(4) Purpose of explanation (overview)
(5) Main paper
(6) Comparison and consideration with previous research (development technology)
(7) Clinical usefulness
(8) Conclusion
(9) References

Journal of JART
-English edition 2026-

June 15, 2026

Issuer: Ueda Katsuhiko
Publisher: The Japan Association of Radiological Technologists
22F Mita Kokusai Building. 1-4-28,
Mita, Minato-ku, Tokyo. 108-0073
TEL: +81-3-4226-2211　FAX: +81-50-3153-1519
https://www.jart.jp

・Published by The Japan Association of Radiological Technologists

The Japan Association of Radiological Technologists
https://www.jart.jp